Proceedings of the Master's Programme Cognitive Neuroscience of the Radboud University

Contact Information:
Journal CNS
Radboud University
Postbus 9104
6500 HE Nijmegen
The Netherlands
nijmegencns@gmail.com

Table of Contents

From the Editor-in-Chief

Dear reader,

I am pleased to present you the first issue of *Proceedings of the Master's Programme Cognitive Neuroscience* for the academic year 2015-2016. Last year was the 10th anniversary of the journal and the publication of the issue 10.1 was accompanied by a very nice launch event. This year, I am happy to continue with the journal tradition for the second decade of the journal's existence.

For this issue, we have selected high quality articles covering a whole range of fields and research techniques in neuroscience. On one hand, we have articles from the field of cognitive neuroscience reporting experiments using neuroimaging techniques electroencephalography (EEG), magnetoencephalography (MEG) and functional magnetic resonance imaging (fMRI) to study such complex human behaviours as expectation, attention and language. On the other hand, this issue also contains articles on molecular and cellular neuroscience studies that used such various techniques as immunocytochemistry, co-immunoprecipitation, and fluorescence imaging. These studies used both human genetic data as well as model organisms, such as yeast, to study protein-protein interactions and signalling pathways related to mutations causing deafness and language impairment. All in all, I hope you enjoy reading these excellent and diverse articles by students graduated from the Research Master's programme Cognitive Neuroscience.

I would like to thank the whole journal team for their work, which is completely voluntary and done as an extracurricular activity next to studies and other responsibilities. Also, the reviewers deserve a big thank you for their valuable contribution in evaluating the quality of the articles. Without the reviews, the journal team could not have made an informed and objective decision on which articles to publish. We are also lucky to be able to publish two coloured issues of 100 pages each academic year with the sponsoring from our Master's programme. Lastly, I would like to thank the authors for their quality work and for revising their articles according to feedback received from the reviewers. We are happy to publish your work in the journal.

With a final thank you to everyone who contributed to the publication of this issue, I wish you a pleasant read!

Nijmegen, March 2016

Karita Ojala

Editor-in-Chief

From the Head of the research line Molecular Neurogenetics

Dear reader,

What makes the Donders Institute for Brain, Cognition and Behaviour a world-class institute is the ambition to exert research excellence over a wide range of timely topics in neuroscience. This is achieved by the dedication of top scientists who work together in an interdisciplinary research line, characterized by genetic, molecular and cellular processes at one end and computational, systems-level neuroscience with cognitive and behavioural analyses at the other end. Such an interdisciplinary strategy creates a significant increase of the scientific, societal and medical impact of research within the Donders.

In my own research line, I have personally experienced that it is highly rewarding and stimulating to build bridges between the Departments of Human Genetics and Cognitive Neuroscience, and to merge research fields that were previously not connected. Performing fundamental research on the molecular and cellular functions of a specific gene or protein is great, but it is even greater if this gene is underlying a neurodevelopmental disorder such as intellectual disability or autism. In that case, logical connections can be made to clinical applications of the fundamental studies and to deciphering the role of the gene in establishing and maintaining neural networks engaged in cognitive tasks affected by mutations in that gene. However, making connections to other fields takes a considerable effort. You have to be able to think out of the box. For that, you have to be prepared to step out of the comfort zone of your primary field of research and invest in becoming acquainted with the methodologies and opportunities that are offered by other disciplines.

The Donders Institute has created an environment that stimulates this process in the structure of meetings, seminars and symposia. Also, the curriculum of the Donders graduate school is designed to prepare young talents to become the versatile neuroscientists of the future. And, last but not least, there is the excellent medium run by students, *Proceedings of the Master's Programme Cognitive Neuroscience*, which offers a look into the wide range of research conducted at the Donders Institute.

The current issue is a perfect reflection of the excellence of interdisciplinary research. I wish you a pleasant and stimulating read.

Nijmegen, March 2016

Prof. Dr. Hans van Bokhoven

Head of the reserach line Molecular Neurogenetics
Radboudumc
Donders Centre for Neuroscience

Predicting the Irrelevant: How Expectation Biases Processing

Alexander Horst von Lautz[1,2,3]
Supervisors: Maryann Noonan[1], Yannik Bauer[1], Ole Jensen[2], Mark Stokes[1]

[1]Oxford Centre for Human Brain Activity, University of Oxford, United Kingdom
[2]Radboud University Nijmegen, Donders Institute for Brain, Cognition and Behaviour, The Netherlands
[3]Bernstein Centre for Computational Neuroscience, Charité—Universitätsmedizin Berlin, Germany

Goal-directed behaviour requires selective attention: the process of biasing perception in favour of task-relevant information. Prior knowledge in the form of experience-based expectations heavily influences this function. Although task-irrelevant stimuli appear to recruit similar cognitive resources, recent research indicates that facilitation of targets and inhibition of distractors may constitute separate mechanisms that are likely to exhibit distinct patterns of neuronal activity prior to stimulus onset. Specifically, it has been theorized that power in the alpha band — as measured with electrophysiological methods — reflects such functional inhibition. Here we tested the role of expectations for target and distractor processing with magneto- and electroencephalography (MEG/EEG). In a visual discrimination task we modulated the expected location of relevant and irrelevant stimuli separately to differentiate stimulus specific changes. We found differences in pre-stimulus alpha power lateralization between targets and distractors when expectations about the upcoming location had been built up. Moreover, using a model-based stimulus decoding approach, we could identify quadrant-specific patterns in the alpha band prior to stimulus onset. We speculate that this may be indicative of distinct processes underlying the perception of relevant and irrelevant input.

Keywords: expectations, alpha power, magnetoencephalography, electroencephalography, decoding

Corresponding author: Alexander Horst von Lautz**; E-mail:** alexander.von-lautz@bccn-berlin.de

1. Introduction

The brain relies on its ability to select relevant input for processing, while inhibiting the irrelevant. Prior knowledge in the form of expectations influences this selection and helps us prioritize the vast amount of sensory input at any given moment. Indeed, recent research into the function of the visual cortex demonstrates that expectations about upcoming goal-relevant stimuli bias their sensory representation (Bollinger, Rubens, Zanto, & Gazzaley, 2010; Chelazzi, Miller, Duncan, & Desimone, 1993; Gazzaley & Nobre, 2012; Jiang, Summerfield, & Egner, 2013; Luck, Chelazzi, Hillyard, & Desimone, 1997; Stokes, Thompson, Nobre, & Duncan, 2009). Yet, often we can also predict what information is likely to be irrelevant and distracting: for most tasks the vast majority of sensory input is unrelated and should take up little cognitive resources for optimal processing efficiency (Navalpakkam & Itti, 2007). Thus, suppression of distracting stimuli appears to be a vital complement to facilitation (Gazzaley, Cooney, McEvoy, Knight, & D'esposito, 2005; Kastner, & Ungerleider, 2000; Sylvester, Jack, Corbetta, & Shulman, 2008).

As evidenced by functional magnetic resonance imaging (fMRI) studies, top-down modulations appear to selectively enhance activity in spatiotopic visual areas, a process most likely mediated by a fronto-parietal control network (Gazzaley et al., 2007; Summerfield & Egner, 2009; Zanto, Rubens, Thangavel, & Gazzaley, 2011).

However, while evidence for target facilitation is well-established, it remains largely unknown how an independent mechanism of distractor inhibition could operate. In particular, Soto, Hodsoll, Rotshtein, and Humphreys (2008) provide evidence that stimuli matching the current contents of working memory (WM) are processed automatically, even when they are distracting and therefore detrimental to performance. Hence, if WM-mediated control is inherently facilitatory, distractor inhibition may have to operate autonomously.

In an approach to identify such a separate mechanism, Awh, Matsukura, and Serences (2003) used prior knowledge about upcoming irrelevant information. They demonstrated that when participants had an expectation about distracting input, the behavioural performance cost incurred by processing distractors was reduced. Moreover, expecting irrelevant information did not slow responses when only targets appeared in the subsequent probe. This suggests that participants were able to use distractor expectations in their favour and could do so independent of target processing.

Trying to uncover the neural underpinnings of these effects, Ruff and Driver (2006) used fMRI. They demonstrated the role of distractor inhibition in a binary choice task when information about an upcoming stimulus was given on a trial-by-trial basis. As expected, they found better behavioural performance when participants knew of the future distractor location. Then, contrasting the blood-oxygen-level dependent (BOLD) signal, they discovered changes in anticipatory activity in the occipital cortex corresponding to the expected distractor location. Interestingly, they could not identify activation differences related to target processing. However, their task separated target and distractor processing poorly, as knowledge about the future distractor automatically determined the upcoming target location. Furthermore, the use of fMRI led to difficulties in assessing the directionality of neural correlates. Changes in BOLD are influenced by excitatory as well as inhibitory neural dynamics, thus the increases in BOLD found by Ruff and Driver (2006) cannot be unambiguously attributed to either inhibition or facilitation. Moreover, absolute changes in BOLD may not be directly related to enhanced or diminished information processing, as multivariate approaches have demonstrated (Kok, Jehee, & de Lange, 2012; Summerfield & Egner, 2009).

Recently, results from electrophysiological studies have indicated a link of functional inhibition with low frequency oscillations of neural populations in the alpha band (8-13 Hz), the strongest electrophysiological signal measured from the human waking brain (Berger, 1929; Niedermeyer, & da Silva, 2004). A number of studies show that alpha power synchronizes in cortical areas corresponding to distracting stimuli and desynchronizes in those responsible for current target processing (Kelly, Lalor, Reilly, & Foxe, 2006; Klimesch, 2012; Sauseng et al., 2005; Worden, Foxe, Wang, & Simpson, 2000). Furthermore, Sauseng et al. (2009) demonstrate, with the application of transcranial magnetic stimulation at 10 Hz, that failures of functional inhibition can modulate short term memory capacity. Another link of oscillations in the alpha band and inhibition may be identified through shifts in alpha phase components that serve to limit interference from distracting visual information (Bonnefond & Jensen,

2012). Shifts in alpha power can be observed prior to stimulus onset (Gould, Rushworth, & Nobre, 2011; Mathewson et al., 2014), and may constitute a ubiquitous organising principle in the brain (Jensen, & Mazaheri, 2010). Jensen and Mazaheri (2010) postulate that information is gated through the brain by functional inhibition of task-unrelated areas and that oscillations in the alpha band reflect this process.

However, previous studies have struggled to manipulate distractor expectations separately from target processing. The question remains how such a mechanism could operate independent of WM-mediated control. Moreover, the relationship between top-down modulations of target stimuli and analogous distractor processing continues to be poorly disentangled. Finally, it is unclear how different, that is, how spatially distinct, visual stimuli need to be to make seperate facilitation and inhibition possible. Thus, if an independent inhibitory mechanism exists, on what spatial scale, that is, visual hemifields, does it operate?

In the current study we addressed these questions with a novel task design that modulated spatial target and distractor expectation independently.

In Experiment 1, we used electroencephalography (EEG) to measure brain activity during the task and contrasted pre-stimulus alpha power lateralization between stimulus types and expectation conditions. We hypothesized that contralateral alpha power from occipito-parietal sources decreases when targets are expected and increases for expected distractors.

In Experiment 2 we employed magnetoencephalography (MEG) on the same task to improve spatial resolution. We matched estimates of post-stimulus oscillations in the alpha band to the pre-stimulus activity of different experimental manipulations. This model-based approach differentiated activity from four visual quadrants. We used this match to contrast stimulus and expectation conditions, thereby testing the effects of foreknowledge on target and distractor processing. We expected a better match in alpha power prior to stimulus appearance, when target expectation was high. Activity reflecting the expectation of a relevant stimulus should be similar to activity reflecting actual target appearance. On the other hand, we expected a decreased pattern match when distractors were expected. The activity pattern for predicting irrelevant information should be different to perceiving relevant information.

2. Methods

2.1 Stimuli and Experimental Design

A schematic of the main task can be found in Figure 1. All stimuli were created and displayed using a PC running the MATLAB-based Psychophysics toolbox (Brainard, 1997). The stimuli were presented at a viewing distance of 55 (93 in MEG) cm, 8 (13) cm lateral to the fixation cross, thus with a visual angle of approximately 8 degrees. Each trial started with a pre-stimulus period of 1000 ms in which a black fixation cross appeared on screen. Subsequently, the stimulus display appeared for 200 ms, with both a target and distractor. The target stimuli were round chequered patterns that were constructed by superimposing two Gabor patches (sinusoidal gratings masked by a Gaussian hull). To distinguish two types of patterns, the spatial frequencies of the patches differed. High frequency patterns had 0.0345 cycles per pixel, whereas low frequency patterns showed 0.0275. The distractor stimuli were Gabor gratings with the same parameters as targets, but were superimposed in the same direction, thereby creating a higher perceived intensity than targets. The orientation of the gratings was manipulated in 16 orientations that were randomly assigned on a trial-by-trial basis.

During the main task, participants had to indicate the nature of the target, giving a left-hand response for high frequency targets, or a right-hand response for a low frequency target. After participants had given their response, the trial ended with an auditory feedback: a high tone (900 Hz) marked a correct, while a low tone (500 Hz) marked an incorrect response. Participants were instructed to not move their eyes and explicitly told to not look at the stimuli on screen.

Unknown to participants, we manipulated the spatial predictability of target and distractor stimuli on two levels. For the duration of one block, either target or distractor appeared in one location more often than in the others. Participants could use this experience to build expectations about future stimulus appearances. In the first condition, either the target or distractor appeared with a likelihood of 75% in one of the four quadrant locations. In the second condition, either the target or distractor location remained the same (100%) for one block. We also collected data from a control condition, in which neither stimulus type appeared in one location more often than the others.

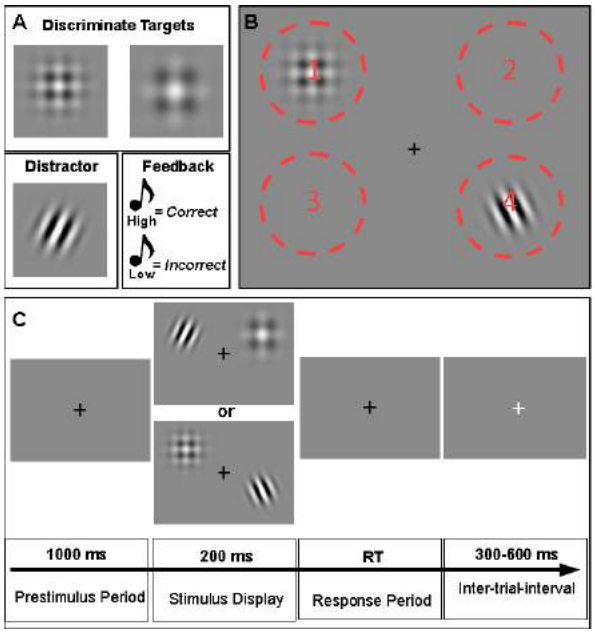

Fig. 1. Schematic of the experimental task. **A.** Participants judged whether targets were high frequency or low frequency chequered patterns. Distractors, on the other hand, were gratings in one of 16 orientations. Auditory feedback was given in form of high and low tones. **B.** Targets and distractors appeared in one of four locations. In the 'Random' condition they appeared in each location with a 25% chance. In the 'Medium Expectation' condition, either target or distractor appeared with 75% certainty in one of the locations for a block of 30 trials. The same was the case in the 'High Expectation' condition, only the location remained the same for all trials with 100% certainty. **C.** One example trial: participants were informed of the prestimulus period by a black fixation cross one second before stimulus presentation; then, a target-distractor pair appeared. Participants judged whether the pattern was low/high frequency by pressing right/left buttons and received auditory feedback. Then the fixation cross turned white to mark the inter-trial interval.

One block consisted of 30 (± 2) trials, one recording session of 6 blocks, and the total experiment consisted of 8 such sessions, totalling 1440 (± 14) trials per subject. After one session of the main task, participants were asked to do a short intermittent task (see Appendix published online: Methods for schematics). Here participants were presented with either a single target or distractor stimulus. By pressing the left or right button, participants indicated whether this had appeared on one or the other side. The stimulus type was irrelevant for this simple response task.

The aim of these intermittent sessions was to estimate the stimulus-driven neural response profiles for each stimulus type and location. In later analyses we used these response profiles to train a forward-model for quadrant-specific stimulus decoding. After one complete session, feedback on the participant's reaction time and accuracy was provided. Participants were asked to aim for at least 90% accuracy while reacting as fast as possible.

2.2 Behavioural Analysis

We recorded reaction time (RT) from stimulus onset and response accuracy during both tasks. We excluded trials in our behavioural analysis that were erroneous, RT outliers and those violating expectation in the 75% condition. RT outliers were defined as responses lying outside the range of triple the median absolute deviation (MAD) (Leys, Ley, Klein, Bernard, & Licata, 2013), a robust measure of scale (Rousseeuw & Croux, 1993). Due to the experimental design, about 180 trials per subject and condition were entered into a 2 x 3 within-subjects repeated measures ANOVA ($\alpha = 0.05$). The factors were stimulus condition (target vs. distractor) and expectation manipulation (no [25%], medium [75%] and high [100%] expectation).

2.3 Experiment 1: EEG

2.3.1 Participants

Twenty-three participants (9 women, 21-37 years old) had normal or corrected-to-normal vision and reported no history of neurological or psychiatric illness. They were screened for compatibility with EEG and gave written informed consent in compliance with local ethics. They received a compensation of £10/h for participating in the study. Four participants were removed from data analysis due to excessive eye movements during EEG acquisition.

2.3.2 EEG Data Acquisition

EEG data were sampled at 1000 Hz on a NeuroScan SynAmps RT amplifier using Scan 4.5 (Compumedics Neuroscan, Charlotte, USA) with 60 Ag/AgCl sintered surface electrodes distributed over the head according to the extended international 10-20 system. The ground was recorded from the anterior midline frontal electrode (AFz), interelectrode impedances kept below 10 k and online referencing to the right mastoid applied. Furthermore, electro-oculographical recordings were made for vertical and horizontal eye movements.

2.3.3 EEG Data Processing

First, we re-referenced the EEG recordings offline to the average of both mastoid electrodes. Using EEGLAB (Delorme & Makeig, 2004) we down-sampled to 250 Hz with 16-bit precision and applied a band-pass filter between 0.05 and 40 Hz. On an individual subject basis, we identified noisy EEG channels via visual inspection and excluded these from further analysis. Excluded channels were mostly from electrodes grouped around lateral temporo-parietal areas (i.e., TP7/8) and lateral frontal areas (F7/F8), thus non-essential recordings for subsequent analyses.

The continuous data was cut into epochs relative to stimulus onset and included a surrounding time window of 1000 ms. Excessive artefacts, blinks, saccades, muscle activity, and excessive signal drift were identified by visually inspecting the epochs. Time points containing these artefacts were removed from following analyses. On this basis, four participants were excluded due to movement-related noise.

2.3.4 Analysis of Alpha Power Lateralization

To investigate the effects of expectation on desynchronization in the alpha band (8-13 Hz), we decomposed the broadband signal from twelve occipital-parietal sensors (O1/2, P1/2, P3/4, P5/6, PO3/4, PO7/8). To do so, the epoched data was transformed into a FieldTrip (Oostenveld, Fries, Maris, & Schoffelen, 2010) file format and a time-frequency representation of power was calculated. We used a Hanning-tapered sliding window Fourier transform at steps of 10 ms for frequencies between 2 and 30 Hz in steps of 1 Hz. We subtracted the average power in the 200 ms before stimulus onset to baseline correct on an individual trial basis. We then averaged power for all experimental conditions for ipsilateral and contralateral sensors with respect to the stimulus presentation. Subsequently, we averaged power in the alpha band between 500 and 0 ms before stimulus onset and tested for effects of lateralized alpha power in a 2 (stimulus type) x 3 (expectation modulation) within-subjects repeated measures ANOVA. As a final step, we performed a permutation-based cluster analysis on all time and frequency points to see whether we could identify any significant differences between conditions (Maris & Oostenveld, 2007).

2.4 Experiment 2: MEG

2.4.1 Participants

Eighteen paricipants (9 female, age range 21-37) participated in the MEG part of this study of which ten had also participated in the EEG part. All participants reported being right handed, having no history of neurological illness and normal or corrected-to-normal vision. They provided written informed consent for being tested according to a protocol approved by the Central University Research Ethics Committee (CUREC). They received a compensation of £10/h for participating in the study. Three subjects were removed from data analysis because of excessive eye movements during the MEG recordings.

2.4.2 MEG Data Acquisition

MEG data were acquired in a magnetically shielded room, on a 306-channel VectorView system (Elekta Neuromag) with two orthogonal planar gradiometers and one magnetometer at each of 102 locations allocated in a helmet surrounding the top of the scalp. During acquisition, a band-pass filter of 0.03-330 Hz was applied and the head position continuously monitored using four head position indicator (HPI) coils attached to the scalp. Before data acquisition, the HPI coil locations, three anatomical fiducial locations — nasion, left and right pre-auricular points — and head points across the scalp were digitized using a Polhemus Isotrak II. Furthermore, to detect eye movements and heartbeat we measured horizontal and vertical electro-oculogram and electrocardiogram via electrodes attached to the eyes and forearm.

2.4.3 Eye-Tracking

Before starting the MEG task, we calibrated an EyeLink 1000 eye-tracking system to an individual's head position. During the MEG task we recorded eye movements continuously to make sure participants did not overtly attended to the stimuli by saccading to them or showed systematic blinks.

2.4.4 MEG Preprocessing

All MEG data were analysed using the FieldTrip toolbox (Oostenveld et al., 2010) and custom-written scripts for MATLAB (The Mathworks Inc.).

First, noisy channels were identified by visually inspecting the data. Then, using the MaxMove (Elekta Neuromag) software, external noise was removed from the MEG data by applying the signal-space separation method (SSS) with its temporal extension (ST). Continuous movement compensation as indicated by the HPI coils was applied and each individual's data transformed to the coordinate frame of their first scanning block. Before conversion to SPM8 format (Friston, Ashburner, Kiebel, Nichols, & Penny, 2007), the continuous data were bandpass filtered at 1-100 Hz, down-sampled to 100 Hz, then cut into epochs with respect to stimulus onset in a time window of -1300 ms to +1000 ms. Time points in which artefacts resulting from muscles, blinks, saccades, and signal drop-out occurred were marked by visually inspecting all trials, and excluded from subsequent analysis steps.

To obtain a time-frequency representation (TFR) of power we applied a sliding Hanning-tapered time window followed by a Fourier transform at steps of 20 ms for frequencies between 5 and 40 Hz at increments of 1 Hz.

2.4.5 Quadrant-Specific Analysis of Alpha Power

The previous EEG analysis was focused on exploring the differences between alpha power lateralization to right and left stimuli in corresponding hemispheres. However, in this task stimuli appeared in one of four locations, a set-up permitting a closer look onto the relationship of expectation and alpha power. Rather than corresponding to the entire hemifield, alpha modulations might be specific to the expected quadrant.

In this task, specifying spatial activity might be crucial to differentiate target and distractor specific activity, as both stimuli could appear in the same hemifield at the same time. Moreover, because we modulated expectations about stimuli for each quadrant, investigating quadrant-specific activity may reduce unwanted variance between quadrants in the same hemifield, thus inherently strengthening contrasts between levels of expectation.

To disentangle quadrant-specific activity we used a forward model to estimate the pattern of alpha power changes following visual stimulation for each quadrant from a separate training dataset (intermittent task), then applied it to the experimental trials for an estimate of specificity for each quadrant. This analysis was based upon encoding models that previously have been applied to fMRI (Brouwer & Heeger, 2009; Serences, & Saproo, 2012) and recently to EEG data sets (Garcia, Srinivasan, & Serences, 2013) to decode colour or orientation of a stimulus.

First, we fitted a general linear model to the trials from our training set to estimate the evoked alpha power in the four quadrants for alpha (8-13 Hz) and a time window of 0-500 ms after stimulus onset. We used a regular least squares estimate to solve the GLM,

$$A = B_1C_1'(C_1C_1')^{-1} \quad [1]$$

where C_1 is a design matrix with four regressors times the number of training trials minus dummy coded for which quadrant the trial is in, B_1 the evoked alpha power at 306 MEG sensors times the number of training trials, and A the weight matrix with 306 sensors times 4 quadrants.

The weight matrix A was used to estimate the specific activity in each quadrant for all time and frequency points of the experimental data set

$$C_2 = (A'A)^{-1} A'B_2 \quad [2]$$

where B2 stores the 306 sensors and frequency responses for each trial.

Figure 2 shows an example of the result of this pattern matching when training and testing on the same training data set (leave-one-out) without any

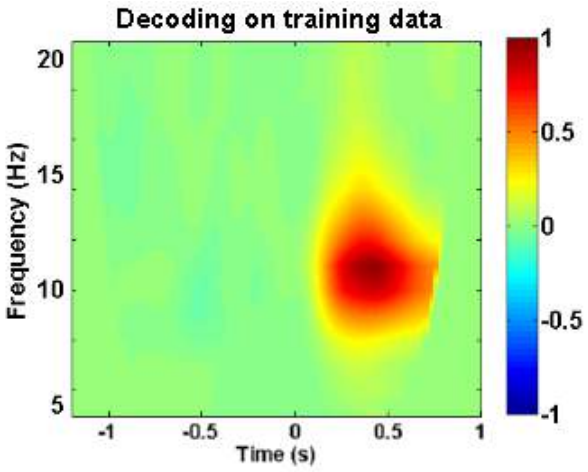

Fig. 2. An example of quadrant decoding (in arbitrary units). This image was made on the basis of leave-one-out training and testing on the same dataset. The model estimate was based on poststimulus response (0-500 ms) in the alpha band (8-13 Hz). This image shows the subtraction of the pattern match for training and testing on the same quadrant (i.e., 1 with 1 in Fig. 1) minus the equivalent diagonal (i.e., 1 with 4 in Fig. 1) fit. The resulting image indicates that there are differences between the patterns of alpha band activity between the two quadrants.

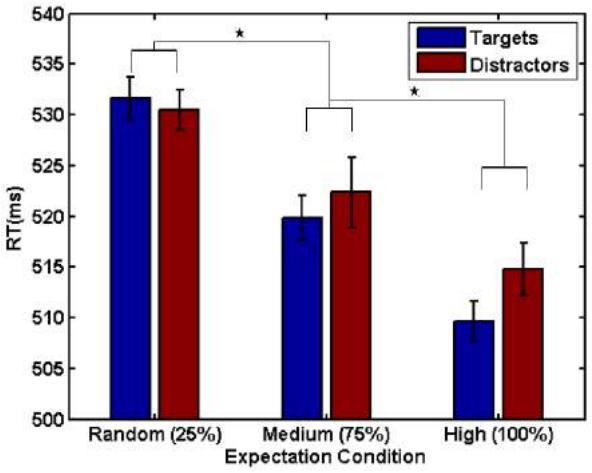

Fig. 3. Mean reaction times of participants in the EEG experiment. Error bars denote one within-subjects standard error.

expectation manipulation. The depicted difference between same quadrant match and diagonal quadrant match indicates how well the forward modelling procedure discriminates between locations. We used this contrast to identify the quadrant-specific differences in alpha power to measure the influence of distractor and target expectation on perceptual processing.

3. Results

3.1 Behavioural Results

Behavioural data confirmed that subjects could use built-up expectations about targets as well as distractors to their advantage. Participants showed very similar reaction time patterns in the EEG and MEG experiments. Because not all subjects participated in both scanning sessions, the following analyses were performed separately for MEG.

Figure 3 shows an overview of the mean reaction times of the three expectation manipulations. It suggests that an increase of spatial predictability of target and distractors results in faster reaction times. Moreover, this effect is similar for targets and distractors. Only when the stimulus was 100% certain to appear in the same location for the entire block, participants seemed to make better use of target than distractor information.

To test these effects statistically, we entered them into a 2 x 3 within-subjects repeated measures ANOVA. This was significant for the factor expectation, $F(2, 36) = 24.36$, $p < .001$ but did not reveal differences between stimulus types $F(1, 36) = 0.77$, $p = .393$. Contrary to our expectation, the interaction stimulus type times expectation

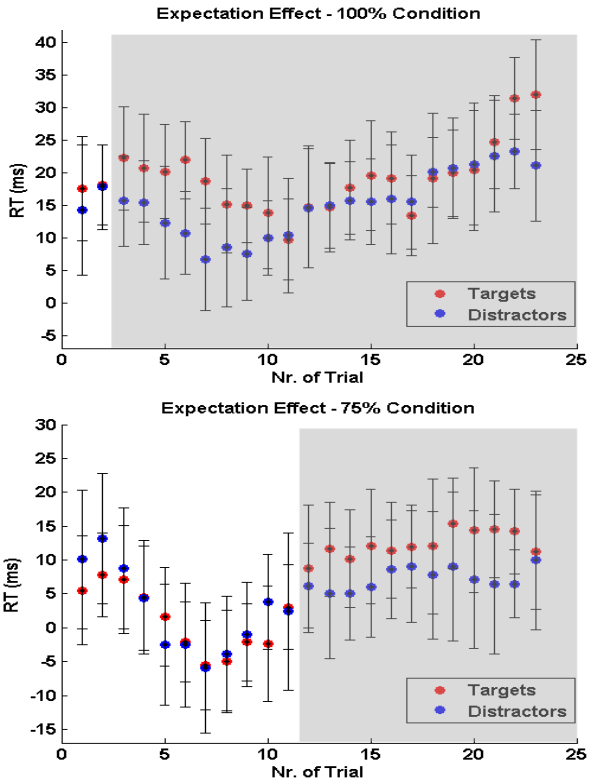

Fig. 4. Difference between expectation and no expectation by trial. Error bars reflect one within-subjects standard error. For visibility reasons, each trial's data was smoothed with a moving average filter, taking into account the surrounding 2 trials. The grey shaded area marks the part of the curve that was significant from zero. **Top.** Mean difference of high expectation (100%) and no expectation (25%) for each trial and stimulus type. **Bottom.** Contrast of medium expectation condition (75%) and no expectation (25%). Note that in this condition only later trials were different from the random condition.

manipulation was not significant $F(2, 36) = 0.45$, $p = .644$. Accuracy scores were overall at 93.1% (± 2.9%) and were entered in a 2 x 3 within-subjects repeated measures ANOVA. This revealed neither an effect for stimulus type $F(1, 36) = 2.05$, $p = .174$, nor for expectation manipulation $F(2, 36) = 0.92$, $p = .406$. We found a significant interaction of stimulus type times expectation manipulation with $F(2, 36) = 3.53$, $p = .039$.

Overall, this indicated that participants were not systematically different in their response accuracies. However, accuracies were numerically higher in the high expectation conditions and more so for targets than distractor manipulations. As indicated by the interaction effect of stimulus type times expectation manipulation, it is possible that there was a speed-accuracy trade-off that led participants to react slower for distractor trials when expectation was high. Thus, while it is difficult to pinpoint the cause, we may be underestimating the reaction time

differences between targets and distractors in the high expectation condition.

If, as hypothesized, expectation builds up over trials in one block, this should be visible when contrasting trials in the expectation manipulations and the control group, where stimuli did not appear in one location more than others. Figure 4 shows this contrast separately for the target and distractor manipulations. To find the difference in reaction time per trial, we subtracted the control condition trials (25% valid) from the high (100% valid, upper panel) and medium (75% valid, lower panel) expectation trials. The top panel, where targets and distractor are 100% predictable, indicates that participants were able to acquire evidence for a certain stimulus position over multiple trials and used this underlying information to better their performance. This expectation effect was not only slightly larger for targets, but increased more quickly than the same contrast for distractors.

The lower panel shows the contrast of valid medium (75% valid) expectation trials versus no (25% valid) expectation trials, calculated in the same manner as in the graph above. Notably, it takes many more trials of the medium expectation condition to identify an expectation effect (grey area, Fig. 4). Both stimulus types were affected in a similar fashion. Comparing the two slopes suggests that when faced with uncertainty, participants need more evidence to benefit from their expectations about upcoming stimuli. Furthermore, the reaction time gain was lower throughout all trials, indicating that participants did not profit as much from expecting a stimulus location with exceeding uncertainty.

3.2 EEG Results

Alpha power has been shown to lateralize when processing relevant and irrelevant information (Kelly et al., 2006; Klimesch, 2012; Sauseng et al., 2005; Worden et al., 2000). Therefore we expected the time-frequency analysis (TFA) of power to show decreases in the contralateral alpha band when expecting target stimuli and increases for distractor expectation. In line with our hypothesis, this pattern seemed to appear as Figure 5 indicates. We found a temporary desynchronization in the alpha band 500 ms before stimulus onset contralateral to the upcoming target location. Furthermore, distractor expectation trials were marked by synchronized activity contralateral to stimulus onset.

Notably, when examining alpha lateralization

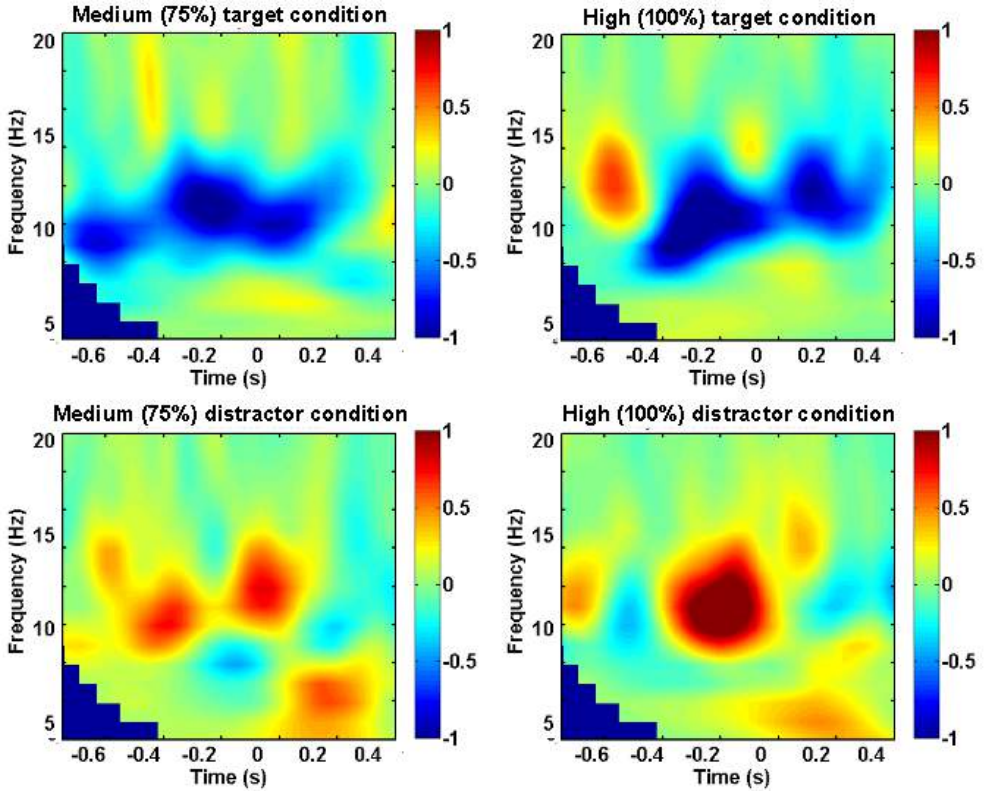

Fig. 5. Contrast of contralateral-ipsilateral power between 4 and 20 Hz (in μV^2) for the expectation manipulations with respect to stimulus onset. The red colour reflects synchronized and blue desynchronized activity. **Top row.** Medium and high target expectation manipulation. **Bottom row.** Medium and high distractor manipulation. Note the prestimulus lateralization difference between the different stimulus types and expectation manipulations.

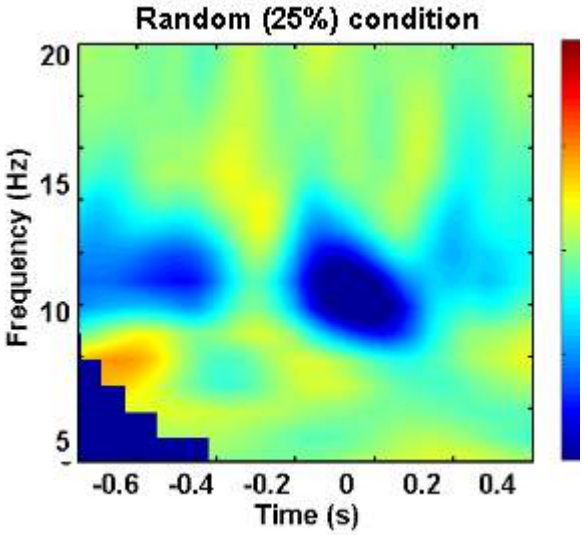

Fig. 6. Lateralized power in the alpha band with respect to target onset in the random condition (in μV^2).

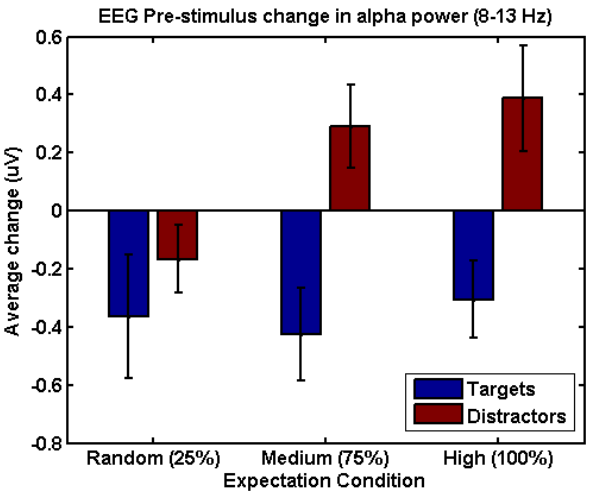

Fig. 7. Prestimulus differences between target and distractor expectation manipulations in the alpha band. Error bars describe one within-subjects standard error.

in the control condition (25%), we found a desynchronization of contralateral alpha similar to that of the target expectation manipulation conditions. Figure 6 shows this same contrast for all trials in which the stimulus locations were assigned randomly. Thus, while distractor expectation seemed to modulate power in the alpha band prior to stimulus onset, target knowledge was not reflected with the same intensity.

To statistically quantify these results, we focused on the alpha power lateralization 0-500 ms before stimulus onset. By averaging over frequencies in the alpha band and all time points in this window of interest, we found differences between expectation manipulations. Figure 7 shows the results of this process. We entered these results in a 2 x 3 within-subjects repeated measures ANOVA for factors stimulus manipulation (target vs. distractor) and expectation manipulations (random, medium, and high expectation trials). This analysis revealed a main effect between targets and distractors $F(1, 36) = 7.87$, $p = .012$, but the factor expectation manipulation was not significant $F(2, 36) = 1.2$, $p = .323$. Unexpectedly, the interaction between these two was also non significant $F(2, 36) = 3.17$, $p = .054$, which was likely due to the large variance in the random data between subjects. This indicates that while there were differences between targets and distractors, these cannot be attributed to the level of expectation. Finally, to test for effects over all frequencies and time points of these conditions, we ran a permutation-based cluster analysis (Maris & Oostenveld, 2007) on each contralateral-ipsilateral power spectrum. This test revealed no significant clusters at $\alpha = 0.05$.

3.3 MEG Results

The quadrant-specific distribution of alpha power in the pre-stimulus interval was reliably modulated by both target and distractor expectation. To measure differences between conditions we had calculated the match between poststimulus alpha power in the training data set (model estimate) and prestimulus power for each of the expectation conditions. Therefore each trial in the main task was matched to four different locations in the training task: a) the same location, b) the other location in the same hemifield, c) the other location on the same height, and d) the diagonal location. A measurement of interest was the difference between same location and diagonal location match as it is indicative of how well the trial distinguished between similar and different locations.

Figure 8 shows this contrast in arbitrary units of match between post-stimulus activity in the training data and prestimulus activity in the main task. It suggests that a relationship between expectations and the match of alpha pattern exists. This relation appears to be in inverse directionality for target and distractor processing. When targets are highly expected in one place (100% condition), the match for the same quadrant increases, while it decreased for the diagonal quadrant.

The inverse is numerically true for expecting distractors. The pattern match is lower for the same quadrant, while it increases in the diagonal opposite. We did not compute statistical tests on this time-frequency window because the unit of this model based match is arbitrary. However, we

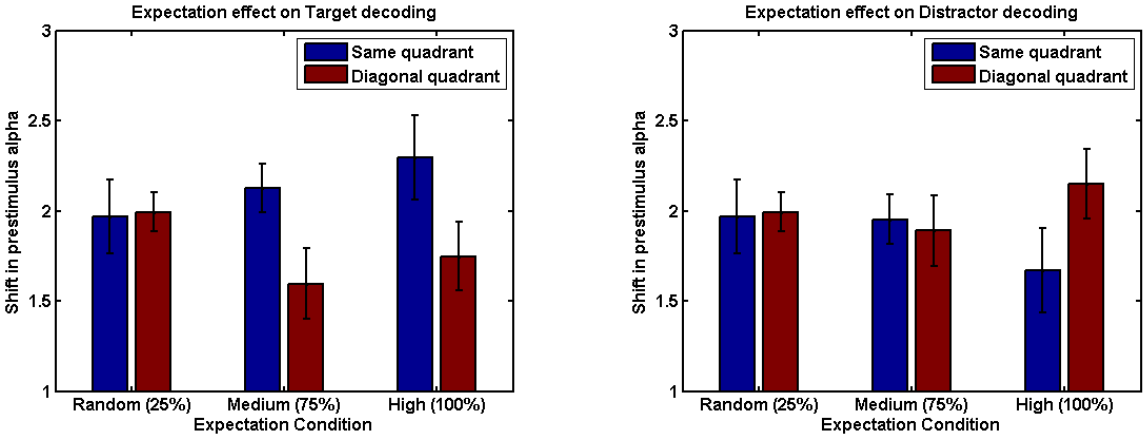

Fig. 8. Target (left) and distractor (right) expectation effects on the difference between same quadrant and diagonal quadrant decoding for the pre-stimulus (One s till onset) time period in the alpha band (8-13 Hz). Error bars denote one within-subjects standard error. The units of this graph are arbitrary and no statistical comparison was made. Numerically, it seems that a relationship between expectations and the pre-stimulus alpha pattern match exists. Note the differences in the high expectation conditions for both stimulus types.

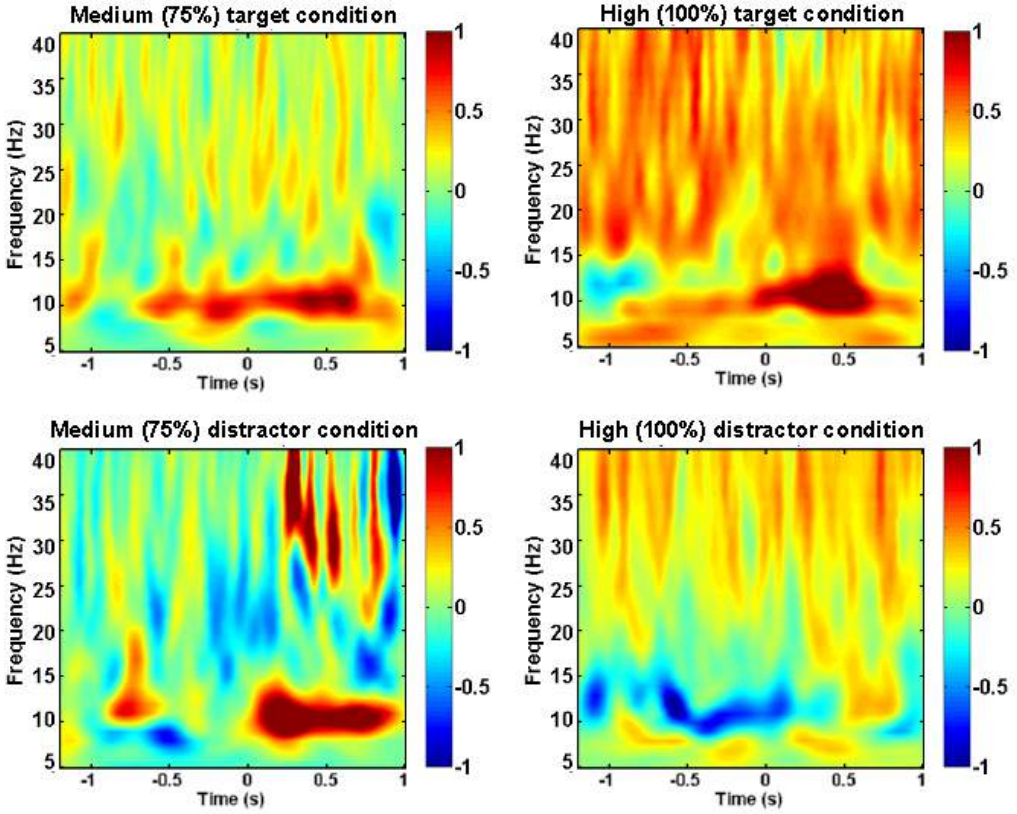

Fig. 9. Results from quadrant decoding for 5-40 Hz for -1.3 to +1 second relative to stimulus onset. The training window was between 0-500 ms after stimulus onset and included frequencies in the alpha band (8-13 Hz). Each individual plot shows the subtraction of same quadrant minus the diagonal quadrant pattern match. **Top row.** medium and high target expectation conditions. **Bottom row.** medium and high distractor expectation conditions. Note the high variance between conditions in the alpha band that looks promising to be used for training classifiers. However, a cluster-based permutation test did not reveal significant clusters for any of these conditions.

performed a cluster-based permutation test on the whole time-frequency range, a simulation based test that makes little assumptions about the data (Maris & Oostenveld, 2007). This analysis did not reveal any clusters in the pre-stimulus period for frequencies in the alpha band (5000 simulations, $\alpha = 0.05$). Figure 9 shows a visualization of these effects for all frequency and time points. The four images show the subtraction of same quadrant match minus the diagonal quadrant match for the expectation manipulations. A consistent modulation of alpha power across the expectation conditions

is clearly visible. As expected, target expectation seemed to increase the match within quadrants, while distractor expectation decreased it. The aforementioned cluster-based permutation test did not reveal any significant clusters. Hence, while the alpha power match between conditions followed the hypothesized pattern numerically, our statistical tests could not identify any significant differences.

4. Discussion

This study investigated how expectations about upcoming target and distractor stimuli bias visual perception. We demonstrated that, when expecting either stimulus, participants reacted faster and showed a differential neural pattern in the alpha band compared to low expectation trials. This effect increased when participants accumulated evidence over trials and when volatility was low.

Our EEG results indicate that expecting a target or distractor on a particular side leads to differential contralateral modulations of power in the alpha band. When participants expected targets, alpha desynchronized, whereas distractor expectation was reflected by synchronized alpha.

Using a model-based location decoding approach on MEG data, we investigated changes in pre-stimulus alpha power patterns. Different levels of expectation appeared to have a relationship with how specific the patterns were to one quadrant. These results were consistent with the hypothesis that experience-based expectations can be used to selectively bias target and distractor processing.

4.1 Expectation Benefits Behaviour

On the psychophysical side we found that expectations about the location of either stimulus led to better behavioural performance. When uncertainty was lower (100% vs. 75% valid trials) this effect increased. Similarly, later trials in a block showed stronger differences between conditions, likely because evidence for one location had accumulated. Furthermore, because expecting a distractor in one location did not determine the target's quadrant, it is plausible that distractor inhibition was not only a by-product of better target discrimination performance. All these findings indicate that experience-based expectations played a selective role for target and distractor processing, prior to stimulus onset.

This is unsurprising; Geng and Behrmann (2005) had demonstrated that uneven distributions of target locations can facilitate processing in a variety of tasks and coined the term 'probability cueing effect' when regularities formed experience with a stimulus type. However, most studies on preparatory modulations of spatial attention focus on target facilitation, leaving out the inhibitory dynamics underlying distractor processing. Evidence from psychophysical studies suggests that such a mechanism could work separately and absent from overt attention. Awh et al. (2003) found that with foreknowledge about the likelihood of their appearance, distractor costs could be reduced when they were located near targets. Moreover, Ruff and Driver (2006) reported that the disruptive influence of a single, spatially remote location could be reduced by covert spatial preparation on a trial by trial basis.

Here, we manipulated expectation directly, and thus can provide further evidence of its central role not only for facilitation, but for selective distractor inhibition.

4.2 Differences in Target and Distractor Processing

Our EEG results indicate that selective modulation of power in the alpha band due to target and distractor expectations can indeed be found in the pre-stimulus interval. As expected, we found differences when contrasting target- and distractor-specific activity in the alpha band between hemispheres, with increases for distractor and decreases for targets contralateral to stimulus location. Surprisingly, this effect was not significant when contrasting levels of expectation (25% vs. 75% vs 100%) in the target condition. Indeed, expectation seemed to have little effect on target-specific pre-stimulus alpha lateralization (Fig. 5).

Alpha lateralization has been shown to predict subsequent visual processing (Rajagovindan & Ding, 2011), visual excitability (Romei et al., *Cereb Cortex*, 2008; Romei et al., *Neuroreport*, 2008), and to correlate with anticipatory changes in ERP (Kelly, Gomez-Ramirez, & Foxe, 2009). Recent approaches to explaining the inhibitory dynamics of perceptual processing assign oscillatory activity in the alpha band the role of a functional inhibitor that gates information away from task irrelevant regions (Jensen & Mazaheri, 2010). Correspondingly, active processing in task-relevant areas would be reflected with a neuronal desynchronization in the alpha band. Thus, considering the lateralization of stimulus processing in the visual cortex, the absence of an expectation effect on target processing-specific

alpha power was unexpected.

One theoretical explanation why we found an effect in pre-stimulus alpha for distractors and not for targets is that gating by inhibition may be more strongly reflected by its inhibitory side. As we did not examine activity in the gamma band (40-100 Hz), the direct relationship of target processing and neuronal oscillations eludes our analysis so far. In future analyses we intend to use the collected MEG recordings to unravel this relationship.

Another reason could have been the short inter-trial-interval of 300-600 ms resulting in a possible contamination from post-stimulus effects of the previous trial. Further analysis, for example, with long epochs ordered by the previous trial, are necessary to overcome these caveats.

An alternative approach could be to base the analysis on a reinforcement learning model that takes into account the trial history, thereby eliminating this possible confound (O'Reilly, 2013). Such a reinforcement learning model could also serve as a better description of the underlying expectation at each trial via a Bayesian learners estimate (Behrens, Woolrich, Walton, & Rushworth, 2007).

Our finding that distractor suppression may be identified prior to stimulus onset raises the question of how such a mechanism could work. Soto et al. (2008) had identified that distractor stimuli held in WM bound more resources, even when this was detrimental to behaviour. If WM-mediated processing is inherently facilitatory, how can we explain the selective suppression effects observed in this task?

An alternative to WM-mediated top-down control is the idea that higher cortical areas influence lower areas to suppress the predictable input, resulting in an elegant strategy to reduce informational redundancy (Friston, 2005; Rao & Ballard, 1999). However, beyond processing efficiency, such predictive coding could offer an explanation of the distractor suppression effect. Indeed, experience of environmental contingencies may form expectations about upcoming stimuli that are used to suppress the predicted input, because the extent of new information is low (Friston & Kiebel, 2009). Consequently distractor inhibition would be inherently favoured, as most sensory information is predictable, hence suppressible.

Therefore, we speculate that two closely interacting, but distinct processes may explain our findings. One, a top-down attentional enhancement of target facilitation and two, a feedback-driven distractor suppression not mediated by working memory, which could be explained by a gating or predictive coding account of perception.

4.3 Quadrant-Specific Alpha Band Oscillations

We identified a relationship between expectation and quadrant-specific decoding accuracy via a forward modelling approach previously used in fMRI (Brouwer & Heeger, 2009; Serences & Saproo, 2012) and EEG (Garcia et al., 2013). The pattern match in distributions of alpha power between training and experimental data was used to contrast same with different stimulus location trials. Expectations about task-relevant and task-irrelevant input appeared to increase this contrast before a stimulus appeared on screen. Due to the preliminary nature of these analyses, it is difficult to interpret the results. The permutation-based cluster analysis did not reveal any significant effects in the pre-stimulus interval for frequencies in the alpha band. This is unsurprising, as our approach had not been optimized for testing differences between conditions.

Training and testing on the full data set of each individual participant and not only on a session's data, will be the first step to increase the power of this analysis. Moreover, we could use this approach to train a classifier (with e.g., support vector machines) to specify the numerical decoding accuracy for a given time/frequency interval between conditions. This could give us a more clear statistical approach to test the decoding accuracy between conditions.

Nonetheless, these analyses address the question of how spatially selective a distractor inhibition mechanism may be. Because there were differences not only between hemifields, but pattern matches seemed distinct for individual quadrants, it is possible that inhibition operates with high spatial acuity. In further analyses we will address this question more thoroughly. It will be interesting to unravel the relationship between same hemifield vs. different hemifield decoding accuracies.

Furthermore, to take into account repetition suppression effects, we will model responses on the basis of the previous trial's location. This way, the distinct role of experience-based expectation for prestimulus location decoding may be investigated without a location-match confound. Also, this could prove to be a more powerful analysis for measurements of spatial selectivity of alpha power.

A related idea has been that expectation about targets elicits short-term increases in activity in the spatiotopic visual cortex. Higher order areas

could access this population better and would be able to store the expected visual features in a more robust representational state (Oberauer, 2013; Olivers, Peters, Houtkamp, & Roelfsema, 2011; Sligte, Scholte, & Lamme, 2008). Distractors, on the other hand, could elicit a short-term decrease in activity in their spatiotopic location, making feature information less accessible.

Thus, we designed distractors to include a feature change independent of targets. This feature — different orientations of the distractor grating — is readily decodable with the same forward modelling approach used to distinguish quadrant-specific activity. The next step in this study will be to measure differences in feature decoding between the expectation conditions. High expectation of distractors should result in less decodability of orientation and in better decoding of target stimulus type (high vs. low frequency grating).

This could also address predictive coding accounts of distractor perception. If expectation sharpens representations in the visual cortex (Kok et al., 2012), we should find better feature representation and higher decodability of target features. Whether the same is true for distractors will be an interesting question to explore.

5. Conclusion

We conclude that pre-stimulus shifts of covert attention to expected items in working memory improve perceptual processing and are marked by shifts in lateralized alpha power. The differences between stimulus types and expectation levels support the idea of independent selective distractor inhibition. Moreover, our results indicate that distractor information may be used in a spatially selective fashion. Whether feature processing is affected by these inhibitory dynamics remains unknown. To tackle this and further questions, we will apply a forward modelling approach to target and distractor feature decoding.

Subsequent analysis will also address where perceptual expectations for relevant and irrelevant input are processed in the brain. The same subjects that took part in the MEG experiment participated in a corresponding fMRI study, which recorded structural scans and diffusion tensor images. To localize expectation dependent changes with MEG, we will employ beamformer analysis to move from sensor to source space.

Acknowledgements

I would like to thank – Dr. Mark Stokes for excellent supervision, Prof. Dr. Ole Jensen for good advice, Yannik Bauer for driving the EEG experiment, Nick Myers for all his time helping with MEG, Dr. Ben Crittenden and Dr. MaryAnn Noonan for their support, Malte Kaller for deciding to do fMRI and everyone else that has helped with the project.

References

Awh, E., Matsukura, M., & Serences, J. T. (2003). Top-down control over biased competition during covert spatial orienting. *Journal of Experimental Psychology: Human Perception and Performance*, *29*, 52–63.

Behrens, T. E., Woolrich, M. W., Walton, M. E., & Rushworth, M. F. (2007). Learning the value of information in an uncertain world. *Nature Neuroscience*, *10*(9), 1214–1221.

Berger, H. (1929). Uber das Elektrenkephalogramm des Menschen. *Archiv fur Psychiatrie und Nervenkrankheiten*, *87*(1), 527–570.

Bollinger, J., Rubens, M. T., Zanto, T. P., & Gazzaley, A. (2010). Expectation-driven changes in cortical functional connectivity influence working memory and long-term memory performance. *The Journal of Neuroscience*, *30*(43), 14399–14410.

Bonnefond, M., & Jensen, O. (2012). Alpha oscillations serve to protect working memory maintenance against anticipated distracters. *Current Biology*, *22*(20), 1969–1974.

Brainard, D. H. (1997). The Psychophysics Toolbox. *Spatial Vision*, *10*(20), 433–436.

Brouwer, G. J., & Heeger, D. J. (2009). Decoding and reconstructing color from responses in human visual cortex. *Journal of Neuroscience*, *29*(44), 13992–14003.

Chelazzi, L., Miller, E. K., Duncan, J., & Desimone, R. (1993). A neural basis for visual search in inferior temporal cortex. *Nature*, *363*(6427), 345–347.

Delorme, A., & Makeig, S. (2004). EEGLAB: an open source toolbox for analysis of single-trial EEG dynamics including independent component analysis. *Journal of Neuroscience Methods*, *134*(1), 9–21.

Friston, K. (2005). A theory of cortical responses. *Philosophical Transactions of the Royal Society B: Biological Sciences*, *360*(1456), 815–836.

Friston, K., Ashburner, J., Kiebel, S., Nichols, T., & Penny, W. (Eds.). (2007). *Statistical parametric mapping: The analysis of functional brain images*. Academic Press. London.

Friston, K., & Kiebel, S. (2009). Predictive coding under the free-energy principle. *Philosophical Transactions of the Royal Society B: Biological Sciences*, *364*(1521), 1211–1221.

Garcia, J. O., Srinivasan, R., & Serences, J. T. (2013). Near-real-time feature-selective modulations in human cortex. *Current Biology*, *23*(6), 515–522.

Gazzaley, A., Cooney, J., McEvoy, K., Knight, R., & D'esposito, M. (2005). Top-down enhancement and suppression of the magnitude and speed of neural activity. *Journal of Cognitive Neuroscience*, *17*(3), 507–517.

Gazzaley, A., & Nobre, A. C. (2012). Top-down modulation: bridging selective attention and working memory. *Trends in Cognitive Sciences*, *16*(2), 129–135.

Gazzaley, A., Rissman, J., Cooney, J., Rutman, A., Seibert, T., Clapp, W., & D'Esposito, M. (2007). Functional interactions between pre-frontal and visual association cortex contribute to top-down modu-lation of visual processing. *Cerebral Cortex*, *17*, 125–135.

Geng, J. J., & Behrmann, M. (2005). Spatial probability as an attentional cue in visual search. *Perception & Psychophysics*, *67*(7), 1252–1268.

Gould, I. C., Rushworth, M. F., & Nobre, A. C. (2011). Indexing the graded allocation of visuospatial attention using anticipatory alpha oscillations. *Journal of Neurophysiology*, *105*(3), 1318–1326.

Händel, B.F., Haarmeier, T., & Jensen, O. (2011). Alpha oscillations correlate with the successful inhibition of unattended stimuli. *Journal of Cognitive Neuroscience*, *23*, 2494–2502.

Jensen, O., & Mazaheri, A. (2010). Shaping functional architecture by oscillatory alpha activity: gating by inhibition. *Frontiers in Human Neuroscience*, *4*, 186.

Jiang, J., Summerfield, C., & Egner, T. (2013). Attention sharpens the distinction between expected and unexpected percepts in the visual brain. *Journal of Neuroscience*, *33*(47), 18438–18447.

Kastner, S., & Ungerleider, L. G. (2000). Mechanisms of visual attention in the human cortex. *Annual Reviews Neuroscience*, *23*, 315–341.

Kelly, S. P., Gomez-Ramirez, M., & Foxe, J. J. (2009). The strength of anticipatory spatial biasing predicts target discrimination at attended locations: a high-density EEG study. *European Journal of Neuroscience*, *30*(11), 2224–2234.

Kelly, S. P., Lalor, E. C., Reilly, R. B., & Foxe, J. J. (2006). Increases in alpha oscillatory power reflect an active retinotopic mechanism for distracter suppression during sustained visuospatial attention. *Journal of Neurophysiology*, *95*(6), 3844–3851.

Klimesch, W. (2012, Dec). Alpha-band oscillations, attention, and controlled access to stored information. *Trends in Cognitive Sciences*, *16*(12), 606–617.

Klimesch, W., Sauseng, P., & Hanslmayr, S. (2007) EEG alpha oscillations: The inhibition-timing hypothesis. *Brain Research Review*, *53*(1), 63–88.

Kok, P., Jehee, J. F. M., & de Lange, F. P. (2012). Less is more: Expectation sharpens representations in the primary visual cortex. *Neuron*, *75*(2), 265–270.

Leys, C., Ley, C., Klein, O., Bernard, P., & Licata, L. (2013). Detecting outliers: Do not use standard deviation around the mean, use absolute deviation around the median. *Journal of Experimental Social Psychology*, *49*(4), 764–766.

Luck, S. J., Chelazzi, L., Hillyard, S. A., & Desimone, R. (1997). Neural mechanisms of spatial selective attention in areas V1, V2, and V4 of macaque visual cortex. *Journal of Neurophysiology*, *77*(1), 24–42.

Maris, E., & Oostenveld, R. (2007). Nonparametric statistical testing of EEG- and MEG-data. *Journal of Neuroscience Methods*, *164*(1), 177–190.

Mathewson, K. E., Beck, D. M., Ro, T., Maclin, E. L., Low, K. A., Fabiani, M., & Gratton, G. (2014). Dynamics of alpha control: Preparatory suppression of posterior alpha oscillations by frontal modulators revealed with combined EEG and event-related optical signal. *Journal of Cognitive Neuroscience*, *26*(10), 2400–2415.

Navalpakkam, V., & Itti, L. (2007). Search goal tunes visual features optimally. *Neuron*, *53*(4), 605–617.

Niedermeyer, E., & da Silva, F. L. (2004). *Electroencephalography: Basic Principles, Clinical Applications, and Related Fields* (5th ed.). Lippincott Williams & Wilkins.

Oberauer, K. (2013). The focus of attention in working memory-from metaphors to mechanisms. *Frontiers Human Neuroscience*, *7*, 673.

Olivers, C. N., Peters, J., Houtkamp, R., & Roelfsema, P. R. (2011). Different states in visual working memory: when it guides attention and when it does not. *Trends in Cognitive Science*, *15*(7), 327–334.

Oostenveld, R., Fries, P., Maris, E., & Schoffelen, J. M. (2010). Fieldtrip: open source software for advanced analysis of MEG, EEG, and invasive electrophysiological data. *Computational Intelligence and Neuroscience*, *2011*.

O'Reilly, J. X. (2013). Making predictions in a changing world — inference, uncertainty, and learning. *Frontiers in Neuroscience*, *7*, 105.

Rajagovindan, R., & Ding, M. (2011). From prestimulus alpha oscillation to visual-evoked response: an inverted-U function and its attentional modulation. *Journal of Cognitive Neuroscience*, *23*(6), 1379–1394.

Rao, R. P., & Ballard, D. H. (1999). Predictive coding in the visual cortex: a functional interpretation of some extra-classical receptive-field effects. *Nature Neuroscience*, *2*(1), 79–87.

Romei, V., Brodbeck, V., Michel, C., Amedi, A., Pascual-Leone, A., & Thut, G. (2008). Spontaneous fluctuations in posterior alpha-band EEG activity reflect variability in excitability of human visual areas. *Cerebral Cortex*, *18*(9), 2010–2018.

Romei, V., Rihs, T., Brodbeck, V., & Thut, G. (2008). Resting electroencephalogram alpha-power over posterior sites indexes baseline visual cortex excitability. *Neuroreport*, *19*(2), 203–208.

Rousseeuw, P. J., & Croux, C. (1993). Alternatives to the median absolute deviation. *Journal of the American Statistical Association*, *88*(424), 1273–1283.

Ruff, C. C., & Driver, J. (2006). Attentional preparation for a lat-eralized visual distractor: behavioral and fMRI evidence. *Journal of Cognitive Neuroscience*, *18*(4), 522–538.

Sauseng, P., Klimesch, W., Stadler, W., Schabus, M., Doppelmayr, M., Hanslmayr, S., Birbaumer, N. (2005). A shift of visual spatial attention is selectively associated with human EEG alpha activity. *European Journal of Neuroscience*, *22*(11), 2917–2926.

Serences, J. T., & Saproo, S. (2012). Computational advances towards linking BOLD and behavior. *Neuropsychologia*, *50*(4), 435–446.

Sligte, I. G., Scholte, H. S., & Lamme, V. A. (2008). Are there multiple visual short-term memory stores? *PLOS one*, *3*(2), e1699.

Soto, D., Hodsoll, J., Rotshtein, P., & Humphreys, G. W. (2008, September). Automatic guidance of attention from working memory. *Trends in Cognitive Sciences*, *12*(9), 342–348.

Stokes, M., Thompson, R., Nobre, A. C., & Duncan, J. (2009). Shape-specific preparatory activity mediates attention to targets in human visual cortex. *Proceedings of the National Academy of Sciences*, *106*(46), 19569–19574

Summerfield, C., & Egner, T. (2009). Expectation (and attention) in visual cognition. *Trends in Cognitive Science*, *13*(9), 403–409.

Sylvester, C. M., Jack, A. I., Corbetta, M., & Shulman, G. L. (2008). Anticipatory suppression of nonattended locations in visual cortex marks target location and predicts perception. *The Journal of Neuroscience*, *28*(26), 6549–6556.

Worden, M. S., Foxe, J. J., Wang, N., & Simpson, G. V. (2000). Anticipatory biasing of visuospatial attention indexed by retinotopically specific alpha-band electroencephalography increases over occipital cortex. *Journal of Neuroscience*, *20*(6), RC63.

Zanto, T. P., Rubens, M. T., Thangavel, A., & Gazzaley, A. (2011). Causal role of the prefrontal cortex in top-down modulation of visual processing and working memory. *Nature Neuroscience*, *14*(5), 656–661.

Expanding the PDZD7 Interactome: PDZD7 Connects the Usher Protein Complex to WNT Signaling and Intraflagellar Transport

Leoni A. Creemers[1]
Supervisors: Erik de Vrieze[2], Erwin van Wijk[2,3], Hannie Kremer[1,2,3]

[1]Radboud University Medical Center Nijmegen, Donders Institute for Brain, Cognition and Behaviour, Department of Human Genetics, The Netherlands
[2]Radboud University Medical Center Nijmegen, Donders Institute for Brain, Cognition and Behaviour, Department of Otorhinolaryngology, The Netherlands
[3]Radboud Institute for Molecular Life Sciences, The Netherlands

Usher syndrome (USH) is the leading genetic cause of deaf-blindness. Mutations in *PDZD7* have been found to modify USH, and its gene product PDZ domain-containing 7 (PDZD7) is a paralog of the scaffold proteins whirlin and harmonin. Previous studies have connected PDZD7 to the USH interactome, through the interactions with several USH proteins. Previously identified putative interactors include intraflagellar transport (IFT) proteins and molecules involved in the Wnt signaling pathway. Here, we tried to expand and validate the interactome of PDZD7 in relation to these modules. Novel candidate interactors were found in yeast two-hybrid analyses and include Wnt signaling molecules β-catenin, LZTS2, CBY1 and YWHAE, and IFT protein IFT57. Co-localization studies showed that PDZD7 overlaps with CBY1 and YWHAE, but not with β-catenin, which indicates an indirect role for PDZD7 in Wnt signaling. Possibly, PDZD7 plays a role in the formation of a signaling hub, as several regulators of Wnt signaling were identified as putative interactors. Co-immunoprecipitation experiments revealed interactions between PDZD7 and IFT25 and IFT27, but not IFT57. This indicates that PDZD7 may be responsible for the pre-assembly and/or trafficking of the USH2 complex. In this report we provide the first evidence that IFT and Wnt signaling may be linked to USH.

Keywords: PDZD7, interactome, Usher syndrome, intraflagellar transport (IFT), Wnt signaling

Corresponding author: Leoni A. Creemers; **E-mail**: leoni1990@gmail.com

1. Introduction

Usher syndrome (USH) is a recessively inherited disorder resulting in sensorineural hearing loss and retinitis pigmentosa (RP), and has been associated with vestibular dysfunction. Its prevalence is estimated to be 3 to 6 per 100,000 depending on population and region (Boughman, Vernon, & Shaver, 1983; Grondahl, 1987; Marazita et al., 1993; Rosenberg, Haim, Hauch, & Parving, 1997; Sadeghi, Kimberling, Tranebjœrg, & Möller, 2004; Spandau & Rohrschneider, 2002). There are three clinical subtypes of USH, defined by the severity and progression of hearing loss and the presence or absence of vestibular dysfunction. RP is common in all subtypes although the age of onset differs per subtype. USH type I (USH1) is the most severe subtype and is characterized by congenital profound hearing loss, RP onset before puberty and vestibular dysfunction (vestibular arreflexia). Type II (USH2), the most prevalent form, presents with congenital moderate to severe hearing loss and RP onset during or after puberty. Patients diagnosed with the third subtype (USH3) suffer from progressive hearing loss, variable vestibular function and variable onset of RP.

To date, ten genes and four loci have been implicated in Usher syndrome. For USH1, six genes and three more loci have been described: *USH1B*, encoding actin-binding molecular motor myosin VIIa (D Weil et al., 1995), *USH1C* (Bitner-Glindzicz et al., 2000; Smith et al., 1992; Verpy et al., 2000) and *USH1G* (Mustapha et al., 2002; Dominique Weil et al., 2003), encoding the scaffold proteins harmonin and SANS, respectively. *USH1D* (Bolz et al., 2001; Bork et al., 2001; Wayne et al., 1996) and *USH1F* (Ahmed et al., 2001; Alagramam et al., 2001) encode the transmembrane cell adhesion molecules cadherin 23 and protocadherin 15, respectively, and *USH1J* (Riazuddin et al., 2012) encodes the calcium binding protein CIB2. The three loci are USH1E (Chaïb et al., 1997), USH1H (Ahmed, Riazuddin, Khan, Friedman, & Friedman, 2009) and USH1K (Jaworek et al., 2012). For USH2, three genes are known: *USH2A* (Eudy et al., 1998; Kimberling et al., 1990) and *USH2C* (Pieke-Dahl et al., 2000; Weston, Luijendijk, Humphrey, Möller, & Kimberling, 2004), encoding the large G protein-coupled receptors USH2A and GPR98, respectively, and *USH2D* (van Wijk et al., 2006), which encodes the scaffold protein whirlin. USH3 is caused by mutations in *USH3A*, the gene for the transmembrane cell adhesion protein clarin-1 (Adato et al., 2002; Fields et al., 2002; Joensuu et al., 2001; Sankila et al., 1995). Furthermore, a locus, USH3B, has been described for USH3 (Puffenberger et al., 2012). A subset of USH mutations are also associated with non-syndromic hearing loss or autosomal recessive RP (Kremer, van Wijk, Märker, Wolfrum, & Roepman, 2006; Saihan, Webster, Luxon, & Bitner-Glindzicz, 2009).

The USH proteins are part of a functional network, the Usher interactome, located in cochlear hair cells and the photoreceptor cells (Kremer et al., 2006; Maerker et al., 2008; Reiners, Nagel-Wolfrum, Jürgens, Märker, & Wolfrum, 2006). Scaffolding proteins SANS, harmonin and whirlin play a central role in this interactome because of their interactions with both USH1 and USH2 proteins. Interactions between USH proteins and harmonin and whirlin occur mostly through their PDZ domains. A typical PDZ domain consists of ~90 amino acid residues and often binds to short amino acid sequences located on the C-terminal tails of target proteins (PDZ binding motifs), although some also bind to internal motifs of the interacting proteins and other PDZ domains (Garner, Nash, & Huganir, 2000; Lee & Zheng, 2010). Proteins containing PDZ domains play critical roles in various biological processes including cell polarity and maintenance, organization of receptor and ion channel signaling, and connecting cytoskeletal structures with membranes (Ye & Zhang, 2013). The Usher interactome is believed to be involved in the development and structural integrity of the stereocilia and mechanotransduction in the inner ear. In photoreceptor cells, the complex is thought to play a role in the trafficking of vesicular cargo between inner and outer segments and in cell structure at the periciliary region (Blanco-Sánchez, Clément, Fierro, Washbourne, & Westerfield, 2014; Cosgrove & Zallocchi, 2014; Kremer et al., 2006). Furthermore, USH proteins have also been found to localize around the synapse of photoreceptor cells and cochlear hair cells, where they are suggested to be involved in synaptogenesis and maintenance (for a recent review, see Cosgrove & Zallocchi, 2014).

A possible candidate gene for Usher syndrome is PDZ domain-containing 7 (*PDZD7*). This protein has previously been associated with USH: when mutated it aggravates the RP symptoms in USH2 patients and it is proposed to contribute to digenic USH (Ebermann et al., 2010; Schneider et al., 2009). Furthermore, PDZD7 shares significant homology with whirlin and harmonin (Ebermann et al., 2010; Schneider et al., 2009): they contain three PDZ domains and one proline-rich region, which suggests that PDZD7 could have a similar function as whirlin

and harmonin in the Usher interactome.

In vitro studies have shown that PDZD7 interacts with USH2A, GPR98, harmonin, whirlin and SANS (Ebermann et al., 2010; Schneider et al., 2009; Zou et al., 2014). Recently, PDZD7 was found to inhibit the GPR98-Gαi pathway by binding to the β-subunit of GPR98, thereby blocking GPR98β-subunit-mediated inhibition of adenylate cyclase (Hu et al., 2014). In *Pdzd7* knockout mice, the lack of PDZD7 led to the disorganization of stereocilia bundles and a reduction in the mechanotransduction currents and sensitivity in cochlear outer hair cells (Zou et al., 2014). Moreover, knockdown of zebrafish Pdzd7 resulted in photoreceptor death and mislocalization of Gpr98 (Ebermann et al., 2010). The same study also showed that Pdzd7 localizes beneath the kinocilia in cochlear hair cells and at the connecting cilium in photoreceptor cells. A more detailed localization study in rats showed that PDZD7 localizes to the ankle links of cochlear and vestibular hair cells, overlapping with whirlin, USH2A and GPR98 (Grati et al., 2012). However, rod and cone photoreceptors functioned normally in *Pdzd7* null mice, in line with other USH mice models. At the molecular level, PDZD7 acted as an organizer of the USH2 complex in cochlear hair cells (Zou et al., 2014).

In the host lab, putative interaction partners of PDZD7 were identified using yeast two-hybrid and tandem affinity purification experiments (unpublished findings Erwin van Wijk and Ronald Roepman). The list of putative interactors included intraflagellar transport (IFT) proteins and molecules involved in Wnt signaling (Table 1). Because IFT is required for ciliogenesis, and Wnt signaling mediates orientation of outer hair cell stereocilia, proteins involved in these two pathways are of particular interest to understand the pathogenesis of USH. The putative interactors, identified by van Wijk and Roepman, indicate that PDZD7 may function as a scaffold protein that links Wnt signaling and IFT to USH. In this study, we have validated the preliminary interaction data via various techniques, and provide the first evidence that PDZD7 interacts with proteins involved in intraflagellar transport and Wnt signaling.

2. Materials and Methods

2.1 DNA constructs

Entry clones containing the coding sequences were available in-house for all genes (*PDZD7, LZTS2, CTNNB1, IFT25, IFT27, IFT57* [NCBI Reference Sequence/GenBank: FJ617449, NM_032429.2, AY463360.1, NM_016126.2, NM_001177701.2 and NM_018010.3, respectively]). For PDZD7,

Table 1. Summary of results of unpublished tandem affinity purification and yeast two-hybrid screen experiments. The tandem affinity purification experiment was performed with HEK293T cells. The yeast two-hybrid screen was performed against a human and bovine retinal cDNA library, in which the reporter genes were strongly (++) or adequately (+) activated. The entire list of PDZD7 interactors through tandem affinity purification and yeast two-hybrid assays can be found in Table S1 and Table S2 respectively.

Identity gene	**Function**	**Tandem affinity purification**	**Yeast two-hybrid library screen**	
		Sequence coverage	α assay	β assay
PDZD7		0.78		
MARK2	Involved in Wnt signaling	0.61		
MARK3	Involved in Wnt signaling	0.49		
CSNK2A2	Participates in several signaling pathways	0.42		
CSNK2B	Possibly participates in Wnt signaling	0.42		
MARK1	Positive regulator of the Wnt signaling pathway	0.41		
CSNK2A1	Participates in several signaling pathways	0.39		
IFT25	Component of IFT-B core complex	0.25		
IFT27	Component of IFT-B core complex	0.13		
IFT74	Component of IFT-B core complex	0.07		
IFT81	Component of IFT-B core complex	0.05		
LZTS2	Negative regulator of the Wnt signaling pathway		++	++
CTNNB1	Key downstream component of the canonical Wnt signaling pathway		++	+

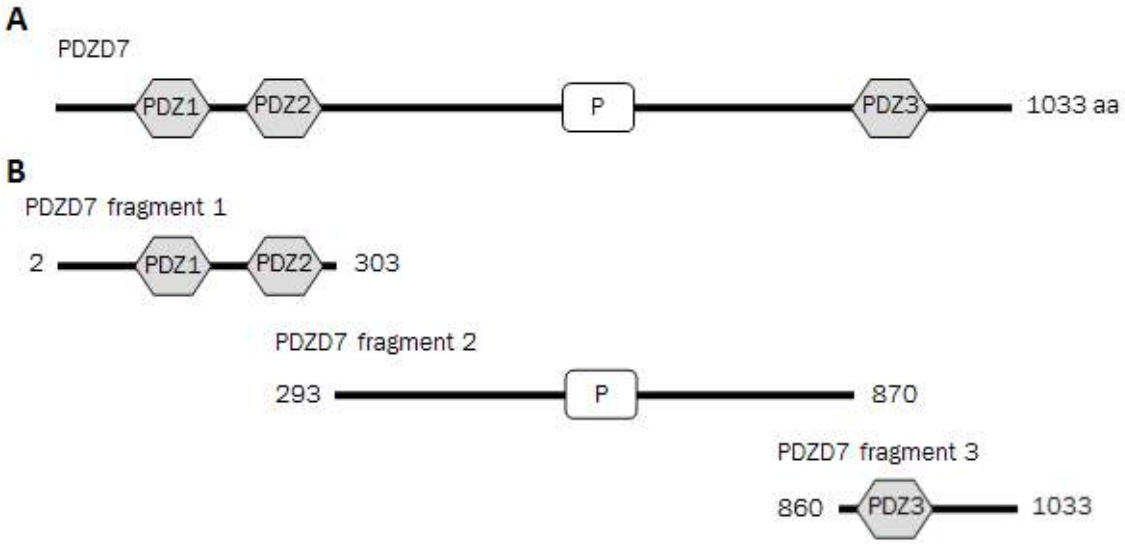

Fig. 1. Schematic representation of PDZD7 and the three fragments. ***A.*** The full length protein is 1033 amino acids long and consists of three PDZ domains (PDZ1, PDZ2 and PDZ3) and one proline-rich domain (P). ***B.*** Fragment 1 of PDZD7 contained the first two PDZ domains. PDZD7 fragment 2 contained the proline-rich domain (P). Fragment 3 contained the last PDZ domain. The three different fragments of PDZD7 were used in the yeast two-hybrid assays. The numbers represent amino acids (aa).

four constructs were used, one encoding the full-length PDZD7 and 3 different fragments (fragment 1: aa 2-303; fragment 2: aa 293-870; fragment 3: aa 860-1033; Fig. 1). Expression clones for yeast two-hybrid (pAD, pBD) or expression in cultured cells (pDest-733 [monomeric red fluorescent protein; mRFP], p3xhemagglutinin (HA) and p3xflag) were generated by performing Gateway cloning (Life Technologies, Carlsbad, CA, USA) according to the manufacturer's instructions.

2.2 Yeast two-hybrid assays

To identify binary interactors of PDZD7, a GAL4-based yeast two-hybrid system (HybriZAP, Stratagene, La Jolla, USA) was used. Genes of interest were fused both to a DNA-binding domain and an activation domain and subsequently transformed into PJ69-4A and PJ69-4α yeast cells, respectively, which contain the HIS3 (histidine), ADE2 (adenine), MEL1 (α-galactosidase) and LacZ (β-galactosidase) reporter genes. All constructs containing the pBD-domain were tested for auto-activation prior to screening for interactors.

All four PDZD7 constructs were used to screen the in-house 1 on 1 yeast two-hybrid grid containing 199 BD and 230 AD ciliary gene clones (kindly donated by Ronald Roepman). In addition, cotransformations of identified interactors were performed to validate the interaction. Interactions between β-catenin or LZTS2 and PDZD7 were tested with cotransformations. The strength of the identified interaction was evaluated via the activation of the *HIS3* and *ADE2* reporter genes via transfer to selective growth media, α-galactosidase colorimetric plate assays (*MEL1* reporter gene) and β-galactosidase filter lift assays (*LacZ* reporter gene). Inserts of putative interaction partners were verified using Sanger Sequencing.

2.3 Immunocytochemistry

The intracellular localization of PDZD7 and its potential binding partners was assessed by transfection with N-terminal monomeric red fluorescent protein (mRFP) and/or enhanced cyan fluorescent protein (eCFP) fusion constructs. Human TERT-immortalized Retinal Pigment Epithelium 1 cells (hTERT-RPE1) were cultured in a 1:1 mixture of DMEM AQ and F12, supplemented with 10% (v/v) fetal calf serum (FCS), 1% (v/v) sodium pyruvate (NaPyr) and 1% (v/v) Penicillin/Streptomycin (all from Sigma-Aldrich, St. Louis, MO, USA). Cells were seeded on sterile microscope glass slides and subjected to serum starvation (0.2% FCS) at 70-80% confluency to induce cilium formation. After 24 h, the ciliated cells were (co-) transfected with the fluorescently labelled constructs using lipofectamine2000 (Life Technologies). For this purpose, lipofectamine was 100x diluted in OptiMEM (Sigma-Aldrich) and incubated at room temperature for 10 min. The DNA was taken up in

Table 2. Yeast two-hybrid assays against a ciliary gene grid revealed EPS8, YWHAE, GID8, IFT57, CRB2, SPAG5, USH2A, GPR98, DNALI1, CEP290, NINL^{isoB}, CDR2 and CBY1 as binding partners of PDZD7. Of these proteins YWHAE, GID8, IFT57, USH2A, GPR98, DNALI1, CEP290 and NINL^{isoB} could be validated in cotransformations. Furthermore, interactions between PDZD7 and either LZTS2 or β-catenin were found upon cotransformation. The β assay of the 1 on 1 screen was performed twice, therefore, the scores given are an average of the two. In the last column, the bait count of the proteins in all yeast two-hybrid grid screens performed in the past can be found. All interactors with bait count over 10 were regarded as potential false positives. The reporter genes were either strongly activated (++), adequately activated (+), weakly activated (+/-), not activated (-) or not assayed (NA). The entire list of PDZD7 interactors can be found in Table S3.

Bait	1 on 1 Screen		Dedicated 1 on 1		Prey identity	Overall bait count grid
	α assay	β assay	α assay	β assay		
pAD PDZD7 full-length	NA	++	-	-	pBD hEPS8 1-211	19
pAD PDZD7 fragment 1	NA	+/-	NA	NA	pBD hEPS8 551-616	19
pAD PDZD7 fragment 1	NA	++	-	-	pBD hEPS8 1-211	19
pAD PDZD7 fragment 2	NA	++	-	-	pBD hEPS8 1-211	19
pAD PDZD7 fragment 2	NA	+/-	-	+	pBD YWHAE	6
pAD PDZD7 fragment 3	NA	+/-	-	+	pBD GID8	13
pAD PDZD7 fragment 3	NA	+/-	NA	NA	pBD hEPS8 551-616	19
pAD PDZD7 fragment 3	NA	++	-	-	pBD hEPS8 1-211	19
pAD PDZD7 fragment 3	NA	+/-	-	+	pBD IFT57	11
pAD PDZD7 fragment 3	NA	++	NA	NA	pBD hCRB2-icd	0
pBD PDZD7 full length	-	+/-	NA	NA	pAD SPAG5 1115-1190	17
pBD PDZD7 full length	+/-	-	-	+	pAD USH2A-icd	0
pBD PDZD7 full length	-	+/-	+/-	++	pAD GPR98	0
pBD PDZD7 full length	-	+/-	-	+	pAD DNALI1	0
pBD PDZD7 fragment 1	-	+/-	-	+	pAD CEP290 cc456	8
pBD PDZD7 fragment 1	++	++	-	-	pAD GPR98	0
pBD PDZD7 fragment 1	-	+/-	-	+	pAD NINL^{isoB} full-length	10
pBD PDZD7 fragment 2	++	++	-	-	pAD CDR2	14
pBD PDZD7 fragment 2	+	++	-	-	pAD SPAG5 774-1193	17
pBD PDZD7 fragment 3	++	++	-	-	pAD CBY1	4
pBD PDZD7 full length	NA	NA	-	+	pAD LZTS2	/
pBD PDZD7 fragment 1	NA	NA	+	++	pAD β-catenin	/
pBD PDZD7 fragment 1	NA	NA	-	+	pAD LZTS2	/
pBD PDZD7 fragment 3	NA	NA	-	+/-	pAD LZTS2	/

250 µl OptiMEM and incubated for 5 min at room temperature. Next, the lipofectamine solution was added to the DNA solution, and incubated for 20 min at room temperature. The serum starvation medium was refreshed and transfection mixture was added to the cells. Six h after transfection, medium was refreshed once more. Twenty-four h after transfection, the cells were rinsed with phosphate buffered saline (PBS) and fixed with 2% paraformaldehyde in PBS for 20 min. The fixed cells were washed with PBS, permeabilized for 10 min with 1% (v/v) Triton X-100 in PBS and incubated in blocking buffer (2% (w/v) bovine serum albumin in PBS) for 20 min. Then, the cells were stained for 1 hour with monoclonal mouse α-polyglutamylated tubulin (GT335, 1:500, generously provided by Carsten Janke, CNRS Centre de Recherches en Biochimie Macromoleculaire, Montpellier, France), monoclonal mouse α-intraflagellar transport 57 (IFT57, 1:300, Abnova, Taipei City, Taiwan), polyclonal rabbit α-β-catenin (1:500, Life Technologies), monoclonal mouse α-active β-catenin (1:100, Millipore, Billerica, MA, USA) and/or polyclonal rabbit α-flag (1:1000, Sigma Aldrich) diluted in blocking buffer. Subsequently, the cells were washed three times with PBS and incubated for 45 min in blocking buffer containing a 500-fold dilution of the appropriate secondary antibodies

(goat α-mouse Alexa Fluor 647, goat α-rabbit Alexa Fluor 488, goat α-mouse Alexa Fluor 488, goat α-rabbit Alexa Fluor 647, goat α-mouse Alexa Fluor 568; all from Life Technologies). The stained cells were washed three times with PBS and once shortly with MQ, after which the coverslips were mounted on microscope slides using Vectashield with DAPI (Vector Laboratories, Burlingame, CA, USA). Images were taken with a Zeiss Axio Imager Z1 fluorescence microscope (Zeiss, Oberkochen, Germany), equipped with a 63x objective and an apotome and were processed using Adobe Photoshop (Adobe Systems, San Jose, CA, USA).

2.4 Co-immunoprecipitation

To validate the binding of PDZD7 and its potential binding partners in vivo, a co-immunoprecipitation experiment was performed with N-terminal 3xHA and 3xflag fusion constructs.

HEK293T cells were grown in medium containing DMEM AQ, 10% (v/v) FCS, 1% (v/v) NaPyr and 1% (v/v) Penicillin/Streptomycin. After 24 h, the cells were co-transfected with the 3xflag- or 3xHA-tagged constructs using polyethylenimine (PEI, Polysciences, Warrington, PA, USA). A total of 2 μg DNA was transfected by adding 90 μl PEI to the DNA. After 10 min of incubation, the mixture was added to the cells. As a positive control the interaction between 3xHA-whirlin and 3xflag-USH2A was used; as negative control 3xflag-STRAD was transfected with the IFTs and PDZD7. Forty-eight h after transfection, the cells were washed with PBS and were lysed on ice in lysis buffer (50 mM Tris-HCl (pH 7.5), 150 mM NaCl, 0.5% Triton-X-100) supplemented with complete protease inhibitor cocktail (Roche Diagnostics). Lysates were centrifuged and the supernatants were put in new eppendorf tubes. For immunoprecipitation, 40 μl of mouse monoclonal α-flag M2 beads (Sigma-Aldrich) and rat monoclonal α-HA beads (Roche, Basel, Switzerland) per sample were washed three times with cold lysis buffer. Subsequently, the lysates were incubated with either the α-flag beads or the α-HA beads in lysis buffer (Vtot=400μl) for two h on a rotating wheel at 4 °C. After incubation, the beads were washed four times with cold lysis buffer after which they were taken up in 1x LDS Sampling Buffer NuPage supplemented with 150 μl dithiothreitol (DTT) and incubated at 70 °C for 10 min. The co-immunoprecipitation samples were run on 4-12% NuPage gradient gels (Life Technologies). The presence of 3xflag-PDZD7 and the 3xHA-tagged IFTs was analyzed by immunoblotting with polyclonal rabbit α-HA (1:500, Sigma-Aldrich) or α-flag (1:1000, Sigma-Aldrich) as primary antibody and goat α-rabbit IRDye800 (LI-COR, Lincoln, NE, USA) as a secondary antibody. Bands were visualized by using the Odyssey Infrared Imaging System (LI-COR) and images were processed using Odyssey V3.0 software (LI-COR).

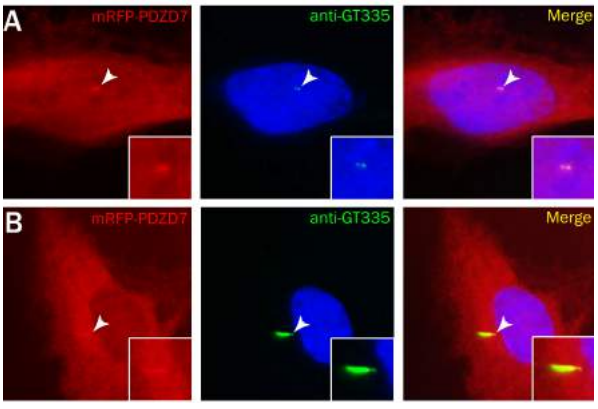

Fig. 2. Localization of mRFP-PDZD7 in single transfected hTERT-RPE1 cells. **A.** PDZD7 localized in the cytoplasm and basal bodies. Approximately 50% of the cells were ciliated. **B.** Occasionally, PDZD7 localized in the cilium. GT335 was used as basal body and cilium marker. The nucleus was stained by DAPI.

3. Results

3.1 Putative PDZD7 interactors include proteins involved in Wnt signaling and IFT

A yeast two-hybrid screen of a grid containing approximately 200 ciliary gene clones was performed to identify binary interactors of PDZD7. For this, the full-length protein and three fragments of PDZD7 were used (Fig. 1). Analysis of positive clones that activated all reporter genes revealed thirteen ciliary proteins as potential binding partners, of which eight were validated in cotransformations (Table 2). These putative binding partners are: YWHAE, GID8, IFT57, USH2A, GPR98, DNALI1, CEP290 and NINL^{isoB}. The complete results of the yeast two-hybrid grid screen are shown in Table S3. Furthermore, cotransformations of LZTS2 and β-catenin (both previously identified in yeast two-hybrid retinal cDNA library screens; Table 1), with the four PDZD7 constructs confirmed both proteins as potential binding partners of full-length PDZD7 and PDZD7 fragment 1.

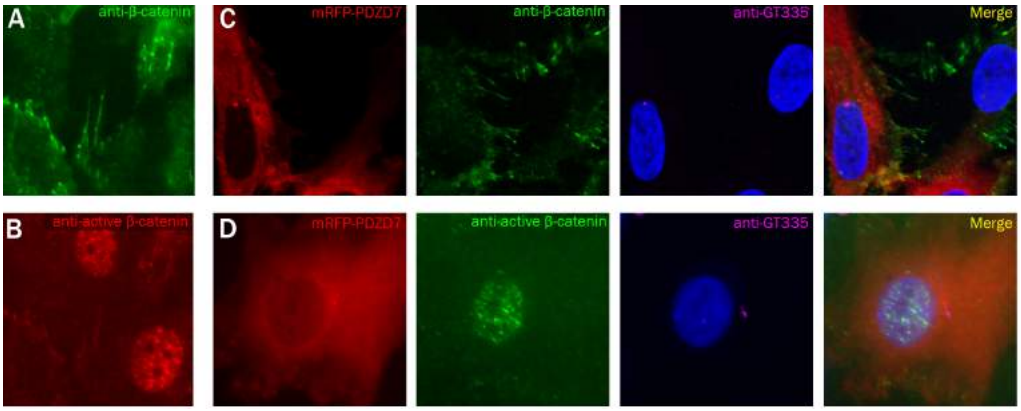

Fig. 3. (Co-)Localization studies in hTERT-RPE1 cells. **A.** Antibody staining showed localization of β-catenin in the cytoplasm and in the cell-cell junctions. **B.** Active β-catenin, stained by an antibody, mainly localized in vesicles in the cell nucleus. **C.** No co-localization of PDZD7 and β-catenin was found. **D.** The co-localization of PDZD7 and active β-catenin was not present either. Moreover, the localization of (active) β-catenin and intensity of the signal didn't seem to change after overexpression of PDZD7. GT335 was used as basal body and cilium marker. The nucleus was stained by DAPI.

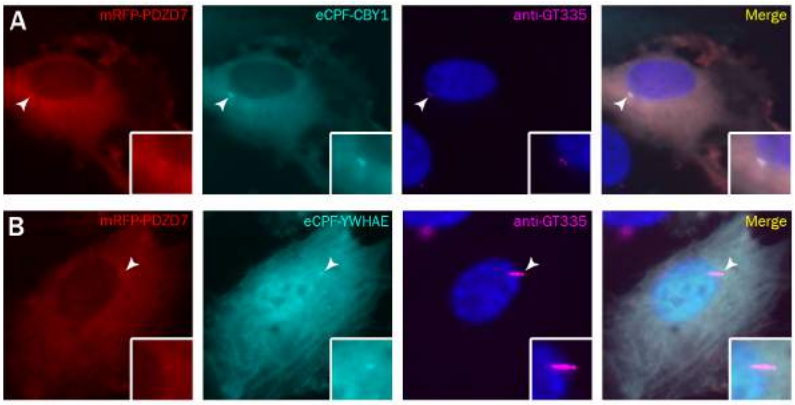

Fig. 4. Co-localization studies in hTERT-RPE1 cells. **A.** PDZD7 co-localized with eCFP-CBY1 in the basal bodies and in the cytoplasm. **B.** Co-localization was also found between PDZD7 and eCFP-YWHAE in the basal bodies and cytoplasm. GT335 was used as basal body and cilium marker. The nucleus was stained by DAPI.

3.2 PDZD7 co-localizes with CBY1 and YWHAE at the basal bodies

In single-transfected hTERT-RPE1 cells, mRFP-PDZD7 was found in the cytoplasm and was enriched at the basal bodies (Fig. 2A). Furthermore, in some cells PDZD7 seemed to localize in the primary cilium (Fig. 2B). Antibody staining showed that β-catenin localized to the cytoplasm and is enriched in the cell-cell junctions, while active β-catenin mainly localized in vesicles in the cell nucleus (Fig. 3A and B). Co-localization studies of mRFP-PDZD7 and endogenous β-catenin (active and inactive) showed no overlap in fluorescent signals of these two proteins (Fig. 3C, D). Furthermore, the localization of (active) β-catenin and the intensity of the staining did not seem to change upon overexpression of PDZD7. Immunocytochemical stainings with two different antibodies against IFT57 were not yet successful and need further optimization. Cells that were transfected with mRFP-PDZD7 and eCFP-CBY1 showed co-localization in the basal bodies and in the cytoplasm (Fig. 4A). mRFP-PDZD7 and eCFP-YWHAE co-localized as well in the basal bodies and cytoplasm (Fig. 4B). The localization of PDZD7 upon overexpression of either CBY1 or YWHAE did not change.

3.3 PDZD7 interacts with IFT25 and IFT27

To examine the interaction between PDZD7 and several of the identified IFT molecules in a mammalian cell system, HEK293T cells were transfected with HA- and flag-tagged PDZD7 and IFT proteins. IFT25, IFT27 and IFT57 were selected as the top candidates from the previously performed tandem affinity purification experiment (Table 1) and the yeast two-hybrid experiments (Table 2). We performed immunoprecipitation assays using anti-flag beads and found that full-length flag-PDZD7 co-immunoprecipitated with HA-IFT25, HA-IFT27 and HA-IFT57 (Fig. 5A, lanes 1-3). However, the negative control flag-STRAD also co-immunoprecipitated, albeit less, with HA-IFT25, HA-IFT27, HA-IFT57 and HA-PDZD7 (Fig. 5A, lanes 4-7). Reciprocal immunoprecipitation experiments using anti-HA antibodies confirmed

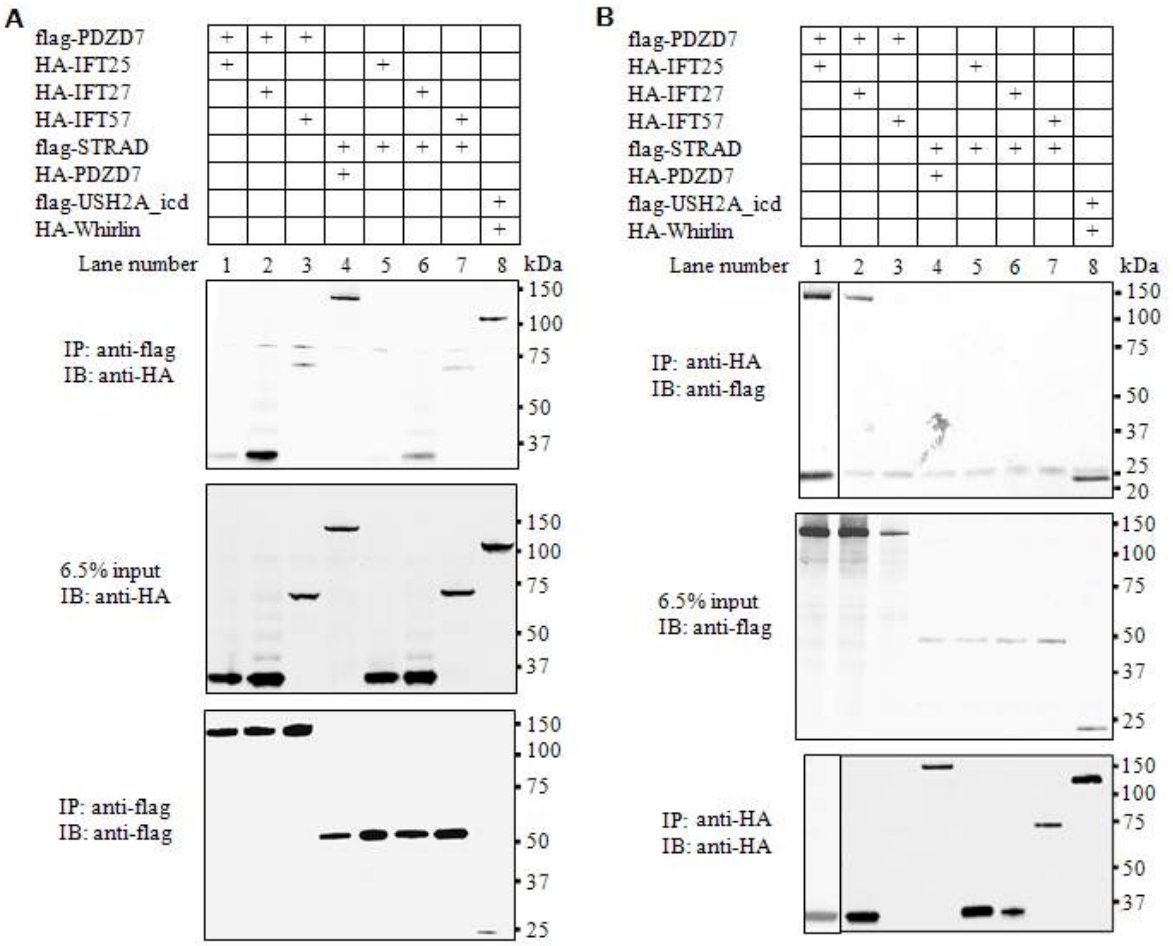

Fig. 5. Co-immunoprecipitation experiments of PDZD7 with IFT25, IFT27 and IFT57. **A.** The immunoblot (IB) in the upper panel shows that flag-PDZD7 co-immunoprecipitated with HA-IFT25, HA-IFT27 and HA-IFT57 (lane 1-3). However, the negative control flag-STRAD also co-immunoprecipitates with HA-IFT25, HA-IFT27 and HA-IFT57, albeit less, as well as with HA-PDZD7 (lane 4-7). Also, the positive control interaction is clearly present (lane 8). Protein input is shown in the middle panel; the anti-flag immunoprecipitates are shown in the bottom panel. **B.** Reciprocal immunoprecipitation assay. The immunoblot (IB) in the top panel revealed that flag-PDZD7 (protein input shown in the middle panel) co-immunoprecipitated with HA-IFT25 (lane 1) and HA-IFT27 (lane 2), but not with HA-IFT57 (lane 3). Moreover, the unrelated protein flag-STRAD did not co-immunoprecipitate any of the HA-IFTs or HA-PDZD7 (lane 3-7). The positive control interaction is clearly visible in lane 8. The anti-HA immunoprecipitates are shown in the bottom panel, in which the expression of HA-IFT57 in lane 3 is absent. The results of the expression test for the anti-flag IB in A, and the anti-HA IB in B, can be found in Fig. S1.

the interaction between flag-PDZD7 and HA-IFT25 and HA-IFT27 (Fig. 5B, lanes 1, 2). The interaction with IFT57 could not be confirmed as it was not expressed (Fig. 5B, lane 3). In this experiment, the negative control did not co-precipitate with our proteins of interest (Fig. 5B, lane 3-7).

4. Discussion

Here we report on the expansion of the interactome of PDZD7. We identified several proteins involved in Wnt signaling as putative interactors of PDZD7 via yeast two-hybrid experiments. Additionally, we confirmed interactions with IFT25 and IFT27, previously identified in tandem-affinity purification studies, via co-immunoprecipitation experiments. Based on our results, we propose that PDZD7 connects the USH-protein network to the intraflagellar transport B module.

Putative interactors of PDZD7, identified via yeast two-hybrid assays, are USH2A, GPR98, CRB2, SPAG5, DNALI1, CEP290, NINL^{isoB}, β-catenin, LZTS2, CBY1, YWHAE and IFT57. Three more putative interactors (EPS8, GID8 and CDR2) were identified as false positives. Many of the putative interactors are associated with other ciliopathies or isolated blindness. For example, CRB2 has previously been associated with retinitis pigmentosa and Leber congenital amaurosis (van den Hurk et al., 2005). Another interactor, CEP290 has been associated

with isolated blindness and many ciliopathies, such as LCA and Joubert syndrome (Coppieters, Lefever, Leroy, & De Baere, 2010). Interactions between PDZD7 and USH proteins USH2A and GPR98 have been described before (Ebermann et al., 2010; Grati et al., 2012; Hu et al., 2014; Zou et al., 2014) and could be confirmed in our study. NINL^{isoB} is a trafficking protein that has been found to interact with USH2A (van Wijk et al., 2009). SPAG5 interacts with both NINL^{isoB} and USH2A and this complex is hypothesized to play a role in microtubule-based cytoplasmic trafficking of proteins essential for cilium formation and function (Kersten et al., 2012). However, SPAG5 may be a false positive as it is a commonly identified interactor in screens of our in-house ciliary yeast two-hybrid grid. IFT57 is often found as a hit in yeast two-hybrid analyses as well, and may therefore be characterized as false positive. The ciliary yeast-two hybrid grid was previously screened using all known IFT proteins as bait, which might explain the abundance of IFT57 amongst preys identified in all screens so far. As several IFT-B complex members were identified in the tandem affinity purification experiments by Roepman and colleagues (unpublished data, Table S1), we included IFT57 in further studies. Since the protein interactions were identified in an artificial yeast two-hybrid environment, additional validation is required for all putative interactors. Because Wnt and IFT proteins were identified in previous protein-protein interaction studies with PDZD7, we focused on these two protein modules.

Wnt signaling is the collective term for the three signaling pathways that are activated by the binding of a Wnt-protein to a Frizzled family receptor. The first, the canonical Wnt/β-catenin pathway, is responsible for the regulation of gene transcription. The second, the noncanonical planar cell polarity (PCP) pathway, modulates the cytoskeleton. Lastly, the noncanonical Wnt/calcium pathway is amongst others involved in the regulation of gene expression and cardiac differentiation via intracellular calcium signaling (Brembeck, Rosário, & Birchmeier, 2006; Rao & Kühl, 2010). Wnt signaling and the cilium are strongly associated: the basal body region acts as a focal point for Wnt signaling (May-Simera & Kelley, 2012). Additionally, many ciliary proteins are required for Wnt signaling and downstream effector regulation (May-Simera & Kelley, 2012).

From our list of putative interactors, we speculate a link between PDZD7 and Wnt signaling, because we identified several Wnt signaling molecules that interact with PDZD7. We and others have demonstrated that PDZD7 localizes to the basal bodies of primary cilia (Ebermann et al., 2010). Our co-localization experiments showed that PDZD7 overlaps with CBY1 and YWHAE, but not with (active) β-catenin. Moreover, localization of (active) β-catenin was not altered upon overexpression of PDZD7. If interactions between PDZD7 and β-catenin indeed take place *in vivo*, they are likely transient. Furthermore, enrichment of Wnt signaling molecules at the basal body is well described (May-Simera & Kelley, 2012). Our results are in favor of an indirect role for PDZD7 in Wnt signaling, since PDZD7 does not co-localize with β-catenin. Possibly, PDZD7 plays a role in the formation of a signaling hub, as there are several regulators of Wnt signaling among the putative interactors (Table 1 and 2). The hypothesis of signaling hub formation is strengthened by the fact that LZTS2 also co-localizes with PDZD7 (Gorris, 2011, unpublished data, Table S2). It may be possible that PDZD7 forms this signaling hub to modulate transduction efficiency, as both LZTS2 and the combination of CBY1 and YWHAE are known to inhibit β-catenin (Li, Mofunanya, Harris, & Takemaru, 2008; Takemaru et al., 2003; Takemaru, Fischer, & Li, 2009; Thyssen et al., 2006). However, this hypothesis should be validated in the future.

A potential role for PDZD7 in Wnt signaling is substantiated by the phenotype of PDZD7 knockout mice, which have disorganized and titled stereocilia (Zou et al., 2014). Knockout mice for receptors of the planar cell polarity pathway show a highly similar phenotype (Wang, Guo, & Nathans, 2006). The similarity in these phenotypes, combined with the findings presented in this report, indicate that PDZD7 may indeed be involved in Wnt signaling.

IFT involves the movement of protein complexes from the basal body to the ciliary tip and back, and is essential for cilium formation and maintenance, for example in the kinocilium of hair cells and connecting cilium of photoreceptor cells (Ishikawa & Marshall, 2011; Maerker et al., 2008). IFT particles are constructed from at least 20 proteins that are organized in two subcomplexes, complex A and complex B, responsible for the retrograde and anterograde transport, respectively (Ishikawa & Marshall, 2011). All IFT proteins that were discovered to (potentially) interact with PDZD7 are members of IFT-B complex.

To investigate whether PDZD7 and the IFT-B complex reside in the same cellular compartment, a requirement for physical interaction, we performed a co-localization study for PDZD7 and IFT57. Although not successful in our hands, IFT57 localizes to the ciliary base and axoneme (Machteld

Oud, personal communication, July 25, 2014). In photoreceptor cells, IFT proteins are enriched at the base and tip of the connecting cilium, as well as the synapse. This places PDZD7 in the same compartment as other USH proteins, overlapping with the published localization of IFT-B at the ciliary base (Gorris, 2011; Sedmak & Wolfrum, 2010).

Anti-HA co-immunoprecipitation confirmed the interactions between PDZD7 and IFT25, and PDZD7 and IFT27, but was unsuccessful for IFT57 due to technical issues. The anti-flag co-immunoprecipitation should be repeated with a different negative control in order to draw unambiguous conclusions on the interaction between PDZD7 and IFT57. IFT25 and IFT27 have been described to form a sub-complex within the IFT-B complex, which may be involved in the regulation of IFT, and consequently ciliogenesis (Wang, Fan, Williamson, & Qin, 2009). Dimerization of IFT25 and IFT27 gives rise to a new protein-binding motif (Bhogaraju, Taschner, Morawetz, Basquin, & Lorentzen, 2011), which could possibly interact with PDZD7. The function of this small module is, as of yet, poorly known, but may hold the clue to understanding why PDZD7 interacts with the IFT-B complex.

The notion that PDZD7 interacts with both USH and IFT proteins suggests that PDZD7 could be involved in trafficking USH proteins by IFT. Or, PDZD7 could be involved in the pre-assembly of the USH2 complex at the basal bodies. Findings in the literature state that Gpr98 is mislocalized in photoreceptor cells of Pdzd7 morphant fish (Ebermann et al., 2010), which suggest that Pdzd7 plays are role in the transport of Gpr98.

Currently, few *in vivo* studies have been performed to examine the consequences of IFT25 and/or IFT27 knockout on cilia formation and functioning. IFT5 null mouse apparently have no defects in cilium formation, but show depletion of IFT27 in embryonic fibroblasts and altered hedgehog signaling (Keady et al., 2012). In trypanosomes, IFT27 is required for cilia formation, as loss of IFT27 results in short, stumpy flagella (Huet et al., 2014). Recently, a study in *Ift27* null mice has shown IFT27 is not required for ciliation, but is required for IFT25 entry into cilia. Depletion of IFT27 also leads to altered hedgehog signaling in these mice, which causes severe ciliopathy hallmarks and death after birth (Eguether et al., 2014). In humans, mutations in IFT27 are causative for Bardet-Biedl Syndrome, a syndromic ciliopathy that includes, amongst others, retinitis pigmentosa and hearing loss (Aldahmesh et al., 2014). The contradicting findings suggest that either the function of IFT27 in cilia formation is lost in higher vertebrates or might only exist in some cell types not interrogated in the current studies (Davis & Katsanis, 2014). If IFT27 indeed plays a role in transport of the USH2 complex, future experiments should reveal that Pdzd7 and USH2 proteins are mislocalized in these morphants.

A recent study found that PDZD7 acts as an organizer of the USH2 complex in cochlear hair cells (Zou et al., 2014). We suggest that PDZD7 may have a similar function in photoreceptor cells. In vivo experiments and/or proximity ligation assays could shed more light on the organizational function of PDZD7 in the eye and the ear. It is not unlikely that the two modules (IFT and Wnt) are of different importance based on cell type. The phenotype of Wnt signaling deficient mice shows the importance of Wnt signaling in the formation of hair cells. Perhaps the interactions between PDZD7 and Wnt signaling molecules are more important in the inner ear compared to the retina. The mislocalization of Gpr98 in Pdzd7 morphant zebrafish suggests that Pdzd7 in the retina could relate to transport of USH complex proteins.

Pending further validation, our results imply a role for PDZD7 in Wnt signaling via the potential interactions with several modulators of the Wnt signaling pathway. Furthermore, PDZD7 is a prime candidate for the long hypothesized functional connection between USH proteins and the IFT machinery. The extensive proteomics dataset gathered here presents PDZD7 as an important protein in various aspects of cilium function and ciliary signaling.

Supplementary material can be found on the journal website www.ru.nl/master/cns/journal/.

Acknowledgements

I would like to thank Prof. Dr. Hannie Kremer for the opportunity to do my internship in her research group. Additionally, I would like to thank Erik de Vrieze for his supervision on the project and for teaching me the various techniques used in the experiments. Lisette van Esch-Hetterschijt and Stef Letteboer, thank you for your assistance and help, and for teaching me the skills I needed for this research. To all my colleagues, thanks for a great time in the lab, I enjoyed it!

References

Adato, A., Vreugde, S., Joensuu, T., Avidan, N., Hamalainen, R., Belenkiy, O., … & Lancet, D. (2002). USH3A transcripts encode clarin-1, a four-transmembrane-domain protein with a possible role in sensory synapses. *European Journal of Human Genetics: EJHG*, *10*(6), 339–350.

Ahmed, Z. M., Riazuddin, S., Bernstein, S. L., Ahmed, Z., Khan, S., Griffith, A. J., … & Wilcox, E. R. (2001). Mutations of the protocadherin gene PCDH15 cause Usher syndrome type 1F. *American Journal of Human Genetics*, *69*(1), 25–34.

Ahmed, Z. M., Riazuddin, S., Khan, S. N., Friedman, P. L., & Friedman, T. B. (2009). USH1H, a novel locus for type I Usher syndrome, maps to chromosome 15q22-23. *Clinical Genetics*, *75*(1), 86–91.

Alagramam, K. N., Yuan, H., Kuehn, M. H., Murcia, C. L., Wayne, S., Srisailpathy, C. R., … & Hagemen, G. S. (2001). Mutations in the novel protocadherin PCDH15 cause Usher syndrome type 1F. *Human Molecular Genetics*, *10*(16), 1709–1718.

Aldahmesh, M. A, Li, Y., Alhashem, A., Anazi, S., Alkuraya, H., Hashem, M., … & Alkuraya, F. S. (2014). IFT27, encoding a small GTPase component of IFT particles, is mutated in a consanguineous family with Bardet-Biedl syndrome. *Human Molecular Genetics*, *23*(12), 3307–3315.

Bhogaraju, S., Taschner, M., Morawetz, M., Basquin, C., & Lorentzen, E. (2011). Crystal structure of the intraflagellar transport complex 25/27. *The EMBO Journal*, *30*(10), 1907–1918.

Bitner-Glindzicz, M., Lindley, K. J., Rutland, P., Blaydon, D., Smith, V. V, Milla, P. J., … & Glaser, B. (2000). A recessive contiguous gene deletion causing infantile hyperinsulinism, enteropathy and deafness identifies the Usher type 1C gene. *Nature Genetics*, *26(1)*, 56–60.

Blanco-Sánchez, B., Clément, A., Fierro, J., Washbourne, P., & Westerfield, M. (2014). Complexes of Usher proteins preassemble at the endoplasmic reticulum and are required for trafficking and ER homeostasis. *Disease Models & Mechanisms*, *7*(5), 547–559.

Bolz, H., von Brederlow, B., Ramírez, A., Bryda, E. C., Kutsche, K., Nothwang, H. G., … & Kubisch, C. (2001). Mutation of CDH23, encoding a new member of the cadherin gene family, causes Usher syndrome type 1D. *Nature Genetics*, *27*(1), 108–112.

Bork, J. M., Peters, L. M., Riazuddin, S., Bernstein, S. L., Ahmed, Z. M., Ness, S. L., … & Morell, R. J. (2001). Usher syndrome 1D and nonsyndromic autosomal recessive deafness DFNB12 are caused by allelic mutations of the novel cadherin-like gene CDH23. *American Journal of Human Genetics*, *68*(1), 26–37.

Boughman, J. A., Vernon, M., & Shaver, K. A. (1983). Usher syndrome: definition and estimate of prevalence from two high-risk populations. *Journal of Chronic Diseases*, *36*(8), 595–603.

Brembeck, F. H., Rosário, M., & Birchmeier, W. (2006). Balancing cell adhesion and Wnt signaling, the key role of beta-catenin. *Current Opinion in Genetics & Development*, *16*(1), 51–59.

Chaïb, H., Kaplan, J., Gerber, S., Vincent, C., Ayadi, H., Slim, R., … & Petit, C. (1997). A newly identified locus for Usher syndrome type I, USH1E, maps to chromosome 21q21. *Human Molecular Genetics*, *6*(1), 27–31.

Coppieters, F., Lefever, S., Leroy, B. P., & De Baere, E. (2010). CEP290, a gene with many faces: mutation overview and presentation of CEP290base. H*uman Mutation*, *31*(10), 1097–1108.

Cosgrove, D., & Zallocchi, M. (2014). Usher protein functions in hair cells and photoreceptors. *The International Journal of Biochemistry & Cell Biology*, *46*(30), 80–89.

Davis, E. E., & Katsanis, N. (2014). Dissecting Intraflagellar Transport, One Molecule at a Time. *Developmental Cell*, *31*(3), 263–264.

Ebermann, I., Phillips, J. B., Liebau, M. C., Koenekoop, R. K., Schermer, B., Lopez, I., … & Bolz, H. J. (2010). PDZD7 is a modifier of retinal disease and a contributor to digenic Usher syndrome. *The Journal of Clinical Investigation*, *120*(6), 1812–1823.

Eguether, T., San Agustin, J. T., Keady, B. T., Jonassen, J. A., Liang, Y., Francis, R., … & Pazour, G. J. (2014). IFT27 Links the BBSome to IFT for Maintenance of the Ciliary Signaling Compartment. *Developmental Cell*, *31*(3), 279–290.

Eudy, J. D., Weston, M. D., Yao, S., Hoover, D. M., Rehm, H. L., Ma-Edmonds, M., … & Sumegi, J. (1998). Mutation of a gene encoding a protein with extracellular matrix motifs in Usher syndrome type IIa. *Science*, *280*(5370), 1753–1757.

Fields, R. R., Zhou, G., Huang, D., Davis, J. R., Möller, C., Jacobson, S. G., … & Sumegi, J. (2002). Usher syndrome type III: revised genomic structure of the USH3 gene and identification of novel mutations. *American Journal of Human Genetics*, *71*(3), 607–617.

Garner, C. C., Nash, J., & Huganir, R. L. (2000). PDZ domains in synapse assembly and signalling. *Trends in Cell Biology*, *10*(7), 274–280.

Gorris, M. (2011). *Identification and characterization of PDZD7 interacting proteins*. (Unpublished Bachelor's thesis or internship report). Radboud University Medical Centre, Nijmegen, the Netherlands.

Grati, M., Shin, J.-B., Weston, M. D., Green, J., Bhat, M. A, Gillespie, P. G., & Kachar, B. (2012). Localization of PDZD7 to the stereocilia ankle-link associates this scaffolding protein with the Usher syndrome protein network. *The Journal of Neuroscience*, *32*(41), 14288–14293.

Grondahl, J. (1987). Estimation of prognosis and prevalence of retinitis-pigmentosa and Ushers syndrome in Norway. *Clinical Genetics*, *31*(4), 255–264.

Hu, Q.-X., Dong, J.-H., Du, H.-B., Zhang, D.-L., Ren, H.-Z., Ma, M.-L., … & Sun, J.-P. (2014). Constitutive Gαi Coupling Activity of VLGR1 and its Regulation by PDZD7. *The Journal of Biological Chemistry*, *289*(35), 24215–24225.

Huet, D., Blisnick, T., Perrot, S., Bastin, P. (2014). The GTPase IFT27 is involved in both anterograde and retrograde intraflagellar transport. *eLife*, *3*(e02419), 1–25.

Ishikawa, H., & Marshall, W. F. (2011). Ciliogenesis: building the cell's antenna. *Nature Reviews. Molecular Cell Biology*, *12*, 222–234.

Jaworek, T. J., Bhatti, R., Latief, N., Khan, S. N., Riazuddin, S., & Ahmed, Z. M. (2012). USH1K, a novel locus for type I Usher syndrome, maps to chromosome 10p11.21-q21.1. *Journal of Human Genetics*, *57*(10), 633–637.

Joensuu, T., Hämäläinen, R., Yuan, B., Johnson, C., Tegelberg, S., Gasparini, P., … & Sankila, E. M. (2001). Mutations in a novel gene with transmembrane domains underlie Usher syndrome type 3. *American Journal of Human Genetics*, *69*(4), 673–684.

Keady, B. T., Samtani, R., Tobita, K., Tsuchya, M., San Agustin, J. T., Follit, J. a, … & Pazour, G. J. (2012). IFT25 links the signal-dependent movement of Hedgehog components to intraflagellar transport. *Developmental Cell*, *22*(5), 940–951.

Kersten, F. F., van Wijk, E., Hetterschijt, L., Bauβ, K., Peters, T. A, Aslanyan, M. G., … & Kremer, H. (2012). The mitotic spindle protein SPAG5/Astrin connects to the Usher protein network postmitotically. *Cilia*, *1*(1), 2.

Kimberling, W. J., Weston, M. D., Möller, C., Davenport, S. L., Shugart, Y. Y., Priluck, I. A., … & Smith, R. J. (1990). Localization of Usher syndrome type II to chromosome 1q. *Genomics*, *7*(2), 245–249.

Kremer, H., van Wijk, E., Märker, T., Wolfrum, U., & Roepman, R. (2006). Usher syndrome: molecular links of pathogenesis, proteins and pathways. *Human Molecular Genetics*, *15*(2), R262–R270.

Lee, H.-J., & Zheng, J. J. (2010). PDZ domains and their binding partners: structure, specificity, and modification. *Cell Communication and Signaling, 8*(1), 8.

Li, F.-Q., Mofunanya, A., Harris, K., & Takemaru, K.-I. (2008). Chibby cooperates with 14-3-3 to regulate beta-catenin subcellular distribution and signaling activity. *The Journal of Cell Biology*, *181*(7), 1141–1154.

Maerker, T., van Wijk, E., Overlack, N., Kersten, F. F. J., McGee, J., Goldmann, T., … & Wolfrum, U. (2008). A novel Usher protein network at the periciliary reloading point between molecular transport machineries in vertebrate photoreceptor cells. *Human Molecular Genetics*, *17*(1), 71–86.

Maher, M. T., Flozak, A. S., Hartsell, A. M., Russell, S., Beri, R., Peled, O. N., & Gottardi, C. J. (2009). Issues associated with assessing nuclear localization of N-terminally unphosphorylated beta-catenin with monoclonal antibody 8E7. *Biology Direct*, *4*, 5.

Marazita, M. L., Ploughman, L. M., Rawlings, B., Remington, E., Arnos, K. S., & Nance, W. E. (1993). Genetic epidemiological studies of early-onset deafness in the U.S. school-age population. *American Journal of Medical Genetics*, *46*(5), 486–491.

May-Simera, H. L., & Kelley, M. W. (2012). Cilia, Wnt signaling, and the cytoskeleton. *Cilia*, *1*(1), 7.

Mustapha, M., Chouery, E., Torchard-Pagnez, D., Nouaille, S., Khrais, A., Sayegh, F. N., … & Weil, D. (2002). A novel locus for Usher syndrome type I, USH1G, maps to chromosome 17q24-25. *Human Genetics*, *110*(4), 348–350.

Pieke-Dahl, S., Möller, C. G., Kelley, P. M., Astuto, L. M., Cremers, C. W., Gorin, M. B., & Kimberling, W. J. (2000). Genetic heterogeneity of Usher syndrome type II: localisation to chromosome 5q. *Journal of Medical Genetics*, *37*(4), 256–262.

Puffenberger, E. G., Jinks, R. N., Sougnez, C., Cibulskis, K., Willert, R. A., Achilly, N. P., … & Strauss, K. A. (2012). Genetic mapping and exome sequencing identify variants associated with five novel diseases. *PloS One*, *7*(1), e28936.

Rao, T. P., & Kühl, M. (2010). An updated overview on Wnt signaling pathways: a prelude for more. *Circulation Research*, 106(12), 1798–1806.

Reiners, J., Nagel-Wolfrum, K., Jürgens, K., Märker, T., & Wolfrum, U. (2006). Molecular basis of human Usher syndrome: deciphering the meshes of the Usher protein network provides insights into the pathomechanisms of the Usher disease. *Experimental Eye Research*, *83*(1), 97–119.

Riazuddin, S., Belyantseva, I. A., Giese, A. P. J., Lee, K., Indzhykulian, A. A., Nandamuri, S. P., … & Ahmed, Z. M. (2012). Alterations of the CIB2 calcium- and integrin-binding protein cause Usher syndrome type 1J and nonsyndromic deafness DFNB48. *Nature Genetics*, *44*(11), 1265–1271.

Rosenberg, T., Haim, M., Hauch, A.-M., & Parving, A. (1997). The prevalence of Usher syndrome and other retinal dystrophy-hearing impairment associations. *Clinical Genetics*, *51*(1974), 314–321.

Sadeghi, M., Kimberling, W., Tranebjœrg, L., & Möller, C. (2004). The prevalence of Usher Syndrome in Sweden: a nationwide epidemiological and clinical survey. *Audiological Medicine*, *2*(4), 220–228.

Saihan, Z., Webster, A. ., Luxon, L., & Bitner-Glindzicz, M. (2009). Update on Usher syndrome. *Current Opinion in Neurology*, *22*, 19–27.

Sankila, E. M., Pakarinen, L., Kääriäinen, H., Aittomäki, K., Karjalainen, S., Sistonen, P., & de la Chapelle, A. (1995). Assignment of an Usher syndrome type III (USH3) gene to chromosome 3q. *Human Molecular Genetics*, *4*(1), 93–98.

Schneider, E., Märker, T., Daser, A., Frey-Mahn, G., Beyer, V., Farcas, R., … & Haaf, T. (2009). Homozygous disruption of PDZD7 by reciprocal translocation in a consanguineous family: a new member of the Usher syndrome protein interactome causing congenital hearing impairment. *Human Molecular Genetics*, *18*(4), 655–666.

Sedmak, T., & Wolfrum, U. (2010). Intraflagellar transport molecules in ciliary and nonciliary cells of the retina. *The Journal of Cell Biology*, *189*(1), 171–186.

Smith, R. J., Lee, E. C., Kimberling, W. J., Daiger, S. P., Pelias, M. Z., Keats, B. J., … & Guest, M. (1992). Localization of two genes for Usher syndrome type I to chromosome 11. *Genomics*, *14*(4), 995–1002.

Spandau, U. H. M., & Rohrschneider, K. (2002). Prevalence and geographical distribution of Usher syndrome in Germany. *Graefe's Archive for Clinical and Experimental Ophthalmology = Albrecht von Graefes Archiv Für Klinische Und Experimentelle Ophthalmologie*, *240*(6), 495–498.

Takemaru, K.-I., Fischer, V., & Li, F.-Q. (2009). Fine-tuning of nuclear beta-catenin by chibby and 14-3-3. *Cell Cycle*, *8*(2), 210–213.

Takemaru, K.-I., Yamaguchi, S., Lee, Y. S., Zhang, Y., Carthew, R. W., & Moon, R. T. (2003). Chibby, a nuclear beta-catenin-associated antagonist of the Wnt/Wingless pathway. *Nature*, *422*(6934), 905–909.

Thyssen, G., Li, T.-H., Lehmann, L., Zhuo, M., Sharma, M., & Sun, Z. (2006). LZTS2 is a novel beta-catenin-interacting protein and regulates the nuclear export of beta-catenin. *Molecular and Cellular Biology*, *26*(23), 8857–8867.

Van den Hurk, J. A. J. M., Rashbass, P., Roepman, R., Davis, J., Voesenek, K. E. J., Arends, M. L., … & den Hollander, A. I. (2005). Characterization of the Crumbs homolog 2 (CRB2) gene and analysis of its role in retinitis pigmentosa and Leber congenital amaurosis. *Molecular Vision*, *11*(August 2004), 263–273.

Van Wijk, E., Kersten, F. F. J., Kartono, A., Mans, D. A., Brandwijk, K., Letteboer, S. J. F., … & Kremer, H. (2009). Usher syndrome and Leber congenital amaurosis are molecularly linked via a novel isoform of the centrosomal ninein-like protein. *Human Molecular Genetics*, *18*(1), 51–64.

Van Wijk, E., van der Zwaag, B., Peters, T., Zimmermann, U., Te Brinke, H., Kersten, F. F. J., … & Kremer, H. (2006). The DFNB31 gene product whirlin connects to the Usher protein network in the cochlea and retina by direct association with USH2A and VLGR1. *Human Molecular Genetics*, *15*(5), 751–765.

Verpy, E., Leibovici, M., Zwaenepoel, I., Liu, X. Z., Gal, A., Salem, N., … & Petit, C. (2000). A defect in harmonin, a PDZ domain-containing protein expressed in the inner ear sensory hair cells, underlies Usher syndrome type 1C. *Nature Genetics*, *26*(1), 51–55.

Wang, Y., Guo, N., & Nathans, J. (2006). The role of Frizzled3 and Frizzled6 in neural tube closure and in the planar polarity of inner-ear sensory hair cells. *The Journal of Neuroscience : The Official Journal of the Society for Neuroscience*, *26*(8), 2147–2156.

Wang, Z., Fan, Z.-C., Williamson, S. M., & Qin, H. (2009). Intraflagellar transport (IFT) protein IFT25 is a phosphoprotein component of IFT complex B and physically interacts with IFT27 in Chlamydomonas. *PloS One*, *4*(5), e5384.

Wayne, S., Der Kaloustian, V. M., Schloss, M., Polomeno, R., Scott, D. A., Hejtmancik, J. F., … & Smith, R. J. (1996). Localization of the Usher syndrome type ID gene (Ush1D) to chromosome 10. *Human Molecular Genetics, 5*(10), 1689–1692.

Weil, D., Blanchard, S., Kaplan, J., Guilford, P., Gibson, F., Walsh, J., … & Weston, M. D. (1995). Defective myosin VIIA gene responsible for Usher syndrome type 1B. *Nature*, *374*(6517), 60–61.

Weil, D., El-Amraoui, A., Masmoudi, S., Mustapha, M., Kikkawa, Y., Lainé, S., … & Petit, C. (2003). Usher syndrome type I G (USH1G) is caused by mutations in the gene encoding SANS, a protein that associates with the USH1C protein, harmonin. *Human Molecular Genetics*, *12*(5), 463–471.

Weston, M. D., Luijendijk, M. W. J., Humphrey, K. D., Möller, C., & Kimberling, W. J. (2004). Mutations in the VLGR1 gene implicate G-protein signaling in the pathogenesis of Usher syndrome type II. *American Journal of Human Genetics*, *74*(2), 357–366.

Ye, F., & Zhang, M. (2013). Structures and target recognition modes of PDZ domains: recurring themes and emerging pictures. *The Biochemical Journal, 455*(1), 1–14.

Zou, J., Zheng, T., Ren, C., Askew, C., Liu, X.-P., Pan, B., … & Yang, J. (2014). Deletion of PDZD7 disrupts the Usher syndrome type 2 protein complex in cochlear hair cells and causes hearing loss in mice. *Human Molecular Genetics*, *23*(9), 2374–2390.

On the Mechanisms of Feature Expectation and Feature-Based Attention in the Primary Visual Cortex

Lieke L. F. van Lieshout[1]
Supervisors: Peter Kok[1], Floris P. de Lange[1]

[1]*Radboud University Nijmegen, Donders Institute for Brain, Cognition and Behaviour, The Netherlands*

Both feature-based attention and feature expectation facilitate perception about the world around us. Whereas feature-based attention is known to act globally and spread across the visual field, the mechanisms of feature expectation are largely unknown. Using functional Magnetic Resonance Imaging (fMRI) and visual grating stimuli, we investigated whether the effects of feature expectation are also global, or act in a more retinotopically specific way. We did so by investigating the expectation effects in different parts of the visual cortex (V1). The Blood Oxygenation Level Dependent (BOLD) response contralateral to expected stimuli was reduced compared to unexpected stimuli. This effect did not spread across the visual field – in fact, in ipsilateral V1, the BOLD response was increased when an expected stimulus was presented compared to when an unexpected stimulus was presented. For the non-cued grating, the orientation of which was orthogonal to the expectation cue, no effects were found as a result of whether this unattended grating was congruent or incongruent with the expectation the participants had about the cued grating. These findings suggest that the mechanisms of feature expectation are retinotopically specific. Additional orientation specific BOLD analyses suggested that feature-based attention, on the other hand, spreads across the visual field. These findings would be in line with the idea of separate neuronal mechanisms for attention and expectation.

Keywords: feature expectation, feature-based attention, V1, fMRI

Corresponding author: Lieke L. F. van Lieshout; **E-mail**: l.vanlieshout@donders.ru.nl

1. Introduction

In the empirical literature, the effects of perceptual expectation tend to be conflated with those of attention (Summerfield & Egner, 2009). Also in practice, expectations and attention often coincide and interact. This might be the case because expectation and attention share some of the most basic behavioural effects: both attended and expected stimuli are detected and recognised more easily than unattended or unexpected stimuli. However, the neural effects of expectation and attention can be opposite: while attention increases the neural response to a stimulus (Kok, Rahnev, Jehee, Lau, & de Lange, 2012b; Martinez-Trujillo & Treue, 2004), expectation has been shown to decrease it (Alink, Schwiedrzik, Kohler, Singer, & Muckli, 2010; Den Ouden, Friston, Daw, McIntosh, & Stephan, 2009; Kok, Jehee, & de Lange, 2012a). Therefore, it is important to carefully distinguish between expectation and attention in experimental design and interpretation (Summerfield & Egner, 2009). The current project aims to distinguish the mechanisms of attention from those of expectation by focusing on the neuronal bases of feature-based attention and feature expectation.

1.1 The mechanisms of feature-based attention

Feature-based attention is the ability to enhance the representation of image components that are related to a particular feature (Maunsell & Treue, 2006). This means that stimuli with an attended feature have an advantage over stimuli that do not express this feature (Martinez-Trujillo & Treue, 2004; Maunsel & Treue, 2006). For example, if you are looking for your friend in a crowd and you know that your friend is wearing a red shirt, you will presumably pay attention to the colour red to find him. When doing so, all red stimuli in the visual field will have an advantage over stimuli of any other colour. This advantage is independent of the location of the stimulus in space (Melcher, Papathomas, & Vidnyánszky, 2005), meaning that the colour red will be boosted across the entire visual field. This advantage also becomes apparent when looking at the brain responses for attended versus unattended stimuli. First of all, feature-based attention has been shown to amplify the response of a particular neuron when attention is directed to the neuron's preferred feature and to suppress this response when attention is directed to the neuron's non-preferred feature (Martinez-Trujillo & Treue, 2004). In the example mentioned above, this would mean that neurons preferring the colour red will show enhanced activity and neurons that prefer a different colour will show suppressed activity. Second of all, multiple studies have shown that feature-based attention operates globally and spreads to stimuli presented outside the focus of spatial attention and to non-stimulated regions of the visual field (Jehee, Brady, & Tong, 2011; Serences & Boynton, 2007). This means that neurons tuned for an attended feature will show an enhanced response, even when no stimulus is presented in the receptive field of that neuron. This spreading of feature-based attention is unavoidable, since the attended feature is also boosted for irrelevant stimuli (Anderssen, Hillyard, & Müller, 2013) and for irrelevant parts of the visual field (Jehee et al., 2011; Serences & Boynton, 2007). In this way, feature-based attention facilitates the perception of stimuli across the entire visual field. The spreading of feature-based attention is a robust phenomenon, since it has been found through a range of different methodologies and techniques, such as fMRI (Jehee et al., 2011; Liu, Larsson, & Carrasco, 2007; Serences & Boynton, 2007), electroencephalography (EEG; Anderssen, Hillyard & Müller, 2013), single-unit recordings, (Maunsell & Treue, 2006; Treue & Martinez-Trujillo, 1999) and psychophysics (Liu & Mance, 2011).

1.2 Feature expectation

Not only feature-based attention, but also top-down expectations about the visual world facilitate perception (Bar, 2004). This facilitation becomes apparent when looking at the neuronal mechanisms of feature expectation. First of all, many studies have found that the neuronal response elicited by expected stimuli is reduced compared to the neuronal response to unexpected stimuli (Alink et al., 2010; Den Ouden et al., 2009; Kok et al., 2012a; Todorovic, van Ede, Maris & de Lange, 2011). When specifically focusing on the early visual cortex (V1), we see that perceptual expectations reduce the amplitude of the BOLD response (Alink et al., 2010; Den Ouden et al., 2009; Summerfield, Trittschuh, Monti, Mesulam, & Egner, 2008; Kok, et al., 2012a; Kok et al., 2012b), but also improve sensory representations in this region (Kok et al., 2012a). Altogether, these studies indicate that prior expectations affect sensory processing already at the earliest stages of the cortical hierarchy (Bar, 2004) by sharpening sensory representation in early visual cortex (Kok et al., 2012a). Second of all, Kok, Failing, and de Lange (2014) have recently shown

that a prior expectation of a specific visual stimulus evokes a pattern in the early visual cortex (V1) with similar feature specificity as the pattern that would be evoked by a presented stimulus. Thus, prior expectations seem to evoke stimulus templates in the early visual cortex, facilitating perception.

1.3 The current study

In summary, both feature-based attention and feature expectation facilitate perception of the world around us, but they initially seem to be two distinct phenomena. This is not only the case because they have been investigated by means of different designs and research questions, but also because their neuronal effects seem to be different. Still, Kok and colleagues (2014) mention that the evoked stimulus templates found in their study, might be similar to the templates evoked by feature-based attention. Therefore, the current study aims to investigate whether the effects of feature expectation are similar to those of feature-based attention, or whether its effects are more locally or retinotopically specific. If the first would be the case, this would mean that feature expectation operates globally and spreads to the opposite hemifield, just like feature-based attention (i.e., Serences & Boynton, 2007; Jehee et al., 2011). This finding would indicate that the mechanisms of feature-based attention and feature expectation are similar. If the latter would be the case, there would be no spreading of stimulus information due to expectation and activity elicited by expectation would only be present in the parts of the visual field that overlapped with the location at which a certain stimulus was expected. This would be an indication that feature expectation operates locally, suggesting distinct neural mechanisms for attention and expectation.

In order to investigate these two hypotheses, grating stimuli were used in which both feature-based attention and feature expectation were manipulated. The feature of interest was the orientation of the presented gratings. Feature-based attention was manipulated by using two different tasks. The first task was orientation discrimination (orientation task), in which participants had to indicate the change in orientation between two consecutive gratings. In this task, the participants were required to pay attention to the orientation of the gratings. The second task was contrast discrimination (contrast task), in which the participants had to pay attention to the contrast difference between the two. In this task, the feature 'orientation' was irrelevant. Feature expectation on the other hand, was manipulated by presenting the participants with a coloured dot before the actual gratings were shown. The colour of the dot was predictive of which grating-orientation was about to occur. In most cases (75%), the dot was followed by gratings of the expected orientation, but in some cases the dot was followed by gratings of the unexpected orientation (25%).

We investigated the expectation effects in different parts of the primary visual cortex (V1). We focussed on the BOLD response amplitude effects of expected and unexpected grating orientations in the hemisphere contralateral and ipsilateral to the attended (cued) gratings. Furthermore, we looked at the effects in the hemisphere contralateral to the unattended (non-cued) gratings as a result of whether this non-cued grating was congruent or incongruent with the expectation the participants had about the cued grating. Together these findings indicated that the effects of expectation act in a local or retinotopically specific way. On top of that, we performed some additional orientation specific analyses to look at amount of stimulus information in the hemisphere contralateral to the cued side and the hemisphere ipsilateral to the cued side. We found a spreading of stimulus information due to attention, but we found no evidence indicating that this spreading is modulated by expectation. All in all, our data gave us some indications that the mechanisms of feature expectation are local or retinotopically specific.

2. Material and methods

2.1 Participants

Thirty participants (19 female) between the ages of 19 and 29 (M = 23.1, SD = 2.7) participated in the experiment. All participants were right-handed, MRI-compatible, and had normal or corrected-to-normal vision. The study was approved by the local ethics committee (CMO region Arnhem/Nijmegen, The Netherlands) and all participants gave written informed consent, according to the declaration of Helsinki. One participant was excluded from further analyses due to excessive (>5 mm) head movements in the scanner and another, due to the absence of a clear visual signal during the retinotopic mapping session, precluding drawing of ROIs. Another five participants were excluded due to failure to perform one or both of the tasks with above chance accuracy. The final sample consisted of 23 participants (15 female) aged 19-28 years (M = 23.3, SD = 2.5), who completed both a behavioural and an fMRI session.

2.2 Experimental design and stimuli

2.2.1 Stimuli

The visual stimuli were generated using MATLAB (Mathworks, Natick, MA, USA) and the Psychophysics Toolbox (Brainard, 1997). In the behavioural session, the stimuli were presented on a BENQ XL2420T screen (1024 x 768 resolution, 60 Hz refresh rate). In the fMRI session, the stimuli were displayed on a rear-projection screen using a luminance calibrated Eiki projector (1024 x 768 resolution, 60 Hz refresh rate) against a uniform grey background. During the fMRI session, participants viewed the visual display through a mirror that was mounted on the head coil. The visual stimuli consisted of two luminance-calibrated coloured dots (orange, cyan, or grey) and two pairs of grayscale luminance-defined sinusoidal Gabor grating stimuli. The two dots were presented respectively 1° left and 1° right of the fixation bull's eye and the grating stimuli were centred at 5° of visual angle to the left and to the right of fixation (grating radius, 3.5°; spatial frequency 1.0 or 1.5 cycles/°, with randomised spatial phase). The contrast decreased linearly to zero over the outer 0.5° degrees of the gratings.

2.2.2 Experimental design

Each trial of the main experiment started with two dots appearing next to the fixation bull's eye. One of these dots was grey and the other one was either orange or cyan. They were presented for 200 ms, followed by a blank screen (550 ms). Next, two pairs of consecutive grating stimuli were presented for 500 ms each, separated by a blank screen (100 ms). The intertrial interval (ITI) was jittered between 3250 and 5250 ms. The fixation bull's eye was presented throughout the entire trial. Participants were instructed to maintain fixation on the central bull's eye during each experimental run and to attend covertly to one of two laterally presented grating stimuli. The location of the coloured dot indicated to which gratings the participants had to attend, whereas the gratings presented at the side of the grey dot had to be ignored. The actual colour of the dot (cyan/orange) predicted the orientation of the subsequent grating stimuli presented to the attended side (~45° or ~135°) with 75% validity. Which colour predicted which grating orientation was counterbalanced across participants.

The unattended (non-cued) gratings could either have the same (50%) or a different orientation (50%) from the attended (cued) gratings. In this way we made sure that the expectations about the orientation of the cued gratings were orthogonal to the orientation of the non-cued gratings.

In separate runs (128 trials, ~14 minutes), the participants performed an orientation task or a contrast task on the cued gratings. The first cued grating had an orientation of 45° or 135° and a luminance contrast of 80%. The second cued grating differed slightly from the first in terms of orientation, contrast, and spatial frequency. The same holds for the non-cued gratings of the grating pairs. When performing the orientation task, the participants had to judge whether the second cued grating was rotated clockwise or counter clockwise with respect to the first cued grating (Fig. 1). In the contrast task, the participants had to make a judgment on whether the second cued grating had a higher or lower contrast than the first cued grating. The responses had to be given by means of a button press. The direction of rotation and contrast change for the non-cued grating were independent of that of the cued grating.

Both tasks were designed to avoid a direct relationship between the perceptual expectation and the task the participants had to perform (see also Kok et al., 2012a). If the task would have been to judge the orientation of the cued grating (45° or 135°), the expectation cue would tell the participants which response was likely (75% of the trials) to be correct, making it easy for the participants to prepare a motor response. In this way, the design would make it impossible to distinguish perceptual expectation from response preparation. By using the orientation task and contrast task instead, this potential confound is avoided since these tasks are orthogonal to the actual perceptual expectation of the participants. Furthermore, these tasks allowed us to adjust the difficulty of the tasks by increasing/decreasing the difference in orientation angle or contrast. The two cued gratings and the two non-cued gratings also differed from each other in terms of phase and spatial frequency. In this way we avoided the presence of motion cues in the orientation judgment. Both gratings from the first pair had a random spatial phase on each trial and the gratings from the second grating-pair were counter phase to the first. The two gratings of each pair had spatial frequencies of 1.0 and 1.5 cycles/° and the order was pseudo-randomised and counterbalanced over conditions.

Each participant completed a total of four runs (two of each task, the order was counterbalanced

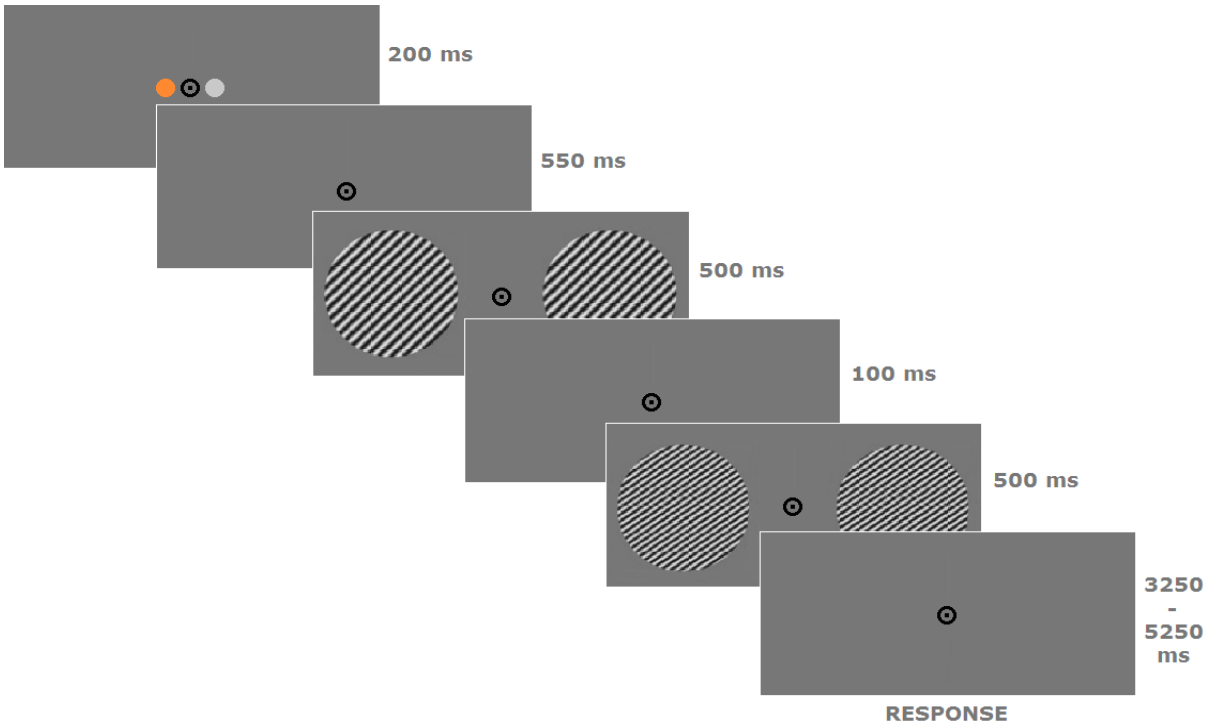

Fig. 1. On each trial, participants were presented with two consecutive grating pairs, differing from each other in terms of orientation, contrast, and spatial frequency. In both tasks, the participants are required to fixate on the fixation bull's eye and to covertly attend to the gratings presented at the side of the coloured dot (in this example, the left side is the attended/cued side). In separate blocks, the participants performed either an orientation task ("Was the second cued grating turned clockwise or counterclockwise with respect to the first cued grating?") or a contrast task ("Was the second cued grating of higher or lower contrast than the first cued grating?"). The color of the dot predicted (with 75% validity) the overall orientation of the cued gratings (~45° or ~135°).

over participants) of the experiment, yielding a total of 512 trials. Each run consisted of two blocks of 64 trials, separated by a 30 s break during which the screen was blank. For each participant, the orientation and contrast differences between the two cued gratings were determined by an adaptive staircase procedure (Watson & Pelli, 1983) separately for the orientation and the contrast task. This was done to yield a comparable task difficulty and performance (~75% correct) for both tasks. The staircase values were determined during the behavioural session and checked during a short practice block in the MRI-scanner. For the four experimental runs of the fMRI session, the orientation difference and contrast difference were set as fixed values.

Subsequent to the main experiment, subjects performed a functional localiser task. During this task, a fixation bull's eye was presented, surrounded by full-field flickering gratings. These gratings were presented at 100% contrast in blocks of ~15 s. The gratings were flickering on and off at a frequency of 2 Hz. Each block contained gratings with a fixed orientation of 45° or 135° and random spatial phase and spatial frequency (1.0 or 1.5 cycles/°). The participants were presented with four blocks in which the two orientations were presented consecutively (the order was pseudo-randomised), followed by a ~15 s blank screen with just a fixation point. This was repeated 8 times and lasted ~10 min. At fixation, a stream of green letters was presented. The participants had to press a button when they detected either an 'X' or a 'Z' in this letter stream. This task was meant to ensure fixation and to avoid eye movements to the flickering gratings.

After this task, the participants completed 2 to 4 runs of a population receptive field (pRF) mapping task (Dumoulin & Wandell, 2008). In this task, a fixation point was presented in the middle of the screen. Around this fixation point, bars containing flickering checkerboards (2 Hz) moved across the screen in a circular aperture with a diameter of 20°. The bars moved in eight different directions (two horizontal, two vertical, and four cardinal) in 20 steps of 1°. Four blank screens were inserted after each block of cardinally moving bars. The participants were instructed to fixate on the fixation point, which alternated between red and green, and to press a button when this fixation point changed colour. The aim of the pRF mapping task was to determine the population receptive field for each voxel in the visual cortex.

2.2.3 Behavioural session

A few (~1-4) days before the fMRI session of the experiment, the participants completed a behavioural session. The aim of this session was to familiarize the subjects with the tasks and the colour-grating associations and to determine the staircase values for both tasks at which the participants performed about 75% correct.

In order to make the participants familiar with the colour-grating associations, they started with an orientation identification task. In this task, the participants had to fixate on the fixation bull's eye that was presented in the middle of the screen. Next to the fixation point, two dots appeared: a grey dot and a coloured dot (orange or cyan, presented for 200 ms), followed by a blank screen (550 ms) and a pair of grating stimuli (500 ms). The side of the coloured dot indicated the side to which the participants had to attend to (the cued side) and the actual colour of the dot predicted the orientation of the subsequent grating stimulus presented to the cued side (~45° or ~135°) with 75% validity. The participants had to indicate whether the grating that was presented at the cued side had an orientation of 45° or an orientation of 135° by means of a button press. The orientation of the non-cued grating was either the same (50%) or different (50%) from that of the cued grating. In this way, the expectation about the orientation of the cued grating was never about the non-cued grating. The participants had to complete 3 blocks of 128 trials (lasting ~20 min in total). This task was used during the behavioural session only and ensured that the participants learned the colour-grating associations correctly.

After these blocks of the orientation identification task, the participants were presented with the instructions of the orientation task and the contrast task. Next, they completed a few practice trials in which they received feedback on their performance, followed by one practice block of both tasks in which they did not receive any feedback. After these practice blocks, the main experiment started (lasting ~40 min in total), consisting of four blocks of 128 trials of each task (the order was counterbalanced across participants). During these blocks, the orientation and contrast differences were determined by an adaptive staircase procedure (Watson & Pelli, 1983). This was done separately for the orientation and the contrast task and the aim was to determine the orientation and contrast difference for which participants were about 75% correct, allowing us to keep performance and task difficulty equal for both tasks.

2.3 fMRI Acquisition Parameters

Functional images were acquired using full-brain 3D echo-planar imaging (TR = 47 ms, TE= 25 ms, 64 transversal slices with a distance of 50%, voxel size of 2 x 2 x 2 mm, FoV read of 256 and FoV phase of 100%, GRAPPA acceleration factor 2, 15° flip angle). Anatomical images were acquired using a T1-weigted MP-RAGE sequence, using a GRAPPA acceleration factor of 2 (TR = 2300 ms, TE = 3.03 ms, voxel size 1 x 1 x 1 mm, 192 transversal slices, 8° flip angle).

2.4 fMRI Data Preprocessing

The images were preprocessed using SPM8 (www.fil.ion.ucl.ac.uk/spm, Wellcome Trust Centre for Neuroimaging, London, UK). The first four volumes of each run were discarded to allow T1 equilibration. The functional images were spatially realigned to the mean image. The head movement parameters were used as nuisance regressors in the general linear model. For each participant, the functional volumes were cropped by removing a total of 8 slices at the top and bottom of the images and 10 slices from both the left and right side of the images to reduce storage load. Next, the structural image was coregistered with the cropped mean functional volume.

For the whole brain analysis, some additional preprocessing steps were performed. The T1 anatomical images were normalised to a T1 template based on the Montreal Neurological Institute (MNI) reference brain and the resulting parameters were applied to the functional resliced volumes. Normalised images were spatially smoothed with an 8-mm FWHM isotropic Gaussian Kernel and high-pass filtered with a cutoff of 1/128 Hz.

2.5 Data analyses

2.5.1 Behavioural analyses

The behavioural analyses were performed using MATLAB (Mathworks, Natick, MA, USA). We analysed reaction times and accuracy in task performance. First of all, we checked whether the participants learned the colour-grating associations correctly during the orientation identification task that was part of the behavioural session. We did so by looking at the differences in accuracy and reaction times between expected and unexpected

grating orientations using paired t-tests. Next, we checked whether participants performed accurately during the fMRI session on both the orientation task and the contrast task (~75% correct) and whether there were differences in accuracy and reaction times between the two tasks. This was also done by means of paired t-tests. Furthermore, we looked at whether there was a difference in performance and reaction times between expected and unexpected trials for both tasks by means of paired t-tests.

2.5.2 Whole brain analyses

The whole brain analysis was performed using SPM8 (www.fil.ion.ucl.ac.uk/spm, Wellcome Trust Centre for Neuroimaging, London, UK). We modelled the data of each subject using an event-related approach, within the framework of the GLM. Regressors representing the different conditions (two different tasks, two cued locations, two orientations of gratings presented at the cued side [expected/unexpected] and two possible orientations [congruent/incongruent with expectation] of the gratings presented at the non-cued side) were constructed by convolving the onset of the first grating pair in each trial with a canonical haemodynamic response function (HRF) and its temporal derivative (Friston et al., 1998). Instruction and break screens were included as regressors of no interest, as well as head motion parameters (Lund, Norgaard, Rostrup, Rowe, & Paulson, 2005).

2.5.3 pRF estimation and retinotopic mapping

We used the data from the pRF mapping task (the moving bar runs) to estimate the population receptive field (pRF) of each voxel in the functional volumes. By means of this method, we are able to estimate the coordinates of the receptive field centre, as well as the size of the receptive field of each voxel in degrees of visual angle.

MrVista (http://white.stanford.edu/software/) was used to perform the model-based pRF analysis, in which a predicted BOLD signal is calculated from the known stimulus parameters and a model of the underlying neuronal population. The model of the neuronal population consisted of a two-dimensional Gaussian pRF, with parameters x0, y0, and σ. The coordinates of the centre of the receptive field are given by x0 and y0, and σ indicates the spread (standard deviation) or size of the receptive field. All parameters were stimulus-referred and their units were degrees of visual angle. These parameters were used to obtain the best possible fit of the predicted to actual BOLD signal (see also Dumoulin & Wandell, 2008).

Once estimated, x0 and y0 were converted to eccentricity and polar-angle measures, which were then used for the retinotopic mapping. Polar-angle maps were overlayed on inflated cortical surfaces using Freesurfer (http://surfer.nmr.mgh.harvard.edu/) to identify the boundaries of retinotopic areas in early visual cortex (Engel, Glover, & Wandell, 1997; Sereno et al., 1995). In this way we identified areas V1, V2, and V3 for the left and right hemisphere separately.

2.5.4 BOLD amplitude analyses of retinotopic areas

For the amplitude analyses, we selected voxels based on their t-values for the contrast attention left versus attention right. We selected the 50 voxels most active when attention was directed to the left side of the visual field and the 50 voxels most active when attention was directed to the right side of the visual field.

Again, data of each subject were modelled using an event-related approach within the framework of the GLM. The same regressors as described for the whole brain analysis were used. The regressors were constructed by convolving the onset of the first grating pair in each trial with a canonical haemodynamic response function (HRF; Friston et al., 1998). Instruction and break screens were included as regressors of no interest, as well as head motion parameters (Lund et al., 2005).

For the analyses, we performed a two-way repeated-measures ANOVA with the factors "Expected/Unexpected grating orientation", and "Orientation task/Contrast task" on the amplitudes of the BOLD responses in the hemisphere contralateral to the cued gratings. We did the same for the hemisphere ipsilateral to the cued gratings. Additionally, we performed a three-way repeated-measures ANOVA with the factors "Hemisphere contralateral/ipsilateral," "Expected/Unexpected grating orientation," and "Orientation task/Contrast task." Next, we performed a two-way repeated-measures ANOVA with the factors "Grating orientation congruent/incongruent with expectation" and "Orientation task/Contrast task" on the amplitudes of the BOLD responses in the hemisphere contralateral to the non-cued gratings.

Additionally, we did a three-way repeated-measures ANOVA with the factors "Hemisphere contralateral to cued/non-cued grating," "Grating orientation congruent/incongruent with expectation," and "Orientation task/Contrast task."

2.5.5 Orientation specific analyses of retinotopic areas

For the orientation specific analyses, we selected the 100 voxels most active when attention was directed to the left side of the visual field and the 100 voxels most active when attention was directed to the right side of the visual field. For both attended sides, we selected 25 voxels that showed the strongest response to gratings of 45° and 25 voxels that showed the strongest response to gratings of 135°. These voxels were selected based on their t-values for the contrast 45° versus 135° obtained during the functional localiser.

Also for these analyses, data of each subject were modelled using an event-related approach within the framework of the GLM. Regressors represent the different conditions (two different tasks, two cued locations, two orientations of gratings presented at the cued side [expected/unexpected], two possible orientations [congruent/incongruent with expectation] of the gratings presented at the non-cued side, and two possible [45° or 135°] expected orientations). The regressors were constructed by convolving the onset of the first grating pair in each trial with a canonical haemodynamic response function (HRF; Friston et al., 1998). Instruction and break screens were included as regressors of no interest, as well as head motion parameters (Lund et al., 2005). A similar model was constructed for the data of the localiser run, with two separate regressors for the two grating orientations (45° or 135°).

For the analyses, we performed a two-way repeated-measures ANOVA with the factors "Expected/Unexpected grating orientation" and "Preferred/Non-preferred Orientation" on the BOLD response amplitudes in the hemisphere contralateral to the cued gratings. To check for differences between the orientation task and the contrast task, we additionally performed a three-way repeated-measures ANOVA with the factors "Expected/Unexpected grating orientation," "Preferred/Non-preferred orientation," and "Orientation task/Contrast task." We performed the same analyses on the BOLD response amplitudes in the hemisphere ipsilateral to the cued gratings.

3. Results

3.1 Behavioural results

3.1.1 Behavioural session

The data from the orientation identification task the participants performed during the behavioural session showed that participants were more accurate and faster for expected gratings (mean accuracy [$M_{accuracy}$] = 89%, SD = 11%; mean reaction time [M_{RT}] = 451 ms, SD = 92 ms) than for unexpected gratings (M = 84%, SD = 15%; M_{RT} = 464 ms, SD = 99.7 ms), $t_{accuracy}(22) = 3.54$, $p = .002$; $t_{RT}(22) = -2.46$, $p = .022$. These differences suggest that the participants learned the colour-grating associations correctly.

3.1.2 fMRI session

The behavioural data from the orientation task and the contrast task obtained during the fMRI session indicated that the participants were able to discriminate small differences in orientation (4.0° with 83% accuracy) and contrast (8% with 78% accuracy) of the cued gratings. The accuracy for the orientation task was significantly higher than the accuracy for the contrast task, $t(22) = 2.18$, $p = .040$, but there was no difference in reaction time between the tasks (M_{RT} = 702 ms, SD = 112 ms, vs. M_{RT} = 712 ms, SD = 157 ms, respectively), $t(22) = -0.47$, $p = .642$.

Task performance and reaction times were not influenced by whether the cued grating had the expected or the unexpected orientation. This was the case for both the orientation task ($M_{accuracy}$ = 83%, SD = 7% vs. $M_{accuracy}$ = 84%, SD = 8%, $t(22) = -0.42$, $p = .678$; M_{RT} = 702 ms, SD = 111 ms vs. M_{RT} = 701 ms, SD = 116 ms, $t(22) = 0.28$, $p = .781$) as well as the contrast task ($M_{accuracy}$ = 78%, SD = 10% vs. $M_{accuracy}$ = 77%, SD = 9%, $t(22) = 0.47$, $p = .645$; M_{RT} = 711 ms, SD = 157 ms, vs. M_{RT} = 715 ms, SD = 158 ms, $t(22) = 0.73$, $p = .473$).

3.2 Whole brain results

We performed a whole brain analysis to investigate any differential brain activity due to directing attention to different sides of the visual field. As expected, we found increased neural activation in the right visual cortex when participants paid attention to the left side of the visual field, and in the left visual cortex when participants directed

Table 1. Localisation of brain activations

Anatomical region	Hemisphere	t-value	Cluster size	Corrected p-value	Coordinates (x y z)		
Attention left > attention right							
Occipital lobe	Right	8.32	64	.000	16	-96	20
Occipital lobe	Right	9.89	52	.000	20	-78	-10
Occipital lobe	Right	8.69	13	.000	30	-88	6
Occipital lobe	Right	8.57	5	.000	36	-84	-4
Attention right > attention left							
Occipital lobe	Left	7.72	3	.001	-22	-100	14
Occipital lobe	Left	7.48	2	.003	-18	-102	16

Note. Spatial coordinates of local maxima of regions showing effects for attention left vs. attention right and attention right vs. attention left. Coordinates correspond to the standard Montreal Neurological Institute (MNI) brain. All results are cluster-level corrected for multiple comparisons (FWE). Only results with cluster size > 1 are reported in this table.

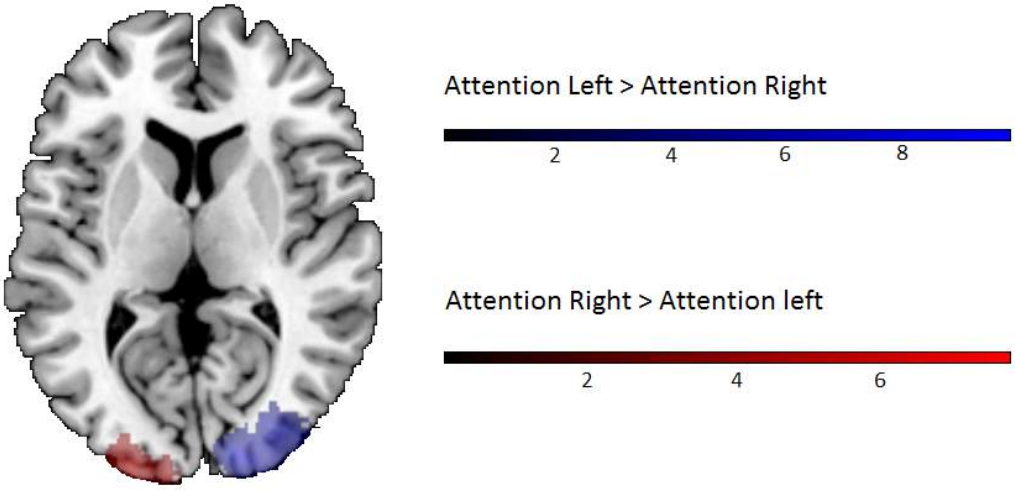

Fig. 2. Directing attention to the left side of the visual field activates the right visual hemisphere, whereas directing attention to the right side of the visual field activates the left visual hemisphere. For visualisation, p-values of .001 (uncorrected) are used in this figure. The color bars indicate t-values.

their attention towards the right side of the visual field (Table 1).

All in all, the whole brain results show that directing attention towards a particular side of the visual field activates the contralateral visual cortex, as one would expect (Fig. 2). These findings, together with the behavioural results, indicate that the participants covertly attended to the correct grating stimuli and performed the tasks on the correct grating pairs.

3.3 ROI amplitude results

3.3.1 Expectation effects for attended gratings

Since the whole brain results indicated robust attention effects in the hemisphere contralateral to the cued side, we first of all took a closer look at the effects of expectation in the primary visual cortex of this hemisphere (V1). We found that expected grating orientations elicited a lower BOLD response amplitude in the contralateral hemisphere than unexpected grating orientations, $F(1,22) = 37.08$, $p = .000$. There was no main effect of task, $F(1,22) = 0.15$, $p = .862$, and also the interaction between expectation and task was not significant, $F(1,22) = 0.32$, $p = .580$. Thus, expected grating orientations elicited a lower BOLD response than unexpected grating orientations, regardless of which task was performed (Fig. 3). This finding is consistent with predictive coding accounts, saying that perceptual expectations reduce the BOLD response amplitude in early visual cortex (Den Ouden et al., 2009; Kok et al., 2012a; Kok et al., 2012b; Summerfield et al., 2008).

Next, we investigated whether this expectation

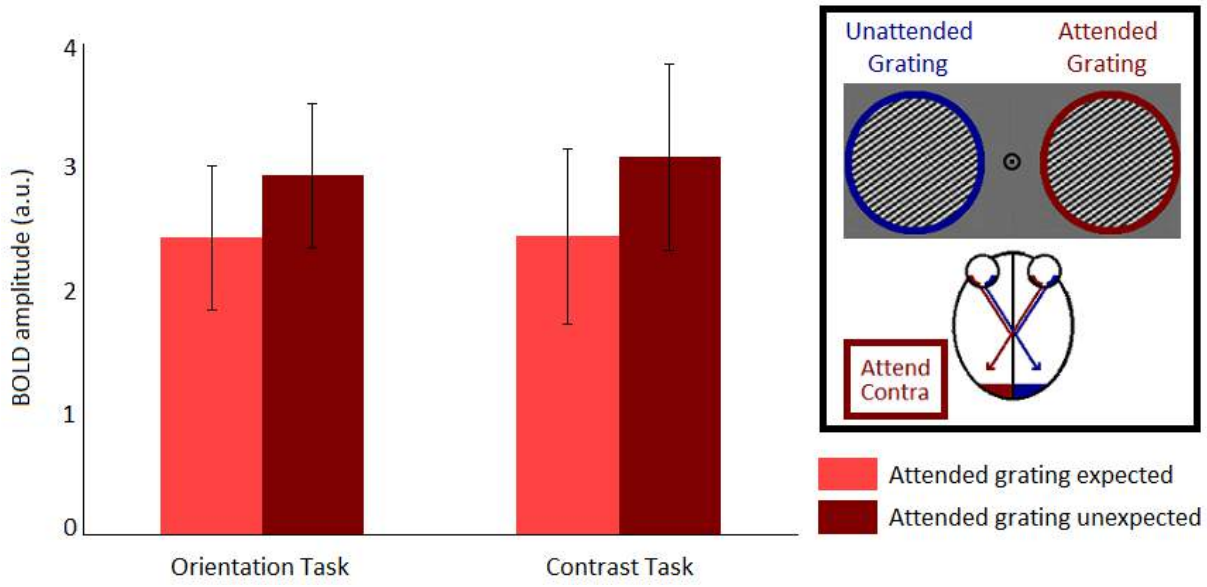

Fig. 3. Perceptual expectations reduce the neuronal BOLD response amplitudes in the early visual hemisphere (V1) contralateral to the attended (cued) gratings. This effect is independent of the task the participants performed. Error bars indicate SEM.

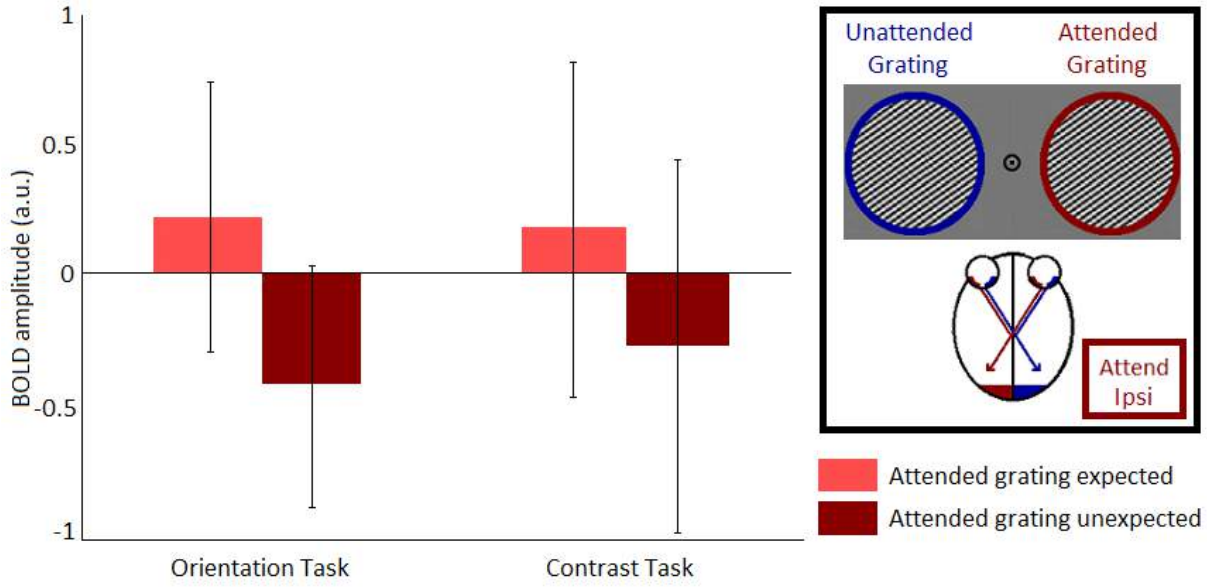

Fig. 4. Expectation elicits enhanced neuronal BOLD response amplitudes in the early visual hemisphere (V1) ipsilateral to the attended (cued) gratings. This effect is independent of the task the participants performed. Error bars indicate SEM.

effect operates globally by looking at whether this effect spreads to the ipsilateral hemisphere. Importantly, voxels in the ipsilateral hemisphere are not directly activated by the grating to which the expectation cue pertains. Still, if expectation would operate globally and spread to the opposite hemifield, one might also expect to see a reduction of the BOLD response as a result of expected versus unexpected grating orientations in the ipsilateral hemisphere. Surprisingly, we found that the effects of expectation were reversed in the ipsilateral hemisphere. In other words, expected grating orientations elicited a higher BOLD response than unexpected grating orientations in the hemisphere ipsilateral to these gratings, $F(1,22) = 14.51$, $p = .000$. Again, there was no main effect of task, $F(1,22) = 0.01$, $p = .915$, and also the interaction between expectation and task was not significant, $F(1,22) = 0.44$, $p = .515$, indicating that this pattern of results was independent of the task participants performed (Fig. 4).

To confirm that the expectation effects differed between the contralateral (Fig. 3) and ipsilateral hemispheres (Fig. 4), we performed an

additional three-way repeated-measures ANOVA (see Methods). We found a significant interaction between hemisphere and expectation, $F(1,22) = 48.70$, $p < .001$, suggesting that the effects of expectation indeed differed between the contralateral and ipsilateral hemisphere. Together, these findings suggest that a reduced BOLD response amplitude due to perceptual expectations only occurs in the hemisphere in which the expected grating enters our visual cortex (the contralateral hemisphere; Fig. 3). However, in the opposite hemisphere (the ipsilateral hemisphere; Fig. 4), perceptual expectations evoked an enhanced BOLD response. This effect could be explained by an allocation of resources (Lavie, 2005; Lavie, Hirst, de Fockert, & Viding, 2004). For unexpected gratings, all processing capacity might be needed in the contralateral hemisphere, drawing away resources from the ipsilateral hemisphere.

3.3.2 No congruency effects for unattended gratings

As described in the previous paragraph, we found clear expectation effects for the gratings to which the expectation cue pertained. In our design, the expectation about the upcoming grating orientations was always about the attended gratings only and the orientations of the unattended gratings were always independent of the expectation cue. Still, if perceptual expectations would operate globally, one could argue that the expectation about the upcoming grating orientation would pertain to the entire visual field and not only to the cued location. If this would be the case, perceptual expectations might also effect the processing of non-cued stimuli, whose features are in fact orthogonal to the expectation cue. This would result in a reduction of the BOLD response amplitude in the hemisphere contralateral to the non-cued grating as a result of whether this grating was congruent or incongruent with the expectation the participants had about the cued grating. The pattern of results would then be similar to that of the hemisphere contralateral to the cued gratings (Fig. 3).

However, we found no main effects of congruency, $F(1,22) = 0.56$, $p = .462$, and task, $F(1,22) = 0.01$, $p = .915$ for the non-cued gratings. Also the interaction between these two factors was not significant, $F(1,22) = 0.64$, $p = .433$. These findings indicate that the BOLD response amplitude in the primary visual cortex (V1) of the hemisphere contralateral to the non-cued grating was not modulated by whether the orientation of this grating was congruent or incongruent with the expectation the participants had about the cued grating (Fig. 5).

Also for these findings, we checked whether there were differences between the BOLD response amplitudes in the hemisphere contralateral to the cued gratings (Fig. 3) and the hemisphere contralateral to the non-cued gratings (Fig. 5). We found that expected/congruent grating orientations overall elicited a lower BOLD response than unexpected/incongruent gratings, $F(1,22) = 9.46$, $p = .006$, but we also found a significant interaction between hemisphere and expectation, $F(1,22) = 11.89$, $p = .002$. Together these findings indicate that

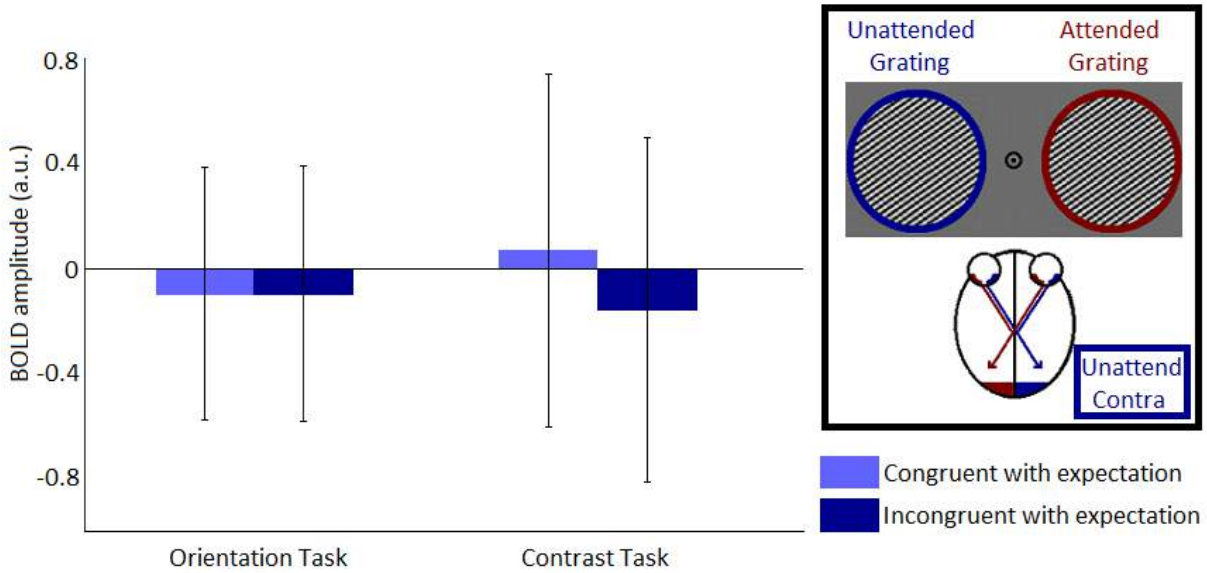

Fig. 5. There were no effects of whether the unattended (non-cued) grating was congruent or incongruent with the expectation the participants had about the attended (cued) gratings in the early visual hemisphere (V1) contralateral to the unattended (non-cued) gratings. Error bars indicate SEM.

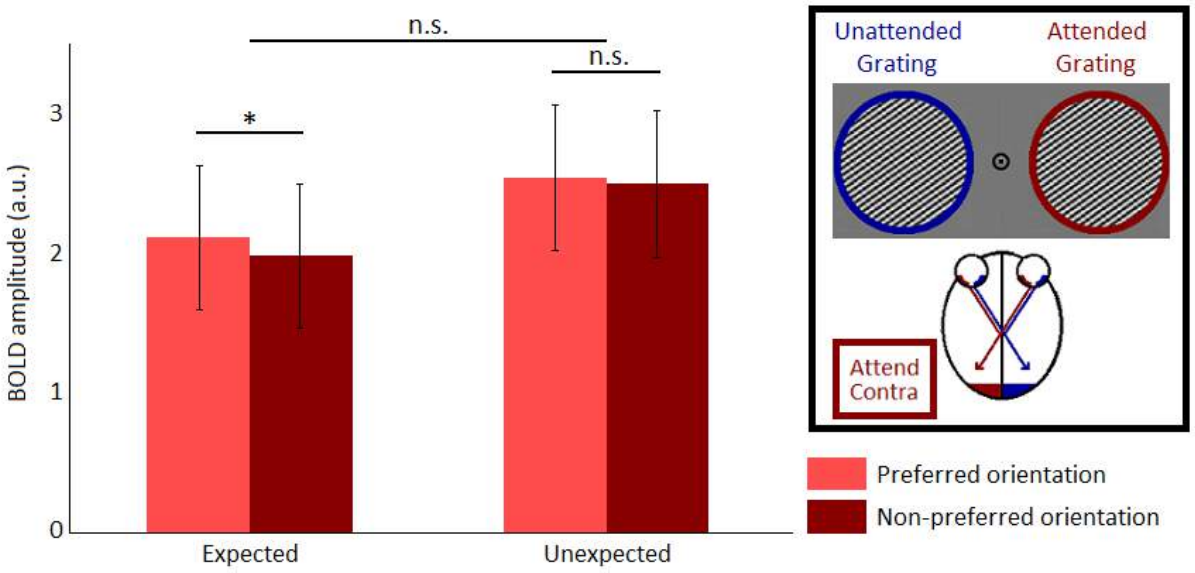

Fig. 6. Perceptual expectations reduce the neuronal BOLD response amplitudes in the early visual hemisphere (V1) contralateral to the attended (cued) gratings. There was no evidence of a higher BOLD response for preferred compared to non-preferred grating orientations and we found no concrete evidence of more stimulus information for expected compared to unexpected gratings. These effects are independent of the task participants performed. Error bars indicate SEM. *p < .05.

the reduced BOLD response amplitude effects for the expectation about the cued gratings are clearly visible in the hemisphere contralateral to the cued gratings (Fig. 3), but are absent in the hemisphere contralateral to the non-cued gratings (Fig. 5). This is an indication that feature expectation operates locally and has no effect on stimuli that are independent of the expectation.

3.4 ROI orientation specific results

The ROI amplitude results described in the previous paragraph, gave some indications about the spatial specificity of the expectation effects. To investigate the spreading of feature-based attention and feature expectation across the visual field, we additionally looked at the orientation specific BOLD response in the hemisphere contralateral to the cued gratings and the hemisphere ipsilateral to the cued gratings. We estimated the BOLD responses evoked in the selected voxels preferring 45° and 135° separately on the basis of an independent localiser data set (see Methods). In this way, we were able to probe the representational content of the BOLD signal.

3.4.1 Orientation specific results in the contralateral hemisphere

First of all, we looked at the orientation specific effects in the hemisphere contralateral to the cued grating. As described in the previous section, we found that perceptual expectation reduces the neural response amplitude in this hemisphere (Fig. 3). In line with the findings by Kok and colleagues (2012a), we would also expect that expected gratings contain more stimulus information than unexpected gratings (also called the 'sharpening effect'). If this would be the case in the current study, this would be reflected in a significant interaction effect between orientation preference and expectation.

However, our data showed no significant effect for orientation preference, $F(1,22) = 2.80$, $p = .109$, and no significant interaction between expectation and orientation preference, $F(1,22) = 0.83$, $p = .372$. These findings indicate that there was no significant sharpening effect of expectation in the hemisphere contralateral to the cued gratings as we would expect (Fig. 6). Post-hoc t-tests revealed that preferred grating orientations elicit a higher BOLD response than non-preferred grating orientations for the expected gratings, $t(22) = 2.25$, $p = .035$, but not for unexpected gratings, $t(22) = 0.57$, $p = .572$. These results would be in line with the sharpening effect (Kok et al., 2012a), but because of the absence of an interaction between expectation and orientation preference we have no concrete evidence for this effect.

On top of this, we found no significant interactions with task ($p > .10$ for all interactions), indicating that the effects were consistent for both tasks.

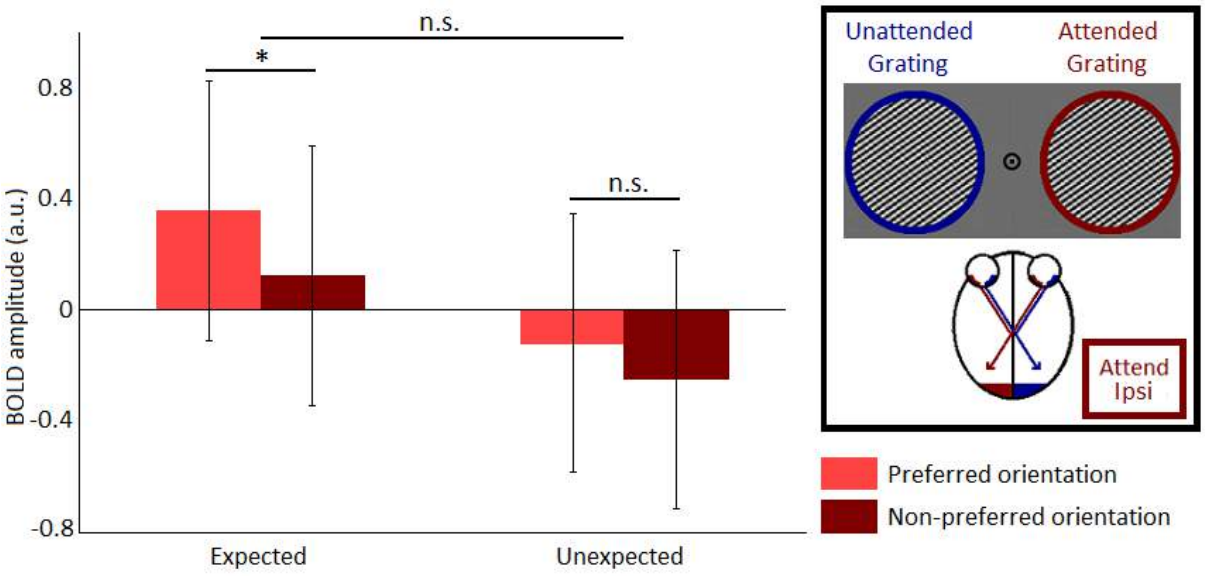

Fig. 7. Expectation elicits higher neuronal BOLD response amplitudes in the early visual hemisphere (V1) ipsilateral to the attended (cued) gratings. Also preferred grating orientations elicit a higher BOLD response than non-preferred grating orientations, indicating a spreading of attention. The latter effect is independent of the expectation the participants had about the upcoming grating orientation and of the task the participants performed. Error bars indicate SEM. *p < .05.

3.4.2 Orientation specific results in the ipsilateral hemisphere

To look at the spreading of stimulus information due to attention, we investigated whether there would be more stimulus information about the preferred grating orientations compared to the non-preferred grating orientations in the hemisphere ipsilateral to the cued gratings. Indeed we found that the BOLD-response amplitude for the preferred grating orientations was higher than for the non-preferred grating orientations, $F(1,22) = 12.44$, $p = .002$, indicating a spreading of attention to the ipsilateral hemisphere. However, there was no significant interaction between expectation and orientation preference, $F(1,22) = 1.64$, $p = .213$, suggesting that the orientation-effects are similar for both expected and unexpected gratings (Fig. 7). However, post-hoc t-tests revealed that preferred grating orientations elicit a higher BOLD response than non-preferred grating orientations for expected gratings, $t(22) = 3.58$, $p = .002$, but not for unexpected gratings, $t(22) = 1.60$, $p = .124$. Because of the absence of an interaction between expectation and orientation preference, there is no concrete evidence that there is more spreading for expected than for unexpected grating orientations. Thus, there seems to be spreading due to attention, but we found no evidence for more stimulus information for either expected or unexpected gratings in the ipsilateral hemisphere. None of these effects interacted with task ($p > .10$ for all interactions), indicating that these findings were consistent for both tasks.

4. Discussion

Both feature expectation and feature-based attention facilitate perception of the world around us. Whereas feature-based attention is known to operate globally and to spread across the visual field (e.g., Jehee et al., 2011; Serences et al., 2007), the mechanisms of feature expectation are largely unknown. Using fMRI, we attempted to find out whether feature expectation operates globally, or whether its mechanisms are more locally or retinotopically specific. Our results suggest that feature expectation can have spatially specific effects on the amplitude of the neural response in V1. The results from the orientation specific analyses suggest that feature-based attention, on the other hand, spreads across the visual field.

4.1 BOLD response amplitude results indicate local effects for expectation

The BOLD response amplitude results revealed that expected grating orientations elicit lower BOLD response amplitudes than unexpected grating orientations in the hemisphere contralateral to the cued gratings. This finding is in line with predictive

coding accounts, saying that expectations reduce BOLD response amplitudes in the early visual cortex (Den Ouden et al., 2009; Kok et al., 2012a; Kok et al., 2012b; Summerfield et al., 2008). If feature expectation would operate globally, we would expect this effect to spread across the visual field and therefore also be present in the hemisphere ipsilateral to the cued gratings. However, we found that the effects in this hemisphere were reversed: expected grating orientations elicited a higher BOLD response amplitude than unexpected grating orientations. These reversed effects in the ipsilateral hemisphere could be explained by the idea of allocation of resources (Lavie, 2005; Lavie et al., 2004). Consistent with predictive coding accounts, unexpected grating orientations might require more processing capacity than expected grating orientations. In the current design, this processing capacity might only be needed in the hemisphere where the grating enters our visual cortex (the hemisphere contralateral to the cued gratings). Therefore, the resources needed for this processing, might be drawn away from the ipsilateral hemisphere, resulting in the reversed pattern found in this hemisphere. These results suggest that expectation has an effect on the BOLD response amplitudes in the ipsilateral hemisphere. However, the reversed pattern seems to indicate that these effects are not caused by a global spreading of expectation across the visual field, but rather by an allocation of resources.

Furthermore, if feature expectation would operate globally, we would expect that the expectation about the upcoming grating orientations would be about the entire visual field and not only about the cued location. However, we found no effects in the hemisphere contralateral to the non-cued gratings as a result of whether these gratings were either congruent or incongruent with expectation. Thus, expectation effects for the cued gratings are clearly visible in the hemisphere contralateral to these cued gratings, but are absent in the hemisphere contralateral to the non-cued gratings. This is an indication that feature expectation operates locally and does not spread across the visual field, unlike the global mechanisms of feature-based attention (Jehee et al., 2011; Serences et al., 2007).

4.2 Orientation specific analyses indicate a spreading of feature-based attention

Additionally, we investigated orientation specific BOLD signals both contralateral and ipsilateral to the cued gratings. Surprisingly, we found no significant orientation specific effects in the hemisphere contralateral to the cued gratings when collapsing over expected and unexpected gratings. However, looking at expected and unexpected grating orientations separately, we found that preferred grating orientations elicit significantly higher BOLD response amplitudes than non-preferred grating orientations for the expected gratings, but not for the unexpected gratings. However, there was no significant interaction between orientation preference and expectation. In other words, we found no concrete evidence that expected grating stimuli contain more stimulus information than unexpected grating stimuli, unlike the findings by Kok and colleagues (2012a).

On the other hand, we found that preferred grating orientations elicit a higher BOLD response amplitude than non-preferred grating orientations in the hemisphere ipsilateral to the cued gratings. This finding suggests a spreading across the visual field due to attention, consistent with previous findings by Serences and colleagues (2007) and Jehee and colleagues (2011). When looking at expected and unexpected orientations separately, we found that for expected gratings, preferred orientations elicited higher BOLD response amplitudes than non-preferred orientations. This effect was not significantly present for unexpected grating stimuli. However, the lack of a significant interaction between orientation preference and expectation precludes the claim that expected stimuli contain more stimulus information than unexpected stimuli in the ipsilateral hemisphere. Thus, we find no evidence for differential spreading for expected and unexpected grating orientations.

4.3 Future directions

All in all, the BOLD response amplitude results described in the previous section seem to indicate that the effects of feature-expectation act in a retinotopically specific way. For the orientation specific results, the conclusions remain a little elusive. Presumably, the orientation specific analyses performed in the current study are not sensitive enough to investigate the effects of feature expectation. Splitting the voxels based on their orientation preference may not be the most sensitive way of looking at orientation specific signals. A more elegant and sensitive way is to do this by means of support vector machines (SVM). Using this method, a linear discriminant function can be obtained, which is able to distinguish between the two orientations

(45° or 135°). Therefore, a next step would be to study the orientation specific signals by means of these support vector machines.

Furthermore, we could take a closer look at the null-effects of expectation on the orientation specific signal found in the current study. There are two possible explanations for these null-effects: either the null hypothesis is true, or the measure we used is too noisy to distinguish between the null and alternative hypotheses. Bayesian statistics could be used to distinguish between these two explanations.

4.4 Limitations

Surprisingly, we did not find any differences in the orientation specific results between both tasks. In the orientation task, the participants were paying attention to the feature 'orientation,' whereas this feature was irrelevant in the contrast task. Therefore, we would have expected that there would only be spreading of orientation information due to attention for the orientation task, but not for the contrast task (consistent with Jehee et al., 2011). However, our results showed no such interaction with task. A reason for this finding might be that the contrast task seemed to be more difficult than the orientation task. This is reflected in the finding that task performance for the contrast task was significantly lower than the performance for the orientation task. These differences in task difficulty make it hard to directly compare the effects of both tasks. Potentially, the participants needed more attention or cognitive effort to successfully complete the contrast task than to complete the orientation task, causing these null effects.

5. Conclusion

All in all, the results found in the current study give us some hints about the local or retinotopically specific effects of expectation, contrasting with the global nature of feature-based attention. Local effects of expectation were mainly found by means of the BOLD amplitude analyses, whereas the orientation specific analyses revealed a spreading due to attention. However, these results should be interpreted with caution. It might be promising to use more sensitive methods to take a closer look at the orientation specific information for expected and unexpected gratings in different parts of the primary visual cortex (V1), enabling us to distinguish the mechanisms of feature expectation from those of feature-based attention.

References

Alink, A., Schwiedrzik, C. M., Kohler, A., Singer, W., & Muckli, L. (2010). Stimulus predict- ability reduces responses in primary visual cortex. *Journal of Neuroscience*, *30*(8), 2960–2966.

Anderssen, S. K., Hillyard, S. A., & Muller, M. M. (2008). Attention facilitates multiple stimulus features in parallel in human visual cortex. *Current Biology*, *18*(13), 1006–1009.

Bar, M. (2004). Visual objects in context. *Nature Reviews Neuroscience*, *5*, 617–629.

Brainard, D. H. (1997). The Psychophysics Toolbox. *Spatial Vision*, *10*, 433–436.

Den Ouden, H. E. M., Friston, K. J., Daw, N. D., McIntosh, A. R., & Stephan, K. E. (2009). A dual role for prediction error in associative learning. *Cerebral Cortex*, *19*(5), 1175–1185.

Dumoulin, S. O., & Wandell, B. A. (2008). Population receptive field estimates in human visual cortex. *Neuroimage*, *39*(2), 647–660.

Engel, S. A., Glover, G. H., & Wandell, B. A. (1997). Retinotopic organization in human visual cortex and the spatial precision of functional MRI. *Cerebral Cortex*, *7*, 181–192.

Friston, K. J., Fletcher, P., Josephs, O. Holmes, A., Rugg, M. D., & Turner, R. (1998). Event-related fMRI: characterizing differential responses. *Neuroimage*, *7*, 30–40.

Jehee, J. F. M., Brady, D. K., & Tong, F. (2011). Attention improves encoding of task-relevant features in the human visual cortex. *The Journal of Neuroscience*, *31*(22), 8210–8219.

Kok, P., Failing, M. F., & de Lange, F. P. (2014). Prior expectations evoke stimulus templates in the primary visual cortex. *Journal of Cognitive Neuroscience*, *26*, 1546–1554.

Kok, P., Jehee, J. F. M., & de Lange, F. P. (2012a). Less is more: expectation sharpens representations in the primary visual cortex. *Neuron*, *75*(2), 265–270.

Kok, P., Rahnev, D., Jehee, J. F. M., Lau, H. C., & de Lange F. P. (2012b). Attention reverses the effect of prediction by silencing sensory signals. *Cerebral Cortex*, *22*(9), 2197–2206.

Lavie, N. (2005). Distracted and confused? Selective attention under load. *Trends in Cognitive Sciences*, *9*(2), 75–82.

Lavie, N., Hirst, A., de Fockert, J. W., & Viding, E. (2004). Load theory of selective attention and cognitive control. J*ournal of Experimental Psychology – General*, *133*(3), 339–354.

Liu, T., Larsson, J., & Carrasco, M. (2007). Feature-based attention modulates orientation-selective responses in human visual cortex. *Neuron*, *5*(2), 313–323.

Liu, T., & Mance, I. M. (2011). The spatial gradient of the spread of feature-based attention. *Vision Research*, *51*, 26–33.

Lund, T. E., Norgaard, M. D., Rostrup, E., Rowe, J. B., & Paulson, O. B. (2005). Motion or activity: their role in intra- and inter-subject variation in fMRI. *Neuroimage*, *26*, 960–964.

Martinez-Trujillo, J. C., & Treue, S. (2004). Feature-based attention increases the selectivity of population responses in primate visual cortex. *Current Biology*, *14*, 744–751.

Maunsell, J. H. R., & Treue, S. (2006). Feature-based attention in visual cortex. *Trends in Neurosciences*, *29*, 317–322.

Melcher, D., Papathomas, T. V., & Vidnyánszky, Z. (2005). Implicit attentional selection of bound visual features. *Neuron*, *46*(5), 723–729.

Serences, J. T., & Boynton, G. M. (2007). Feature-based attentional modulations in the absence of direct visual stimulation. *Neuron*, *55*(2), 301–312.

Sereno, M. I., Dale, A. M., Reppas, J. B., Kwong, K. K., Belliveau, J. W., Brady, T. J., Rosen, B. R., & Tootell, R. B. (1995). Borders of multiple visual areas in humans revealed by functional magnetic resonance imaging. *Science*, *268*, 889–893.

Summerfield, C., & Egner, T. (2009). Expectation (and attention) in visual cognition. *Trends in Cognitive Sciences*, *13*(9), 403–409.

Summerfield, C., Trittschuh, E. H., Monti, J. M., Mesulam, M. M., & Egner, T. (2008). Neural repetition suppression reflects fulfilled perceptual expectations. *Nature Neuroscience*, *11*, 1004–1006.

Todorovic, A., van Ede, F., Maris, E., & de Lange, F. P. (2011). Prior expectation mediates neural adaptation to repeated sounds in the auditory cortex: an MEG study. *Journal of Neuroscience*, *31*, 9118–9123.

Treue, S., & Martinez-Trujillo, J. C. (1999). Feature-based attention influences motion processing gain in macaque visual cortex. *Nature*, *399*, 575–579.

Watson, A. B., & Pelli, D. G. (1983). Quest: a Bayesian adaptive psychometric method. *Perception & Psychophysics*, *33*(2), 113–120.

Inter-Subject Variability in Resting-State fMRI Connectivity Predicts fMRI Activation in a Language Task

Lorijn Zaadnoordijk[1]
Supervisor: Hubert Fonteijn[1]

[1]Radboud University Nijmegen, Donders Institute for Brain, Cognition and Behaviour, Donders Centre for Cognitive Neuroimaging, The Netherlands

The spatial response observed during functional magnetic resonance imaging (fMRI) experiments is generally highly variable across subjects. In the current study, we disentangled the inter-subject variability that reflects differences in the network topology of the brain and the variability caused by other effects (e.g., task compliance or engagement). Using resting-state connectivity and task-based activation during a language task, we found significant correlations between inter-subject variability across the two measures. The strength with which a region is connected to the language network during rest is found to be predictive of how active it is during language processing. This finding demonstrates that a significant portion of the inter-subject variability observed in fMRI studies can be related to inter-individual differences in brain organization.

Keywords: fMRI, network topology, language processing, inter-subject variability

Corresponding author: Lorijn Zaadnoordijk; **E-mail**: l.zaadnoordijk@donders.ru.nl

1. Introduction

A considerable amount of inter-subject variability in activation strength is observed in experiments using functional magnetic resonance imaging (fMRI). Generally, in these experiments, a group's average brain activity is computed per task or condition, and any inter-subject variability is considered a nuisance. The underlying factors that cause this variability are often unknown. This poses a problem for a full understanding of the functioning of the brain. To get a proper understanding and interpretation of the observed brain activity, it is crucial to know what sources are contributing to it. The aim of the current research is to characterize this inter-subject variability, and to disentangle the different underlying causes. Finding the causes of inter-subject variability in fMRI data will result in a better understanding of these types of data.

Inter-subject variability can arise from differences in the organization and function of the brain, as well as experimental factors, such as task compliance, task engagement or noise. Disentangling the biological from the experimental factors allows neuroscientists to understand the observed brain activity and the differences in brain activity across subjects. This disentanglement becomes increasingly important since neuroscience and genetics have been brought together in the field of imaging genetics. In imaging genetics it is assumed that an individual's genotype will have an effect on the brain's anatomy and functional activity. Previous research has shown that using the genome to find differences in neuroanatomy and functional neuronal activity is successful. Such research was carried out, for instance, on psychiatric disorders such as attention deficit hyperactivity disorder, anxiety disorders and schizophrenia (e.g., Bédard et al., 2010; Domschke & Dannlowski, 2010; Durston, 2010; Potkin et al., 2008). Furthermore, a relation between genetic profiles and functional activation has been established in a number of task-based fMRI experiments (e.g., Goldberg & Weinberger, 2004; Pinel et al., 2012; Snijders, 2010) and in resting-state fMRI experiments (Glahn et al., 2010).

Neuroimaging data, however, provide a large number of potential endophenotypes. To reduce the multiple comparisons problem, a selection of endophenotypes must be made. Making an informed decision based on the efficiency of these endophenotypes is thus of great importance. The current study sets out to aid in this decision process by addressing two important questions. The first question that is addressed pertains to the uniqueness of the variability that is observed within a single region. Often, the variability in brain activity of a single region is selected as an endophenotype. It is unclear, however, how unique the inter-subject variability of a single region is, and thus whether the variability of each individual region can serve as an efficient endophenotype. If the variability of a region correlates very highly with the variability of many other regions, using that region as an endophenotype may not be the most efficient choice. The current research explores this question by computing the co-activation between regions across the brain. The characterization of this co-activation will lead to a better understanding of the uniqueness of the inter-subject variability of activation strength within a region, and, by extension, its efficiency as an endophenotype.

The second question that will be addressed pertains to the disentanglement of underlying factors that are contributing to the brain activity. We aim to locate and isolate the portion of the inter-subject variability observed in functional experiments that can be linked to differences in the functional organization of the brain. This type of variability is most likely to have a more fundamental biological basis and may therefore be more strongly connected to the genome. When considering the functional organization of the brain, the activation level of a region could be influenced by many factors, one of which is network topology. Resting-state fMRI has emerged as a powerful method to characterize the connectivity of brain regions. In resting-state fMRI experiments, participants are scanned without being engaged in a particular cognitive task. The activity patterns observed during resting-state are thought to reflect spontaneous fluctuations in the BOLD signal (Damoiseaux et al., 2006), and are thus not task-evoked. When a set of regions show correlated spontaneous activity without being engaged in a specific cognitive process, this is called a resting-state network. Interestingly, areas that are part of the same resting-state network are often also involved in the same cognitive process (see Smith et al., 2009). Among those resting-state networks are the language networks, which roughly consist of the inferior frontal gyrus (IFG), middle and superior temporal gyrus (MTG, STG), and parts of the inferior parietal cortex (Xiang, Fonteijn, Norris, & Hagoort, 2010). Similar to task-based fMRI experiments, in resting-state fMRI experiments a large amount of inter-subject variability is observed (Mueller et al., 2013). In this type of data, the inter-subject variability generally reflects differences in the

network topology of the resting-state networks.

The substantial amount of variability in activation and connectivity patterns between subjects raises questions about the potential sources of these differences. As the inter-subject variability is found in both task-based and resting-state fMRI data, it is likely that parts of this variability are caused by differences in the functional organization of the brain. These differences may be reflected in both task-based and resting-state data as activation and connectivity are closely linked. The activation of a brain region is determined by its input and output. Previous work has shown that resting-state connectivity profiles were predictive of inter-individual differences in task activation during an Eriksen Flanker task (Mennes et al., 2010). Using task-based and resting-state fMRI, the aim of this study is to find shared sources of inter-subject variability in network topology and task activation of a language task. These two functional measures of brain activation, where one shows network topology through spontaneous activity, and the other shows evoked activity specifically for language processing, enable us to compare the effect of functional organization on both sets of imaging data. We will correlate the inter-subject variability found in the resting-state connectivity strength and in the task-based activation strength across subjects to map the variability that is shared across the two data types. Correlated variability will be considered to be caused by functional organization rather than task-related effects, such as task compliance or task engagement. To characterize this type of inter-subject variability reliably, a large cohort is required. Therefore, the current study is conducted as part of a larger project (the Mother Of all Unification Studies [MOUS] project) in which the neurobiology of language in general, and semantic and syntactic integration specifically, are studied within different perceptual modalities (see Box 1 for details).

The present study characterizes correlated inter-

Box 1: The MOUS Project

Background: The MOUS project (a large-cohort study [N=204]) was set up to investigate the neural mechanisms of sentence processing (unification/integration) based on the Memory-Unification-Control model (Hagoort, 2005). In this model, unification (or integration) is considered to be a combinatorial process during which retrieved lexical components (e.g., words) are integrated into larger meaningful units (e.g., sentences). Using a variety of techniques, such as magnetoencephalography (MEG), fMRI, magnetic resonance spectroscopy, and diffusion tensor imaging (DTI), the aim of the MOUS project is to investigate whether the neural underpinnings for unification are common across language domains (e.g., reading, listening). Furthermore, the neuroimaging data of the participants are analyzed together with their genetic data in order to find genetic profiles that modulate these neural mechanisms and cause individual differences.

Stimuli: The stimuli consisted of 204 Dutch sentences of nine to 15 words that did not exceed a length of 11 letters. By scrambling the sentences, 204 corresponding word sequences were created. The word sequences were controlled to not contain a coherent sentence fragment of three or more words. The stimuli were presented visually or auditorily to the participants. The sentences and sequences were randomly divided into six sets of 60 unique sentences (30 per condition) and 60 unique word sequences. The sets were balanced across participants, who were presented with only one set (i.e., they were presented with 60 sentence trials and 60 word sequence trials). To monitor and maintain their attention, after 10% of the trials, a comprehension question was asked.

fMRI acquisition procedure: Before going into the scanner, participants received instructions in Dutch regarding regular MRI-scanner protocols and the experimental task. Participants were asked to move as little as possible while being in the scanner. For the acquisition of the resting-state data, participants were instructed to keep their eyes closed and to "think of nothing in particular". The task consisted of 24 mini blocks of sentences or word sequences (three to four sentences or sequences per block). At the start of each block, the label "Zinnen" (Sentences) or "Woorden" (Words) was displayed on the screen. Participants were instructed to try to read or listen to the words in the sequence conditions as separate words, that is, the words were not supposed to be integrated into a meaningful sentence. To answer the comprehension questions, a button box was provided to the participant. All participants used their left index finger to answer 'Yes' and their left middle finger to answer 'No'. Between trials, a fixation cross was shown to the participants, which serves the purpose of being a low-level baseline in the analyses. The task took approximately 25 minutes to complete.

individual variability in the spatial response between resting-state and task-based fMRI data. We will explore where potential shared sources of variability are, and will investigate the role of network topology on language processing. Additionally, we investigate to what extent variability in a single region is unique, and therefore how efficient it is as an endophenotype. In order to do this, it is necessary to have clearly defined regions. Regions can be defined by anatomical properties (e.g., cytoarchitectonic features), be adopted from previous studies or be based on functional properties. Regions extracted from anatomical parcellations are often too coarse and do not fully overlap with function. Adopting regions from findings reported in the literature is also problematic as it is difficult to find a whole brain parcellation. Therefore, the regions in this study are defined by a functional parcellation. In a functional parcellation, voxels that are functionally similar (based on similarity in time courses) are clustered together. Additionally, functional parcellation serves as an efficient form of data reduction. Computing connectivity patterns between parcels rather than voxels reduces the multiple comparisons problem that arises from this type of research. Methods that have been proposed for parcellation include independent component analysis (Beckmann, DeLuca, Devlin, & Smith, 2005; Calhoun, Adali, Pearlson, & Pekar, 2001) and clustering analyses (Cordes, Bassett, Power, Braver, & Petersen, 2002; Fonteijn, 2011; Van den Heuvel, Mandl, & Hulshoff, 2008). The type of parcellation method that is used does not seem to have a great influence on the resting-state networks that result from the analyses (Van den Heuvel & Hulshoff Pol, 2010). Functional parcellation thus appears to be a robust basis for doing region to region analyses.

2. Material and methods

2.1 Participants

One hundred and two participants (50 male, 52 female) with a mean age of 22.25 years old (age range: 18 to 33 years old) were included for analysis. These participants are a subset of participants who took part in a large-cohort study (the MOUS project, see Box 1). In this study, a large body of data was acquired with different imaging techniques (e.g., MEG, MRI) in two conditions: half of the participants were presented auditory stimuli, for the other half, the presentation was visual. In the current study, we analyzed the fMRI data of the participants in the visual condition only.

All participants were right-handed native Dutch speakers with normal or corrected-to-normal vision. Additionally, they were screened for developmental, neurological and psychiatric disorders. Participants gave informed consent in accordance with the CMO (the local "Committee on Research Involving Human Subjects" in the Arnhem-Nijmegen region) ethics committee.

2.2 Data acquisition

The data were acquired with a SIEMENS Trio 3T scanner using a 32-channel head coil. The order of the data acquisition was as follows: resting-state fMRI, GABA spectroscopy, DTI, task-based fMRI, structural image. As this paper is concerned with the resting-state and task-based fMRI data, the acquisition parameters for these types and for the structural image are given below.

2.2.1 Resting-state fMRI data acquisition

T_2^*-weighted functional EPI-BOLD images (whole brain coverage) were acquired with a standard 2D gradient-echo echo-planar imaging sequence (TR = 1680 ms, TE = 30 ms, 70° flip-angle, slice-matrix = 64x64, FOV = 256 mm, anisotropic voxel size = 3.5x3.5x3.0 mm, slice orientation = I >> S).

2.2.2 Task-based fMRI data acquisition

T_2^*-weighted functional EPI-BOLD images (partial brain coverage) were acquired with a single echo 2D gradient-echo echo-planar imaging sequence (TR = 2000 ms, TE = 35 ms, 90° flip-angle, 29 oblique slices (phase encoding direction = A >> P), slice-matrix = 64x64, slice thickness = 3.0 mm, slice gap = 0.5 mm, FOV = 224 mm, anisotropic voxel size = 3.5x3.5x3.0 mm). The stimuli were back-projected on a screen at the head of the scanner. An angled mirror attached to the head coil enabled participants to view the stimuli.

2.2.2 Task-based fMRI data acquisition

T_2^*-weighted functional EPI-BOLD images (partial brain coverage) were acquired with a single echo 2D gradient-echo echo-planar imaging sequence (TR = 2000 ms, TE = 35 ms, 90° flip-angle, 29 oblique slices (phase encoding direction = A >> P), slice-matrix = 64x64, slice thickness = 3.0 mm, slice gap = 0.5 mm, FOV = 224 mm, anisotropic voxel size = 3.5 x 3.5 x 3.0 mm). The

stimuli were back-projected on a screen at the head of the scanner. An angled mirror attached to the head coil enabled participants to view the stimuli.

2.2.3 Structural image acquisition

A high-resolution T_1-weighted magnetization-prepared rapid gradient-echo pulse sequence was used (MP-RAGE; TR = 2530 ms, TE = 3.37 ms, 7° flip-angle, 1 slab, slice-matrix = 256x256, slice thickness = 1 mm, FOV = 256 mm, isotropic voxel-size = 1.0x1.0x1.0 mm).

2.3 Image preprocessing

The data were preprocessed with statistical parametric mapping software (SPM8; Wellcome Trust Centre for Neuroimaging, London, UK) as follows.

2.3.1 Task-based fMRI data

The first three EPI-BOLD volumes were removed to ensure a T_1 equilibrium. The remaining functional volumes were de-spiked (there were 20 affected volumes distributed across 7 subjects) and realigned to correct for subject movement in the scanner. The mean EPI-BOLD volume was coregistered to the structural image, after which this transformation was applied to all functional volumes. The structural image template provided by SPM8 was used as a basis for spatial normalization (using affine transformation only) of the structural images. The resulting transformation matrix was used to transform the EPI-BOLD volumes to standard space. The EPI-BOLD volumes were re-sliced to a resolution of 2x2x2 mm, and spatially filtered with an isotropic 3D spatial Gaussian filter kernel (FWHM = 6 mm).

2.3.2 Resting-state fMRI data

The first three volumes were removed to ensure a T_1 equilibrium. The remaining functional volumes were realigned to correct for subject movement in the scanner. The mean functional volume was co-registered to the structural image, after which this transformation was applied to all functional volumes. The structural image template provided by SPM8 was used as a basis for spatial normalization (using affine and non-affine transformation) of the structural images. The resting-state volumes were normalized with the transformation matrices that were generated from this algorithm, resliced to a resolution of 3x3x3 mm, and spatially filtered with an isotropic 3D spatial Gaussian filter kernel (FWHM = 6 mm).

2.4 Definition of nuisance regressors

The structural image was segmented into gray matter, white matter and cerebrospinal fluid (CSF). This segmentation was used to define the mean time course from the white matter and CSF information. Nuissance regressors were formed by the white matter and CSF mean time course and six motion parameters (translation and rotation). The resting-state data and nuisance regressors were temporally filtered with a bandpass filter ($0.008 \text{ Hz} < f < 0.1$ Hz), the temporal filtering of the task data was done with a high-pass filter ($f > 0.008$ Hz). The nuissance regressors were then removed from the functional data by linear regression.

2.5 Data analysis

2.5.1 Contrasts

Contrast images were used as a basis for the activation analyses of the present research. The linear model included two kinds of explanatory regressors: (1) movement regressors and (2) experimental conditions (sentence conditions, word sequences conditions, baseline conditions and the filler condition). The regressors were convolved with a canonical hemodynamic response function. We used the contrast images for these two contrasts: Sentences versus Baseline (SvsB), which is a general contrast that shows where brain activation for reading sentences is greater than during the low-level baseline (a fixation cross), and Sentences versus Word sequences (SvsW), where it is assumed that unification processes are engaged more during the processing of sentences than word sequences.

2.5.2 Data-driven parcellation

The clusters for our analyses were defined by a functional parcellation. First, a functional parcellation was computed for each participant individually, by entering a sparse voxel-voxel similarity matrix (keeping the first 500 nearest neighbors in terms of functional similarity) into an in-house implementation of the normalized cuts algorithm (Shi and Malik, 2000). This greedy algorithm starts by dividing the data into 15 functional networks (roughly equivalent to the number of networks in

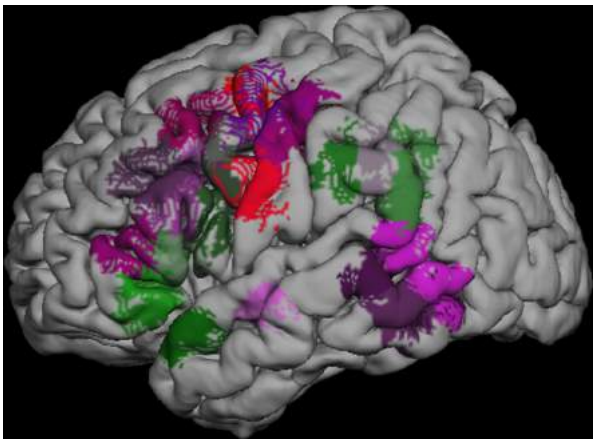

Fig. 1. Overview of selected ROIs from the group parcellation.

Power et al., 2011). Then it divides the network into two clusters, which are each divided into two clusters, while evaluating for each division which subdivision is the most optimal. Each hemisphere was parcellated separately into 150 clusters for each participant. These divisions are made purely based on similarity in time courses, that is, there was no spatial constraint on the cluster formation, leading to several cases where a single cluster was spread over multiple regions of the brain. In these cases, the parcel was broken up into its constituting spatially distinct regions and assigned a new cluster number if the region was larger than 60 voxels in the task-based data and larger than 20 voxels in the resting-state data (this difference is a reflection of the differences in voxel size between the two data types). This resulted in a varying number of clusters for each subject.

In order to answer the question whether the task-based or resting-state data should be used as the basis for the functional parcellation, we computed a functional parcellation image for both data types for a set of pilot subjects (N=17). Next, functional connectivity (cluster-to-voxel) was calculated for both data types by using the parcels of both parcellation images as seed-regions. Having obtained functional connectivity for two data types using two different parcellations as seed regions, this led to functional connectivity profiles for each participant in four situations: (1) functional connectivity of the task time courses using the parcels from the task parcellation, (2) functional connectivity of the task time courses using the parcels from the resting-state parcellation, (3) functional connectivity of the resting-state time courses using the task parcellation, and (4) functional connectivity of the resting-state time courses using the resting-state parcellation. In situations 1 and 4, the functional connectivity profiles will be optimal as their seed regions were extracted from the same data. Situations 2 and 3, on the other hand, are interesting because there the non-optimal parcels are used to calculate cluster-to-voxel connectivity. Comparing the optimal to the suboptimal situation per data type enabled us to determine which functional parcellation led to the smallest information loss when compared to the optimal parcellation of the same data type. This correlation is spatial in nature; it measures how well the spatial distribution of the parcels in the optimal and suboptimal situation matches with the functionally connected voxels. The crossover caused a minor information loss in both cases. For most participants (N=13), however, the least information was lost (i.e., the correlation between connectivity patterns of the optimal and the suboptimal combination of parcels and time courses was the highest) for the task-based parcellation. Therefore, the group parcellation was computed based on the task data.

The group parcellation was created by again computing a sparse similarity matrix. For the group parcellation, however, the similarity matrix was computed for all voxel-pairs based on how often the voxel-pairs were present in the same cluster across subjects (based on Van den Heuvel et al., 2008). This matrix thus shows how consistently two voxels belong to the same functional network across participants. Only the 500 nearest neighbors in terms of similarity of clustering across subjects were kept. This matrix was entered into the modified normalized cuts algorithm to redefine the clusters. The median of the number of clusters per participant per hemisphere was taken as the number of clusters that had to be defined in the group parcellation. This resulted in 351 clusters in total (175/176 clusters for the left/right hemisphere). The parcels of the group parcellation were used as regions of interest.

2.5.3 ROI selection

For further analysis, 29 clusters from the core language network were selected as regions/clusters of interest (ROIs). The selection of these clusters was based on the regions of activation reported by Snijders et al. (2010) and Pinel et al. (2012) who investigated the influence of genetic profiles on the language network. In addition, clusters in the angular gyrus were chosen, as they are thought to be involved in semantic integration (Binder et al., 2009). Next to these clusters, a few adjacent clusters in the postcentral gyrus and supramarginal gyrus were included. Figure 1 shows an overview of all clusters that were selected as ROIs.

2.5.4 Resting-state connectivity analysis

For illustrative purposes, we computed voxel-wise functional connectivity patterns for the resting-state data by correlating the mean time-course of a cluster to the time courses of all voxels in the brain. Statistical significance was then computed for each voxel in a random-effects fashion by performing a t-test on the z-transformed correlation values across subjects. The resulting patterns were very similar to the connectivity patterns that were previously reported in the literature (e.g., Damoiseaux et al., 2006; Xiang et al., 2010), indicating that the resting-state data of our sample are of comparable quality to other studies and that the parcellation procedure leads to biologically plausible regions. Next, we computed functional connectivity between cluster pairs by computing the correlation between their respective time courses. These correlation values are the basis for all subsequent analyses.

2.5.5 Task co-activation analysis

The task co-activation analysis was conducted to investigate how much the level of activation of a (ROI) cluster correlates with the other clusters' (whole-brain) activation level across subjects. Note that a significant correlation in this analysis does not mean that the area activates above threshold in a standard activation analysis, instead it is a measure of consistency of the co-activation of two areas across participants. Co-activation was determined for two separate contrasts: SvsB and SvsW sequences (see Box 1 for details). For each of these contrast images, the contrast values were extracted per voxel and averaged within clusters, leading to an average cluster activation value for each contrast. These values were then correlated with each other across subjects, as a measure of the consistency with which clusters show a similar kind of activation pattern. This analysis was conducted twice; in the second analysis the mean contrast level was regressed out of the data to remove non-language-specific effects from the data. A false discovery rate (FDR) correction was applied to the correlation results to correct for multiple comparisons.

2.5.6 Connectivity-activation analysis

As one of the main goals of the current studies is to investigate to what extent inter-subject variability in task fMRI data is driven by the intrinsic functional organization of the brain (i.e., network topology), the activation of a (ROI) seed cluster during the task was correlated with the connectivity strength between that seed cluster and other clusters (whole-brain) during rest. The activation of the seed cluster was determined, as in the co-activation analysis, by taking the average value in the contrast images. The connectivity strength was defined as the z-transformed correlation value of the mean time courses of two clusters (see also the subparagraph on resting-state connectivity). Again, an FDR correction was applied to the correlation results to correct for multiple comparisons.

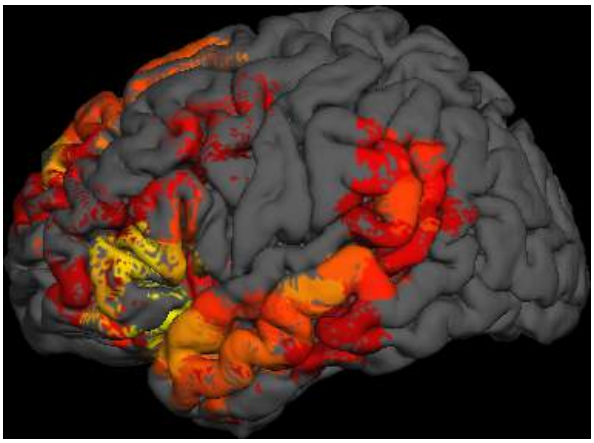

Fig. 2. Example of a resting-state connectivity pattern in a language network (seed region: pars orbitalis).

3. Results

Considering the number of results, only the most relevant results are reported here. A complete overview of all results, including the supplementary material, can be obtained by contacting the author or can be retrieved from the journal website.

3.1 Resting-state connectivity

The functional connectivity patterns obtained from the resting-state fMRI data showed the well-known resting-state networks. Finding the standard resting-state networks in this parcel-based connectivity analysis is reassuring. It demonstrates that the parcellation method leads to a plausible functional parcellation. The language networks that we found were both dorsal and ventral networks, involving the regions that are associated with these networks (e.g., inferior frontal gyrus, superior and middle temporal gyrus, angular gyrus). In Figure 2 an example of a language network is shown, where a cluster in the pars orbitalis is used as a seed region.

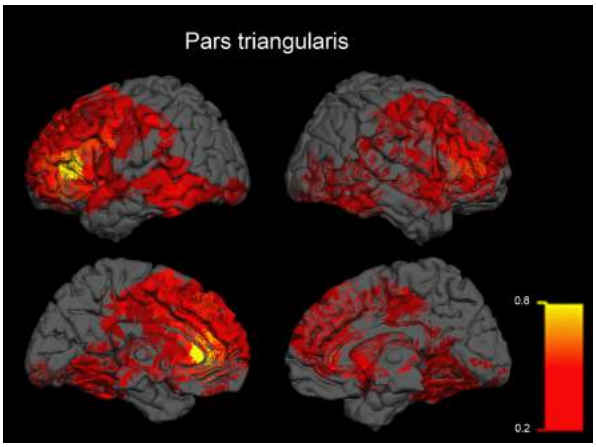

Fig. 3. Correlation map ($p < .05$, FDR corrected, positive correlations only) of the clusters whose activation is significantly correlates with that of the seed cluster (pars triangularis; depicted in yellow) for the SvsB contrast.

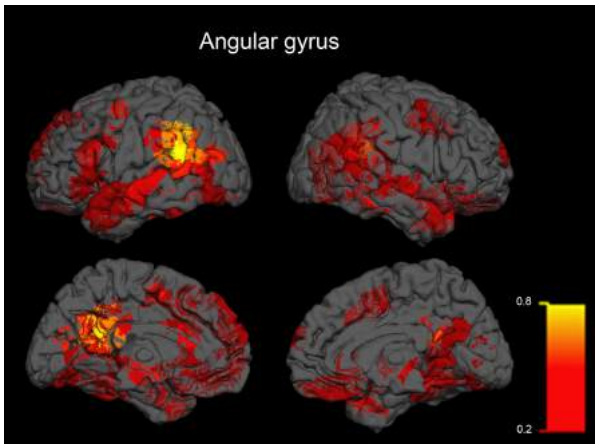

Fig. 4. Correlation map ($p < .05$, FDR corrected, positive correlations only) of the clusters whose activation is significantly correlates with that of the seed cluster (angular gyrus; depicted in yellow) for the SvsB contrast.

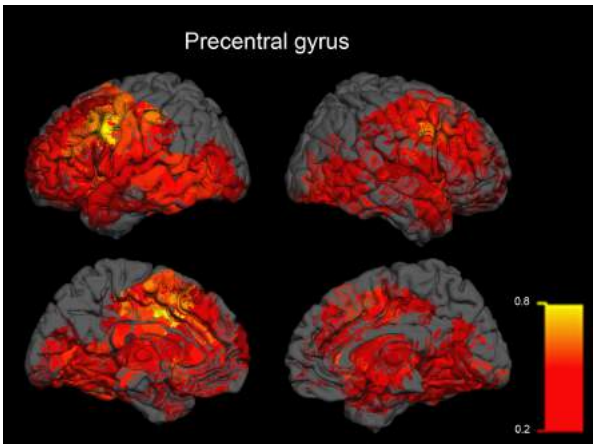

Fig. 5. Correlation map ($p < .05$, FDR corrected, positive correlations only) of the clusters whose activation is significantly correlates with that of the seed cluster (precentral gyrus; depicted in yellow) for the SvsB contrast.

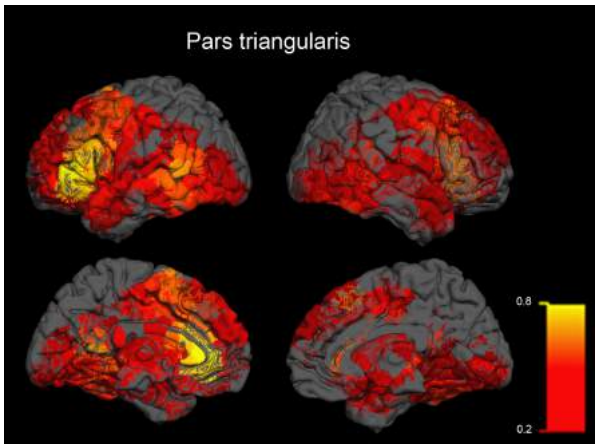

Fig. 6. Correlation map ($p < .05$, FDR corrected, positive correlations only) of the clusters whose activation is significantly correlates with that of the seed cluster (pars triangularis; depicted in yellow) for the SvsW contrast.

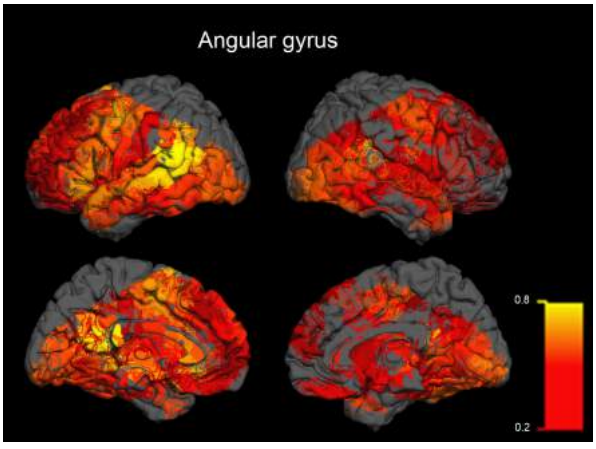

Fig. 7. Correlation map ($p < .05$, FDR corrected, positive correlations only) of the clusters whose activation is significantly correlates with that of the seed cluster (angular gyrus; depicted in yellow) for the SvsW contrast.

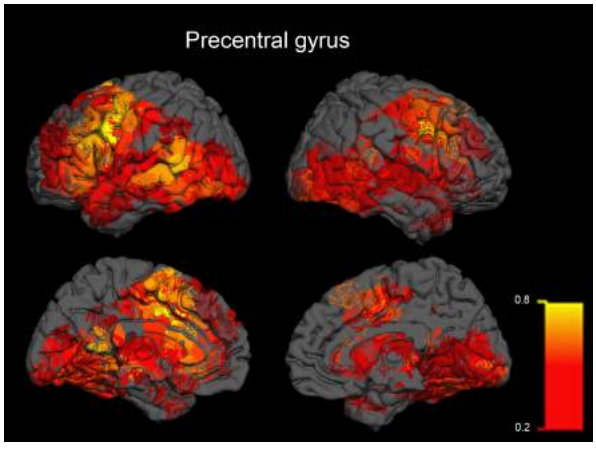

Fig. 8. Correlation map ($p < .05$, FDR corrected, positive correlations only) of the clusters whose activation is significantly correlates with that of the seed cluster (precentral gyrus; depicted in yellow) for the SvsW contrast.

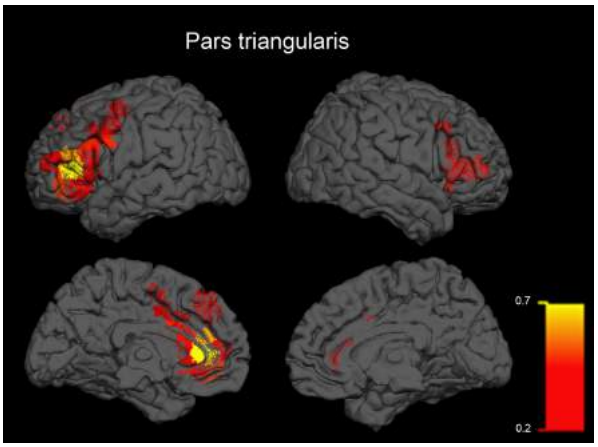

Fig. 9. Correlation map ($p < .05$, FDR corrected, positive correlations only) of the clusters whose activation is significantly correlates with that of the seed cluster (pars triangularis; depicted in yellow) for the SvsB contrast after mean signal removal.

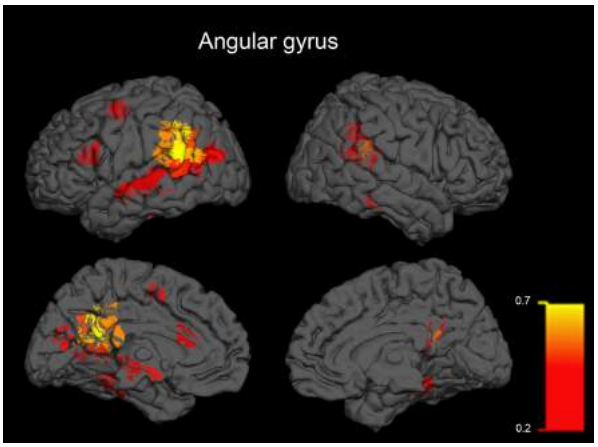

Fig. 10. Correlation map ($p < .05$, FDR corrected, positive correlations only) of the clusters whose activation is significantly correlates with that of the seed cluster (angular gyrus; depicted in yellow) for the SvsB contrast after mean signal removal.

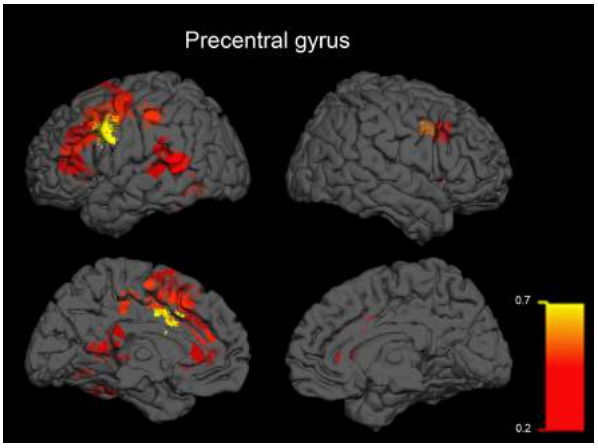

Fig. 11. Correlation map ($p < .05$, FDR corrected, positive correlations only) of the clusters whose activation is significantly correlates with that of the seed cluster (precentral gyrus; depicted in yellow) for the SvsB contrast after mean signal removal.

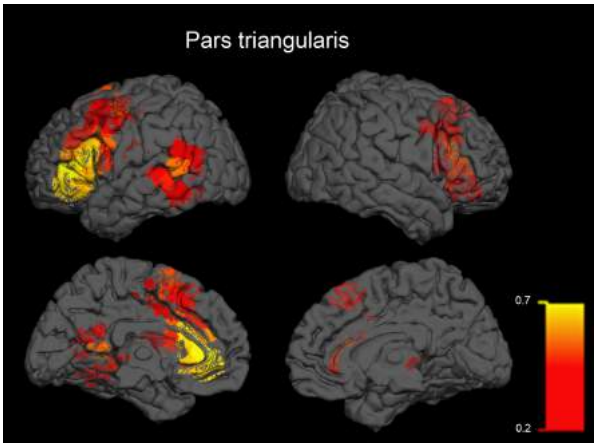

Fig. 12. Correlation map ($p < .05$, FDR corrected, positive correlations only) of the clusters whose activation is significantly correlates with that of the seed cluster (pars triangularis; depicted in yellow) for the SvsW contrast after mean signal removal.

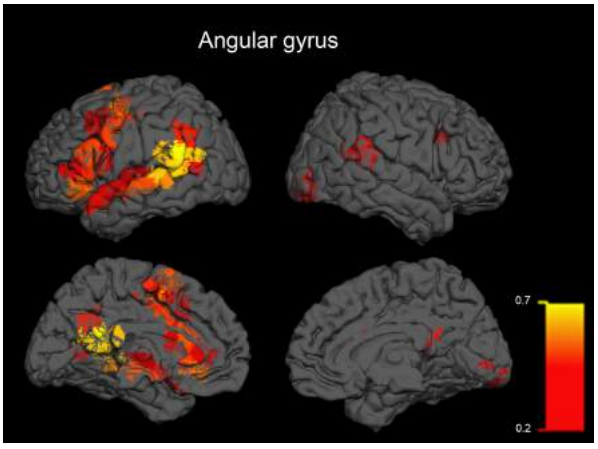

Fig. 13. Correlation map ($p < .05$, FDR corrected, positive correlations only) of the clusters whose activation is significantly correlates with that of the seed cluster (angular gyrus; depicted in yellow) for the SvsW contrast after mean signal removal.

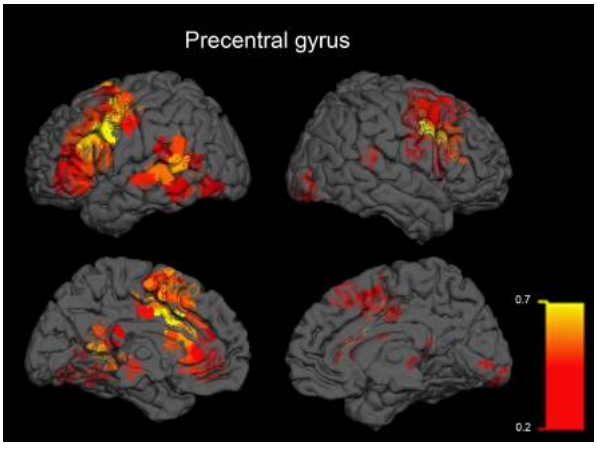

Fig. 14. Correlation map ($p < .05$, FDR corrected, positive correlations only) of the clusters whose activation is significantly correlates with that of the seed cluster (precentral gyrus; depicted in yellow) for the SvsW contrast after mean signal removal.

3.2 Task co-activation

The activation of each of the 29 ROIs is highly correlated with a very large number of clusters across subjects throughout the brain. This applies to both the SvsB and SvsW contrasts, although a noticeable difference between the contrasts is observed in the co-activation patterns in posterior brain regions, such as angular and supramarginal gyrus. They show larger patterns of co-activation in the integration specific contrast (SvsW) than in the general contrast (SvsB). Figures 3-8 illustrate the co-activation patterns of a region in the pars triangularis, angular gyrus and precentral gyrus in both contrasts.

The large patterns of co-activation with language regions in the two language contrasts, including regions well outside the traditional network (e.g., primary visual and auditory cortex, frontal pole and cerebellum), point to the presence of a generic effect that is to some extent aspecific to language and certainly not specific to the co-activation pattern of any individual pair of regions. We have therefore removed this aspecific effect by removing the mean contrast level of each subject (averaged across all regions) from the contrast level of each region. This procedure is similar to the mean signal regression strategies that are used in the resting-state fMRI literature to remove the effect of the global signal from the connectivity patterns. As with the methods used in the resting-state fMRI literature, the resulting co-activation patterns should be interpreted with care, since global signal removal can induce anti-correlations that are purely artifactual (Murphy, Birn, Handwerker, Jones, & Bandettini, 2009). The aim of this analysis was purely to investigate whether more specific networks of co-activation remained after the removal of the global level of activation of each subject. This was indeed the case: co-activation maps (Figures 9-14) now show significant co-activation that is largely restricted to the language network (inferior frontal gyrus, precentral gyrus, angular gyrus and parts of the superior and middle temporal gyrus).

3.3 Connectivity-activation analysis

For each ROI the mean contrast value of activation was correlated with the connectivity strength of that ROI with the other clusters in the brain across subjects. For the SvsB contrast, we found significant positive and negative correlations for 21 of the 29 ROIs after correction for multiple comparisons. The SvsW contrast did not yield any significant results. In the remainder, we will discuss the SvsB results further.

The angular gyrus, middle and inferior frontal gyrus and the precentral gyrus showed a correlation between network topology and activation levels. More specifically, when these regions are more functionally connected to the parts of the language network (middle and superior temporal gyrus and angular gyrus especially) during rest, they activate more strongly during language processing. This pattern is observed, for instance, in the pars triangularis. When this region has a stronger functional connection to middle temporal gyrus and angular gyrus during rest, its activation increases while processing sentences (see Figure 15). Negative correlations were also observed, suggesting that a stronger functional connectivity with areas outside

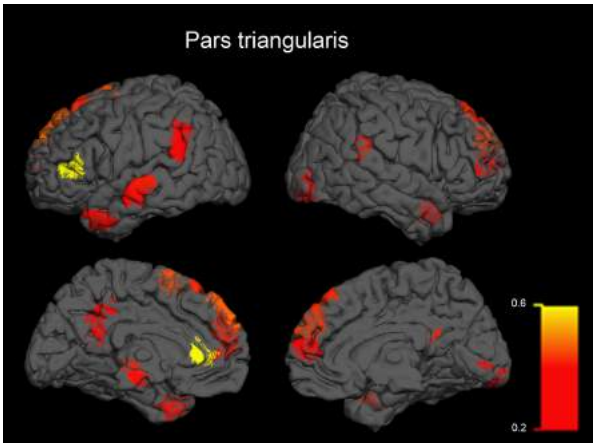

Fig. 15. Correlation map ($p < .05$, FDR corrected, positive correlations only) of the clusters whose connectivity strength to the seed cluster (pars triangularis; depicted in yellow) significantly correlates with the task activation of the seed cluster for the SvsB contrast.

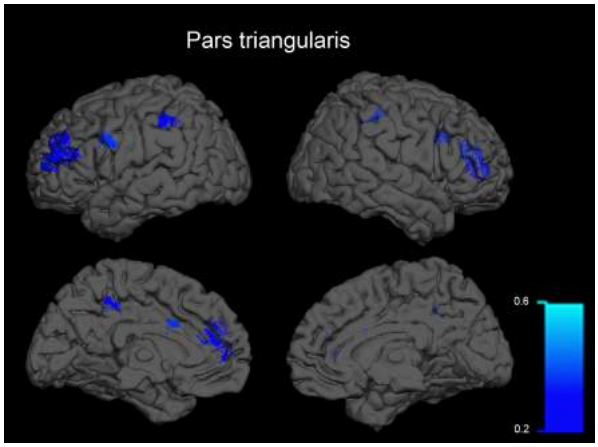

Fig. 16. Correlation map ($p < .05$, FDR corrected, negative correlations only) of the clusters whose connectivity strength to the seed cluster (pars triangularis) significantly correlates with the task activation of the seed cluster for the SvsB contrast.

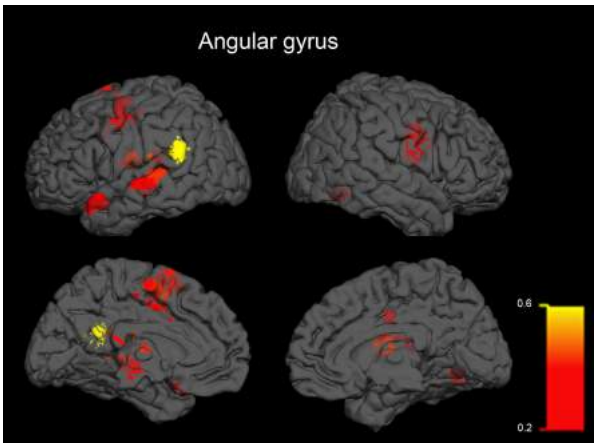

Fig. 17. Correlation map ($p < .05$, FDR corrected, positive correlations only) of the clusters whose connectivity strength to the seed cluster (angular gyrus; depicted in yellow) significantly correlates with the task activation of the seed cluster for the SvsB contrast.

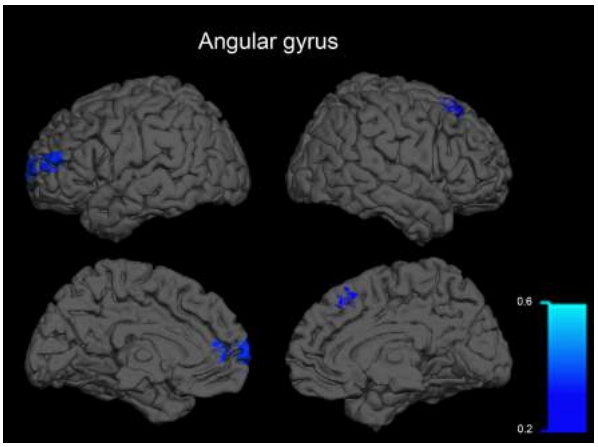

Fig. 18. Correlation map ($p < .05$, FDR corrected, negative correlations only) of the clusters whose connectivity strength to the seed cluster (angular gyrus) significantly correlates with the task activation of the seed cluster for the SvsB contrast.

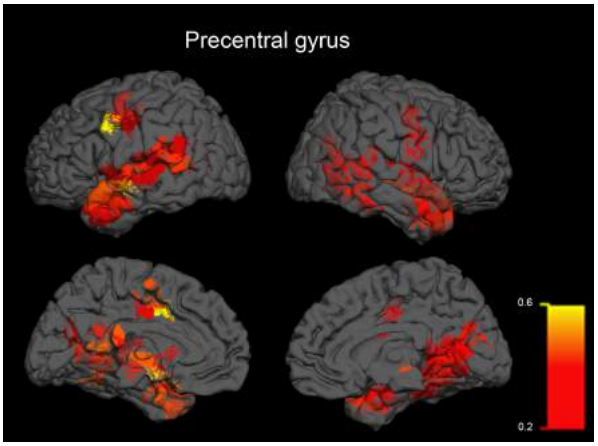

Fig. 19. Correlation map ($p < .05$, FDR corrected, positive correlations only) of the clusters whose connectivity strength to the seed cluster (precentral gyrus; depicted in yellow) significantly correlates with the task activation of the seed cluster for the SvsB contrast.

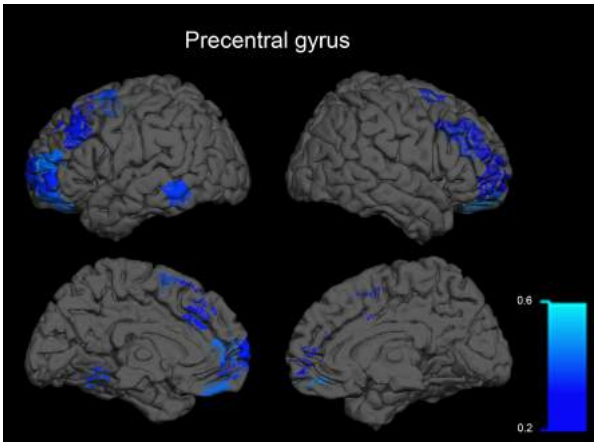

Fig. 20. Correlation map ($p < .05$, FDR corrected, negative correlations only) of the clusters whose connectivity strength to the seed cluster (precentral gyrus) significantly correlates with the task activation of the seed cluster for the SvsB contrast.

of the language network result in a lower activation level during the language task. Interestingly, most of the negative correlations that we find are clustered around the frontal pole (see Figures 18 and 20). That is, when a region has stronger functional connectivity to the frontal pole, its activation during sentence processing is lower. Generally, inter-subject activation in the temporal lobe, frontal operculum and supramarginal gyrus was not correlated with inter-subject variability in network topology.

The results of the precentral gyrus stood out in the activation-connectivity analysis in terms of the number of positive and negative correlations found (see Figures 19 and 20). The functional connectivity strength from the precentral gyrus to large parts of the superior and middle temporal gyrus, the angular gyrus and the precuneus was correlated with the activation strength of the precentral gyrus during the language task. Negative correlations were found between the precentral gyrus' activation level during the task and its connectivity strength to large parts of the prefrontal gyrus. That is, the activation of the precentral gyrus during the task was higher when it was more connected (positive correlations) to the superior and middle temporal gyrus and angular gyrus (parts of the language network) and the precuneus, and lower when it was more involved in other networks related to the prefrontal gyrus (negative correlations). The number of significant correlations is generally smaller for regions within the core language network. Examples of correlation patterns from core language regions are shown in Figures 15-18. These results indicate that the activation levels of regions within the core language

network are less susceptible to variability in their connectivity patterns.

4. Discussion

This study investigated the nature of the large amount of inter-subject variability in activation strength found in fMRI activation. We have made an attempt to disentangle the variability caused by differences in functional organization of the language networks from variability caused by experimental factors, such as compliance or engagement. The comparison of the inter-individual variability in task-based fMRI with the inter-individual variability in network topology in resting-state fMRI enabled us to investigate the existence and location of correlated variability across the two functional measures of brain activity. The rationale for this is the following: if the inter-individual variability correlates between the two measures, the variability in the task-based fMRI data cannot have been caused by task-effects alone, and therefore this portion of the variability likely arises from intrinsic functional organizational differences, as measured by resting-state fMRI. Investigating where the variability has a shared source for both resting-state and task fMRI, is helpful to obtain insight on the ways in which network topology influences cognitive processes.

To characterize the uniqueness and specificity of the variability across regions during the task, we first determined the co-activation of the brain with our ROIs. By calculating the correlation of activation between two areas during a language task, it was shown that the activation level of a very large number of regions in the brain is highly correlated with the activation levels of regions within the language network. Interestingly, this shows that the activation level of a certain region is predicted by the activation of many regions. Another observation is that the amount of co-activation is larger in the specific language-unification contrast (SvsW) than in the general language contrast (SvsB). The patterns of co-activation in the SvsW contrast were very widespread, regardless of the seed region. In the SvsB contrast, coactivation was not as high for all seed regions. Especially the more posterior regions (e.g., angular gyrus) showed a smaller extent of significant correlations. This shows that a region's strength of activation is highly correlated with the activation strength of other regions across the whole brain. These widespread correlation patterns suggest that part of the co-activation is not specific to language. Instead, it is caused by a non-language-specific effect, possibly task engagement, that activates all regions. This aspecific effect obscured a language-specific effect, as became clear after regressing the mean signal. Many language regions were found to co-activate with other language regions. The language-specific effect was again stronger for the unification contrast than for the general language contrast. Additionally, negative correlations were found, suggesting that some non-language regions (e.g., the frontal pole) de-activate when the activation of the language regions is higher. However, as discussed in the Results section, negative correlations should be interpreted with care in the context of global signal regression. The results after mean signal regression show that additional to the aspecific, global patterns of co-activation, there are also patterns of co-activation that specifically involve the language network. The extent to which one region in the language network is active during a task is thus associated with the activation level of other regions in the language network, which varies across participants.

In order to investigate the role of network topology on the inter-subject variability in fMRI data, the inter-subject variability within the resting-state functional connectivity was correlated with variability in activation during task. We only found significant correlations in the general language contrast (SvsB); no significant correlation between network topology and the specific integration contrast (SvsW) was found. This suggests that a shared variability between resting-state connectivity and task activation is found between networks that are either language or non-language related, but not in unification processes within the language network. Our results showed that for the SvsB contrast in a number of cases the activation of a region during the language task was positively correlated with the functional connectivity strength of that region to other language regions, and negatively correlated with the connectivity strength with regions outside of the language networks. This pattern is observed most strongly for regions that are peripherally involved in language processing than for the core language regions, which may indicate that the level of involvement of a peripheral region with the language network or another network is more predictive of its activation level during a language task. Interestingly, most of the negative correlations that we find are a set of regions that are clustered around the frontal pole. As the frontal pole is involved in social-emotional, cognitive processing and default mode networks (Liu et al., 2013), a region's stronger connection to these networks and

decrease in task activation may be due to a different distribution of resources between networks across participants.

Recently, Cole, Bassett, Power, Braver and Petersen (2014) have shown that next to resting-state networks there are also task-general (present during many different cognitive tasks) and task-specific networks. The functional network architecture that is seen during task performance is a configuration of these resting-state, task-general and task-specific networks. Their findings suggest that there is a much stronger relationship between resting-state connectivity and task-evoked connectivity than generally accepted. Our current study, though focusing on task activation rather than task-evoked functional connectivity, appears to be in line with this finding and with the idea that the activation of a region is determined by the in- and output within its network, as it demonstrates that network topology during rest predicts task activation. These findings are in line with previous work investigating the predictive value of resting-state connectivity on task activation, which showed that inter-individual differences of task activity were predicted by a region's positive connectivity strength with the task network during an Eriksen Flanker task, as well as a region's negative connectivity with the default mode network (Mennes et al., 2010).

It is important to note the limitations of the group parcellation. As this parcellation is an average across participants, there is potentially some misalignment between the group parcellation and a single subject in terms of functional regions. Therefore, some of the inter-subject variability could possibly be explained by a misalignment. A replication of this study with the participants in the auditory condition of the MOUS project will give an indication of the robustness of our results.

Having established that the differences in functional organization of the language networks influences both task-based and resting-state fMRI data, a next step could be to also investigate the influence of structural connectivity on this functional network topology. It is commonly assumed that there is a strong relation (although not a one-to-one coupling) between the presence and structure of white matter fiber bundles and functional activity (for a review, see Damoiseaux & Greicius, 2009). Furthermore, it has been shown that there is no functional connectivity without an (indirect) white matter connection (Johnston et al., 2008). Yet it remains unclear how properties of the fiber bundles influence the activity. Most of the areas that stood out in the present research are regions that are connected by segments of the arcuate fasciculus (described in Catani, Jones, & ffytche, 2005) and extreme capsule (described in Saur et al., 2008). The functional connectivity strength between regions during rest and activation of regions during language processing might be closely related to properties of these pathways. Investigating this relation in more depth could give further insight in the relation between structural and functional neuroanatomy.

Additionally, a future direction and application of this research could lie in the field of imaging genetics. In imaging genetics it is assumed that an individual's genotype will have an effect on the brain's anatomy and functional activity. These effects have indeed been found on cognitive processes such as language (e.g., Pinel et al., 2012; Snijders, 2010), as well as on resting-state network topology (Glahn et al., 2010). The co-activation analysis showed that the inter-subject variability of a single region may not be the most efficient endophenotype as this variability is not unique but partly driven by an aspecific effect. Correlated variability in activation can be handled more efficiently with data reduction techniques. The correlated inter-subject variability between resting-state connectivity and task activation found in the current research points to a biologically-grounded source, and is possibly a reflection of differences in the genome. Therefore, we suggest that inter-subject variability with a shared underlying cause might be an interesting endophenotype for imaging genetics research.

5. Conclusion

In this research, we have shown that inter-subject variability in the functional organization of the language networks is present across different functional measures. The inter-subject variability in network topology during rest is in part correlated with inter-subject variablity in the activation of a language task. This consistency is mostly observed in areas that are peripherally involved in language processing. When a region shows greater connectivity to the language network during rest, it activates more strongly during a task. We conclude that network topology is predictive of task-based activation, as a portion of the inter-subject variability that is observed in task-based fMRI is caused by intrinsic differences in network topology. This type of shared inter-subject variability can potentially be very interesting for future analyses relating it to different domains, such as structural connectivity research or imaging genetics.

6. Acknowledgments

I would like show my gratitude to my supervisor Hubert Fonteijn. Thanks to his knowledge, advice and patience, I was able to carry out and finish this thesis project. I would also like to thank Julia Uddén, Annika Hultén and Peter Hagoort for allowing me to work on their data and for giving me input after every presentation. The MOUS meetings, the Neurobiology of Language meetings and meetings with individual people have been a useful source of ideas and inspiration, I thank all members of these meetings for that. Finally, I am thankful for the reviewers of the CNS Journal for their helpful comments.

7. References

Beckmann, C. F., DeLuca, M., Devlin, J. T., & Smith, S. M. (2005). Investigations into resting-state connectivity using independent component analysis. *Philosophical Transactions of the Royal Society B: Biological Sciences*, *360*(1457), 1001–1013.

Bédard, A. C., Schulz, K. P., Cook Jr., E. H., Fan, J., Clerkin, S. M., Ivanov, I., … & Newcorn, J. H. (2010). Dopamine transporter gene variation modulates activation of striatum in youth with ADHD. *NeuroImage*, *53*(3), 935–942.

Binder, J. R., Desai, R. H., Graves, W. W., & Conant, L. L. (2009). Where is the semantic system? a critical review and meta-analysis of 120 functional neuroimaging studies. *Cerebral Cortex*, *19*(12), 2767–2796.

Calhoun, V. D., Adali, T., Pearlson, G. D., & Pekar, J. J. (2001). A method for making group inferences from functional MRI data using independent component analysis. *Human Brain Mapping*, *14*(3), 140–151.

Catani, M., Jones, D. K., & Ffytche, D. H. (2005). Perisylvian language networks of the human brain. *Annals of Neurology*, *57*(1), 8–16.

Cole, M. W., Bassett, D. S., Power, J. D., Braver, T. S., & Petersen, S. E. (2014). Intrinsic and task-evoked network architectures of the human brain. *Neuron*, *83*(1), 238–251.

Cordes, D., Haughton, V., Carew, J. D., Arfanakis, K., & Maravilla, K. (2002). Hierarchical clustering to measure connectivity in fmri resting-state data. *Magnetic Resonance Imaging*, *20*(4), 305–317.

Damoiseaux, J. S., & Greicius, M. D. (2009). Greater than the sum of its parts: a review of studies combining structural connectivity and resting-state functional connectivity. *Brain Structure and Function*, *213*(6), 525–533.

Damoiseaux, J. S., Rombouts, S. A. R. B., Barkhof, F., Scheltens, P., Stam, C. J., Smith, S. M., & Beckmann, C. F. (2006). Consistent resting-state networks across healthy subjects. *Proceedings of the National Academy of Sciences*, *103*(37), 13848–13853.

Domschke, K., & Dannlowski, U. (2010). Imaging genetics of anxiety disorders. NeuroImage, *53*(3), 822–831.

Durston, S. (2010). Imaging genetics in ADHD. *NeuroImage*, *53*(3), 832–838.

Fonteijn, H. (2011). MR methods for studying the modularity and connectivity of the human brain. On the parcellation of resting-state fMRI data: within-subject consistency and determining the number of clusters (Doctoral dissertation). Retrieved from: dspace.library.uu.nl.

Glahn, D. C., Winkler, A. M., Kochunov, P., Almasy, L., Duggirala, R., Carless, M. A., … & Blangerod, J. (2010). Genetic control over the resting brain. *Proceedings of the National Academy of Sciences*, *107*(3), 1223–1228.

Goldberg, T. E., & Weinberger, D. R. (2004). Genes and the parsing of cognitive processes. *Trends in Cognitive Sciences*, *8*(7), 325–335.

Hagoort, P. (2005). On Broca, brain, and binding: a new framework. *Trends in Cognitive Sciences*, *9*(9), 416–423.

Johnston, J. M., Vaishnavi, S. N., Smyth, M. D., Zhang, D., He, B. J., Zempel, J. M., … & Raichle, M. E. (2008). Loss of resting interhemispheric functional connectivity after complete section of the corpus callosum. *Journal of Neuroscience*, *28*(25), 6453–6458.

Liu, H., Qin, W., Li, W., Fan, L., Wang, J., Jiang, T., & Yu, C. (2013). Connectivity-based parcellation of the human frontal pole with diffusion tensor imaging. *Journal of Neuroscience*, *33*(16), 6782–6790.

Mennes, M., Kelly, C., Zuo, X.-N., Di Martino, A., Biswal, B. B., Castellanos, F. X., & Milham, M. P. (2010). Inter-individual differences in resting-state functional connectivity predict task-induced bold activity. *NeuroImage*, *50*(4), 1690–1701.

Mueller, S., Wang, D., Fox, M. D., Yeo, B. T., Sepulcre, J., Sabuncu, M. R., … & Liu, H. (2013). Individual variability in functional connectivity architecture of the human brain. *Neuron*, *77*(3), 586–595.

Murphy, K., Birn, R. M., Handwerker, D. A., Jones, T. B., & Bandettini, P. A. (2009). The impact of global signal regression on resting state correlations: are anti-correlated networks introduced? *NeuroImage*, *44*(3), 893–905.

Pinel, P., Fauchereau, F., Moreno, A., Barbot, A., Lathrop, M., Zelenika, D., … & Dehaene, S. (2012). Genetic variants of FOXP2 and KIAA0319/TTRAP/THEM2 locus are associated with altered brain activation in distinct language-related regions. *Journal of Neuroscience*, *32*(3), 817–825.

Potkin, S. G., Turner, J. A., Fallon, J. A., Lakatos, A., Keator, D. B., Guffanti, G., & Macciardi, F. (2008). Gene discovery through imaging genetics: identification of two novel genes associated with schizophrenia. *Molecular Psychiatry*, *14*(4), 416–428.

Power, J. D., Cohen, A. L., Nelson, S. M., Wig, G. S., Barnes, K. A., Church, J. A., … & Petersen, S. E. (2011). Functional network organization of the human brain. *Neuron*, *72*(4), 665–678.

Saur, D., Kreher, B. W., Schnell, S., Kmmerer, D., Kellmeyer, P., Vry, M.-S., … & Weiller, C. (2008). Ventral and dorsal pathways for language. *Proceedings of the National Academy of Sciences*, *105*(46), 18035–18040.

Shi, J., & Malik, J. (2000). Normalized cuts and image segmentation. *IEEE Transactions on Pattern Analysis and Machine Intelligence*, *22*(8), 888–905.

Smith, S. M., Fox, P. T., Millera, K. L., Glahn, D. C., Fox, P. M., Mackay, C. E., … & Beckmann, C. F. (2009). Correspondence of the brain's functional architecture during activation and rest. *Proceedings of the National Academy of Sciences*, *106*(31), 13040–13045.

Snijders, T. (2010). More than words: Neural and genetic dynamics of syntactic unification. Effects of a common CNTNAP2 polymorphism on functional and structural brain measures related to language processing (Doctoral dissertation). Retrieved from: repository.ubn.ru.nl.

Snijders, T., Petersson, K., & Hagoort, P. (2010). Effective connectivity of cortical and subcortical regions during unification of sentence structure. *NeuroImage*, *52*(4), 1633–1644.

Van den Heuvel, M., Mandl, R., & Hulshoff Pol, H. (2008). Normalized cut group clustering of resting-state fMRI data. *Public Library of Science one*, *3*(4), e2001.

Van den Heuvel, M. P., & Hulshoff Pol, H. E. (2010). Exploring the brain network: a review on resting-state fmri functional connectivity. European *Neuropsychopharmacology*, *20*(8), 519–534.

Xiang, H. D., Fonteijn, H. M., Norris, D. G., & Hagoort, P. (2010). Topographical functional connectivity pattern in the perisylvian language networks. *Cerebral Cortex*, *20*(3), 549–560.

Molecular Characterization of FOXP2 in Neurodevelopment and Disorder

Swathi Mookonda Chinnappa[1]
Supervisor: Sarah A. Graham[1]

[1]*Max Planck Institute for Psycholinguistics, Nijmegen, The Netherlands.*

Forkhead box protein P2 (*FOXP2*) was the first gene to be implicated in language. Although several mutations have been reported in this gene in patients with language and other neurodevelopmental disorders, only a few of these have been functionally characterized. Here, we report the first characterization of the N597H, Q390VfsX5 and P416T mutations, in addition to further characterizing the R553H, Q17L, R328X and M406T mutations. We show that the Q390VfsX5 mutation has a severe effect on protein function, supporting the pathological role of this mutation. In addition, we find that the N597H mutation retains functional properties of wild-type FOXP2, suggesting that this mutation does not underlie the patient phenotype as has been suggested. We also investigated the molecular consequences of human-specific amino acid changes in FOXP2 and provide novel molecular characterization on FOXP2 isoforms and paralogs.

Keywords: FOXP2, language, speech, neurodevelopment, gene regulation, transcription factor, protein-protein interactions, mutation

Corresponding author: Swathi M. Chinnappa; **E-mail**: swathimc@student.ru.nl

1. Introduction

In comparison to other species where vocal communication is restricted to a small collection of calls and vocalizations, humans have a wide repertoire of sound combinations that provide us with the ability to develop a more complex language system. There are several different aspects to language including phonology, semantics, syntax and pragmatics, all of which have a cognitive basis. Incredibly, humans acquire this ability without conscious effort. It is therefore not surprising that language in humans is also thought to have a complex genetic basis. However, we still do not have a complete understanding of the genes or the gene networks that underlie language development and the search for possible language-related genes still continues.

A crucial step in understanding the biological basis of language is to investigate language impairment. Several types of language impairment have been reported including dyslexia, specific language impairment and speech sound disorders. Dyslexia is a developmental disorder characterized by difficulty in reading fluently and accurately. Specific language impairment (SLI) is an impairment that is, as the name suggests, specific to language development that cannot be attributed to other developmental factors such as autism or general slow development, while speech sound disorders are characterized by the inability to correctly produce word sounds. While research in cognitive neuroscience could tell us much about the brain morphology and behavioural phenotypes in language impairments, study of language impairments that run in families acts as the perfect entry point into the genetic basis of language. For example, studies have implicated the *DYX1C1*, *KIA0319* and *DCDC2* genes in dyslexia while *CMIP* and *ATP2C2* have been shown to play a role in SLI (Carrion-Castillo, Franke, & Fisher, 2013; Newbury et al., 2009). Such studies could in turn lead to objective and standardized tests for diagnosing and treating language-related disorders. Currently, diagnosis is based on psychometric tests which do not give an absolute distinction between normal and abnormal performance, and the cause of disorders is unexplained, which limits treatment options.

In this regard, the first gene to be associated with language and speech is *FOXP2* (Forkhead box protein P2). It was first discovered in reference to a monogenic form of language impairment identified in a large pedigree in the UK (the KE family) (Lai, Fisher, Hurst, Vargha-Khadem, & Monaco, 2001). The affected family members all show impairment in learning and producing the complex orofacial movements required to produce speech. The impairment is consistent with a diagnosis of childhood apraxia of speech (CAS), also known as developmental verbal dyspraxia (DVD). Those carrying the mutation also show impairment in receptive and expressive language (affecting both speech and reading/writing) but do not show impairment in other cognitive areas, barring some lowering in IQ. There is, therefore, a link between the mutation within this gene and the above mentioned language impairments while leaving other cognitive abilities relatively intact. Other *FOXP2* mutations have been subsequently reported, including point mutations, deletions and translocations (Bacon & Rappold, 2012).

FOXP2 codes for a transcription factor that belongs to the FOX class of proteins. Transcription factors play a crucial role in regulating the expression of genes in a cell. They have the ability to both turn on and off genes as well as fine-tune their expression. Precise regulation of gene expression is vital to guide development and to establish differentiated tissues such as different subtypes of neurons, and also to respond to environmental signals, including establishing learning and memory in response to neuronal firing.

FOX proteins are transcription factors that all contain a forkhead box domain which is the DNA binding domain. There are 50 FOX proteins in humans. They are expressed in a variety of tissues and play crucial roles in embryogenesis, with several having been implicated in genetic disorders (Bacon & Rappold, 2012). FOXP2 belongs to the FOX subfamily of FOX proteins which also includes FOXP1, FOXP3 and FOXP4. FOXP1, FOXP2 and FOXP4 are expressed in the brain and other tissues, while FOXP3 is expressed in hematopoietic cells. FOXP2 is highly expressed in brain and lung tissue. In the brain, it is expressed during neuronal differentiation and in neurons of different thalamic nuclei, striatal medium spiny neurons, projection neurons of cortical layers VI and V, and in V1 interneurons in ventral spinal cord (Campbell, Reep, Stoll, Ophir, & Steven, 2010; Ferland, Cherry, Preware, Morrisey, & Walsh, 2003; Hisaoka, Nakamura, Senba, & Morikawa, 2010; Reimers-Kipping, Hevers, Pääbo, & Enard, 2011).

The FOXP2 protein contains several domains; two polyglutamine regions, each containing a stretch of the amino acid glutamine (one of 40 glutamines and another, eight residues away, of 10

glutamines) (Bruce & Margolis, 2002), a zinc finger domain, a leucine zipper domain that plays a role in dimerisation (Li, Weidenfeld, & Morrisey, 2004) and the forkhead DNA binding domain. The DNA binding domain has been determined (Stroud 2006) while other regions require further research. *FOXP2* is a highly conserved gene between vertebrate species, with only three amino acid substitutions between the mouse and human orthologs. Notably, two of these changes occurred in the human lineage after the split with chimpanzees. The leucine zipper, zinc finger or the DNA binding FOX domain are particularly well conserved and none of these amino acid changes are observed in these domains.

In addition, mice that are homozygous for the mutation found in the KE family show severe developmental delays and die within four weeks of birth. Mice that are heterozygous for the non-functional allele show subtle phenotypic changes in organs other than the brain (Enard et al., 2009). They have also been shown to have impaired motor skill learning as assessed by the running wheel and accelerated rotarod behavioural tests. In addition, synaptic plasticity is also affected in the Purkinje cells of the cerebellum and spiny neurons of the basal ganglia (Groszer et al., 2010).

An important step in elucidating the function of FOXP2 and its role in the aetiology of speech impairment is investigating potential FOXP2 targets, their role in the brain and the effect of FOXP2 on the expression of these genes. Chromatin Immunoprecipitation (ChIP) studies, that enable us to identify genes to which a protein binds, have identified potential targets of FOXP2, some of which have been further characterized. This includes the *CNTNAP2* gene as well as *SRPX2*, both of which are involved in neurite outgrowth and synapse formation (Sia, Clem, & Huganir, 2013; Vernes et al., 2009). This is the first step in working towards elucidating the role of FOXP2 in the context of brain function. Although hundreds of potential FOXP2 targets have been identified in these studies, it is still not known which targets are important for the development of language-related brain circuits.

The mutation in the KE family gave us invaluable insight into one of possibly thousands of genes that impact language. Further investigations into FOXP2 function will help us gain a better understanding of how the protein functions and what impact it has on the brain. In this respect, characterizing FOXP2, especially its mutated forms, will help in unravelling the overall network in which it plays a role. We aim to develop a battery of assays that can be used to assess *FOXP2* mutations and also characterize four recent mutations. In addition to the four recent mutations, the battery of assays was used to assess in two close relatives of *FOXP2* (*FOXP1* and *FOXP4*), *FOXP2* isoforms, human specific changes in *FOXP2* and other *FOXP2* patient mutations have been reported. This set of assays would assist in identifying the role of a *FOXP2* mutation in a given disorder leading to a better understanding of the link between the protein and the phenotype. In addition, not all disorders involving mutations in the *FOXP2* gene have FOXP2 dysfunction as the causative factor. These assays could be used, therefore, to avoid misdiagnosis of a disorder as being related to the *FOXP2* gene and protein.

2. Results

2.1 Characterization of FOXP proteins involved in neurodevelopment

FOXP1 and FOXP4 are close relatives of FOXP2 that also show overlapping patterns of expression in the developing brain. The identity of amino acids between FOXP1/FOXP2 is 64%, and between FOXP2/FOXP4 and FOXP1/FOXP4 is 56%. These proteins have a very high level of conservation in the leucine zipper, zinc finger, DNA binding domains and the region flanking the poly-glutamine region while there is a lower level of conservation elsewhere in the protein. A major difference between the FOXP proteins is that only FOXP2 has a polyglutamine tract (Fig. 1A). Given the high level of similarity between FOXP1, FOXP2 and FOXP4, we thought it relevant to characterize these proteins as well. This would highlight the differences and similarities between these FOX proteins and help us to gain a better understanding of the connection between the structure of the protein and its functioning.

YFP (yellow fluorescent protein) and mCherry are fluorescent proteins that can be used as tags for other proteins. Therefore, proteins tagged with YFP and mCherry can be visualized under fluorescence. This allows us to not only check for expression of the proteins but also to assess intracellular localization. FOXP1, FOXP2 and FOXP4 constructs tagged with YFP were previously generated in this research group. To verify protein expression from these constructs, HEK293 (human embryonic kidney) cells were transfected with these constructs and whole cell lysates were used to analyze protein expression using western blotting (Fig. 1B). All three proteins were found to run just above 100kDa on the blot

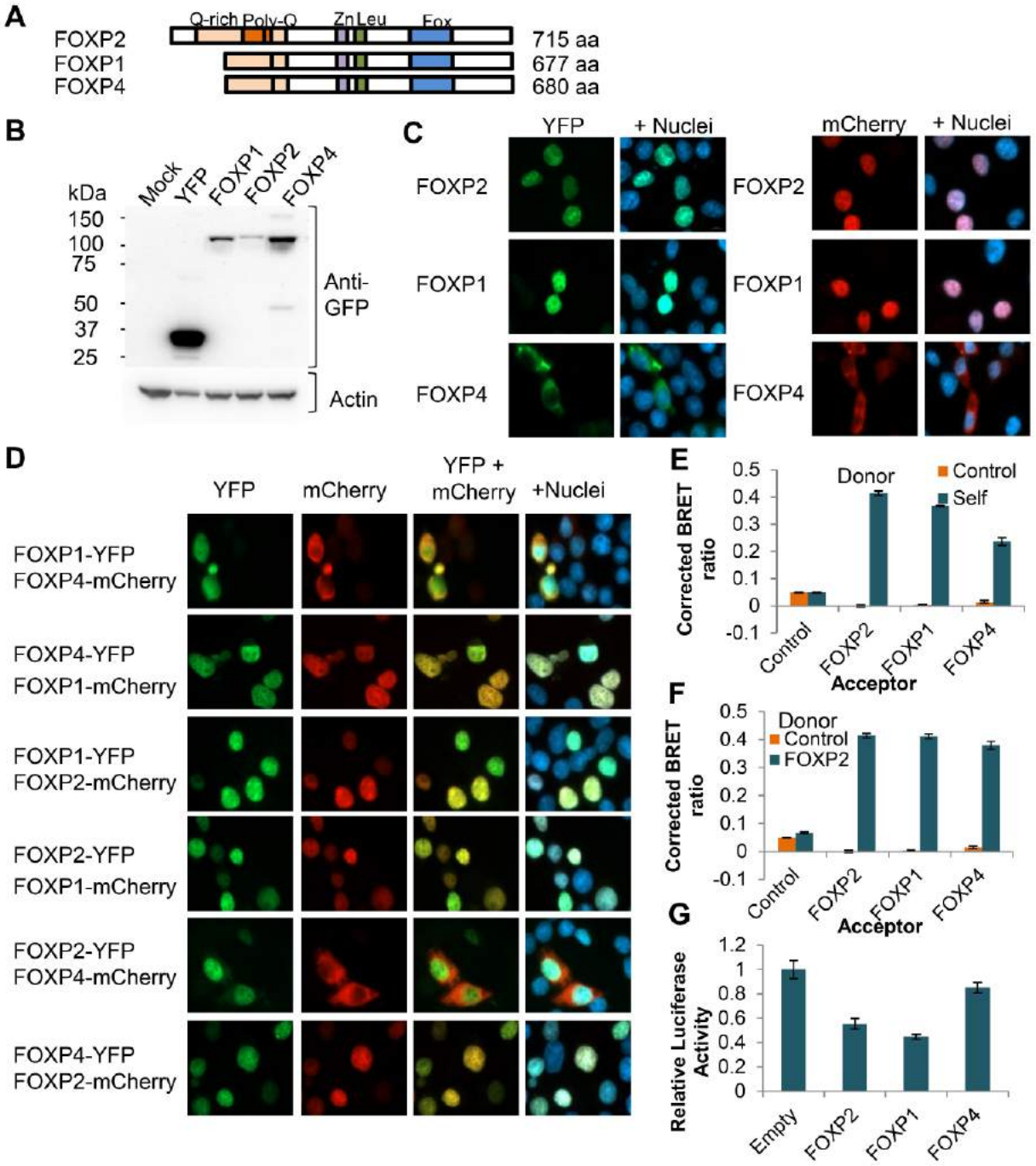

Fig. 1. Characterization of FOXP1, FOXP2 and FOXP4. **A.** Schematic representation of FOXP1, FOXP2 and FOXP4 showing the glutamine-rich region (Q-rich, pale orange), polyglutamine tract (Poly-Q, dark orange), the zinc finger (Zn, purple), leucine zipper (Leu, green) and the DNA binding domain (FOX, blue). **B.** Western blot of whole cell lysates of HEK293 cells transfected with YFP-tagged FOXP1, FOXP2 and FOXP4 or a mock transfection with no plasmid. The protein was detected using anti-GFP antibody. **C.** Fluorescence microscopy images of FOXP1, FOXP2 and FOXP4 fused to YFP (green) or mCherry (red). **D.** Fluorescence microscopy images of YFP and mCherry-tagged FOXP1, FOXP2 and FOXP4 co-transfected in all combinations. **E.** BRET assay to assess homodimerization of FOXP1, FOXP2 and FOXP4. **F.** BRET assay to assess heterodimerization of FOXP2 with FOXP1 and FOXP4. **G.** Luciferase assay to assess the regulation of the SV40 promoter by FOXP1, FOXP2 and FOXP4 YFP-fusion proteins. In E, F and G, the plotted values are means of biological triplicates from one representative experiment and the error bars represent standard deviation.

consistent with their theoretical weights. The results also indicate that expression of FOXP2 is low in comparison to FOXP1 and FOXP4. This difference in expression could be a result of the difference in protein structure as both the FOXP1 and FOXP4 proteins lack the poly-glutamine region. All of the proteins show dramatically lower expression than YFP alone, suggesting that the expression level of

these proteins is limited by signals in the mRNA or protein.

Fluorescence images of HEK293 cells transfected with YFP- and mCherry-tagged FOXP1, FOXP2 and FOXP4 constructs show that both FOXP1 and FOXP2 are nuclear, which is to be expected since they both contain the nuclear localization signals flanking the DNA binding domain (Fig. 1C). Surprisingly, FOXP4 is found to be cytoplasmic even though it still contains the nuclear localization signals. The expression patterns were found to be the same with the YFP and mCherry constructs validating this method of protein expression. The difference in localization could play a role, not only in protein function, but also in potential interactors.

In addition, HEK293 cells were co-transfected with FOXP1, FOXP2 and FOXP4 in YFP and mCherry in different combinations to assess intracellular localization of these proteins when expressed together (Fig. 1D). When FOXP1 and FOXP2 were co-transfected, one tagged with YFP and mCherry and vice versa, both proteins retain their nuclear localization with perfectly overlapping expression pattern. FOXP4, however, shows cytoplasmic localization in co-transfections of FOXP4-mCherry and FOXP2-YFP and nuclear in co-transfections of FOXP4-YFP and FOXP2-mCherry. Further experiments are needed to understand the interaction.

Furthermore, FOXP1, FOXP2 and FOXP4 have been shown to form homo- and heterodimers in co-immunoprecipitation assays (Li et al., 2004). The dimerization could also play a role in proper functioning of the proteins. We used a Bioluminescence Resonance Energy Transfer (BRET) assay developed in this research group to assess this interaction in live cells (Deriziotis, Graham, Estruch, & Fisher, 2014) . In the BRET assay, the two proteins thought to be interacting, are each tagged either with Renilla luciferase or YFP. Upon addition of the luciferase substrate, the luciferase in the cells is activated, leading to luminescence at 470nm wavelength. If the two proteins do interact, it brings the luciferase in close proximity to the YFP, resulting in energy transfer from the luciferase to the YFP. The Renilla luciferase tagged protein therefore acts as the donor while the YFP tagged protein acts as the acceptor. This transfer results in a change in frequency of the emitted light, from 470nm to a 530nm. This can be measured using a luminometer. A ratio is calculated for the YFP emission value relative to the Renilla luciferase emission value. A higher BRET ratio compared to a control condition in which the luciferase or YFP is not fused to another protein, therefore, indicates an interaction between the two proteins.

FOXP1, FOXP2 and FOXP4 all showed a high BRET ratio when assessing interaction during homo- and heterodimerization indicating that they all form both homo- and heterodimers (Fig. 1E and 1F). This shows that the interaction observed in co-immunoprecipitation assays also occurs in live cells and emphasizes that FOXP1, FOXP2 and FOXP4 could form heterodimers that have different effects on gene regulation (Sin, Li, & Crawford, 2014). The interaction also explains why co-expression of FOXP4 with FOXP2 or FOXP1 alters the subcellular localization of these proteins. Alterations of subcellular localization due to heterodimerization could also be a mechanism for regulating gene expression by FOXP proteins.

To assess the ability of FOXP proteins to regulate transcription we used a luciferase reporter assay. In a luciferase reporter assay, a construct for expression of a transcription factor is co-transfected in cells with a vector containing a firefly luciferase reporter gene under the control of a promoter that contains a binding site for the transcription factor. Cells are also transfected with a normalizer plasmid such as the Renilla luciferase in order to control for factors other than protein activity, such as transfection efficiency and cell number. Upon addition of the luciferase substrate, the luciferase is activated and this activity can be measure using a luminometer. The measured value is then normalized to the Renilla luciferase value. Using this technique, we assessed the regulation of the SV40 viral promoter by the FOXP proteins. Both FOXP1 and FOXP2 repressed the SV40 promoter consistent with previous results, demonstrating that the YFP-fusion proteins retain DNA-binding activity (Fig. 1G). In comparison, FOXP4 did not repress the promoter to the same extent. This could be a result of the cytoplasmic localization of FOXP4.

Finally, we assessed the interaction of FOXP proteins with C-terminal binding proteins. C-terminal Binding Protein 1 (CtBP1) acts as a corepressor for several transcription factors. It was identified as an interactor of the full length FOXP2 protein in an adult rat lung yeast two-hybrid screen with a part of FOXP2 as the bait (Li et al., 2004) and in an independent yeast two-hybrid screen which also identified the CtBP1 paralog CtBP2 as a FOXP2 interaction partner (Sakai et al., 2011). The interaction between FOXP2 and CtBP1 has also been validated by co-immunoprecipitation (Li et al., 2004). Transfection of HEK293 cells with CtBP1 and CtBP2 fused to either YFP or mCherry

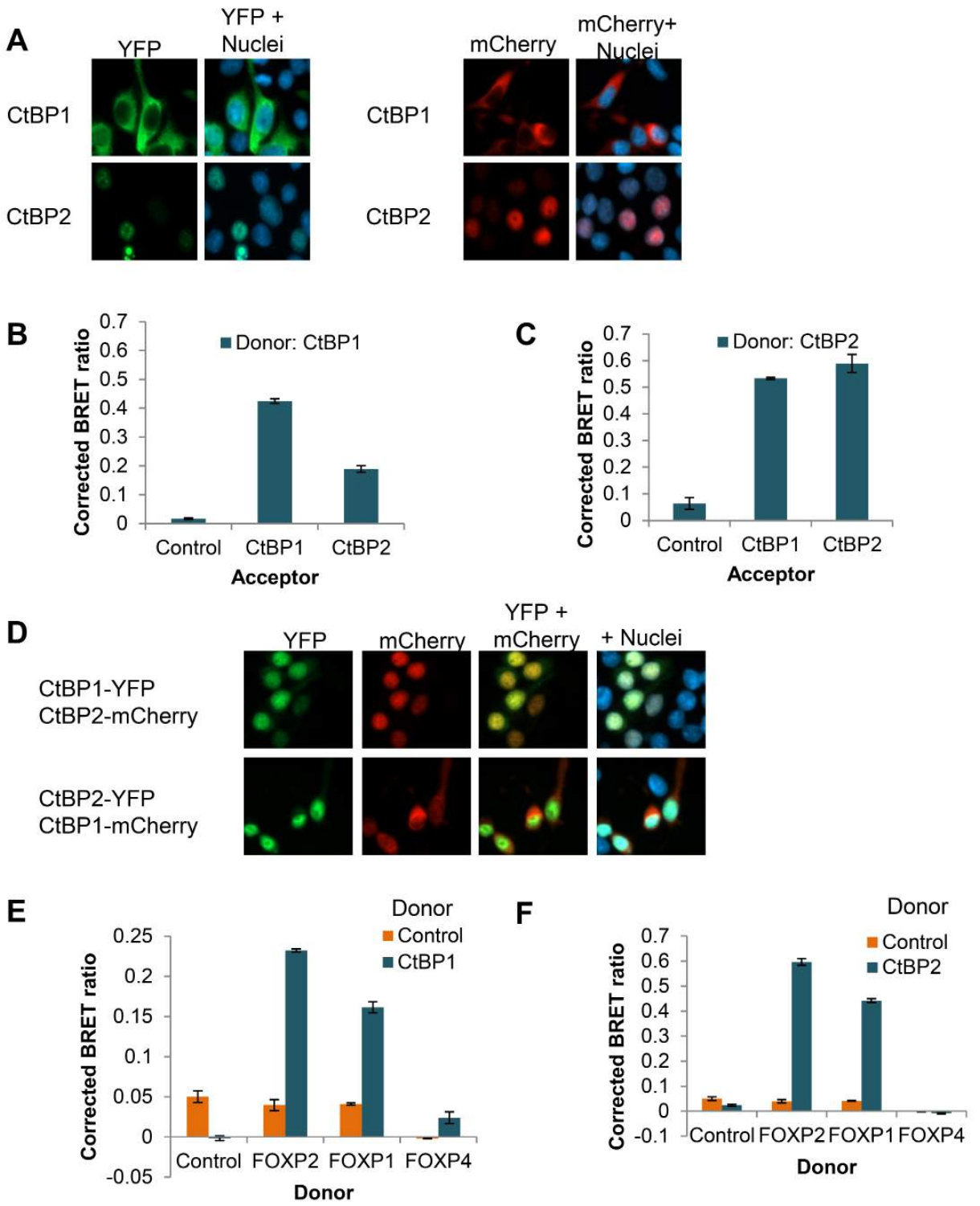

Fig. 2. Interaction of FOXP1, FOXP2 and FOXP4 with CtBP proteins. **A.** Fluorescence microscopy images of HEK293 cells transfected with CtBP1 and CtBP2 tagged with YFP (in green) or mCherry (in red). **B.** BRET assay to assess homo- and heterodimerization of CtBP1 and CtBP2 with CtBP1 as the donor Renilla luciferase fusion protein. **C.** BRET assay to assess homo- and heterodimerization of CtBP1 and CtBP2 with CtBP2 as the donor Renilla luciferase fusion protein. **D.** Fluorescence microscopy images of HEK293 cells co-transfected with CtBP1 and CtBP2 fused to YFP (green) and mCherry (red). **E.** BRET assay to assess the interaction of FOXP1, FOXP2 and FOXP4 with CtBP1. **F.** BRET assay to assess the interaction the interaction of FOXP1, FOXP2 and FOXP4 with CtBP2. In B, C, E and F, the plotted values are means of biological triplicates from one representative experiment and the error bars represent standard deviation.

showed that CtBP1 is predominantly cytoplasmic with some nuclear expression, whereas CtBP2 is nuclear (Fig. 2A). BRET assays showed that CtBP1 and CtBP2 form homo- and heterodimers, as has recently been reported (Madison, Wirz, Siess, & Lundblad, 2013) (Fig. 2B, 2C). Consistent with this

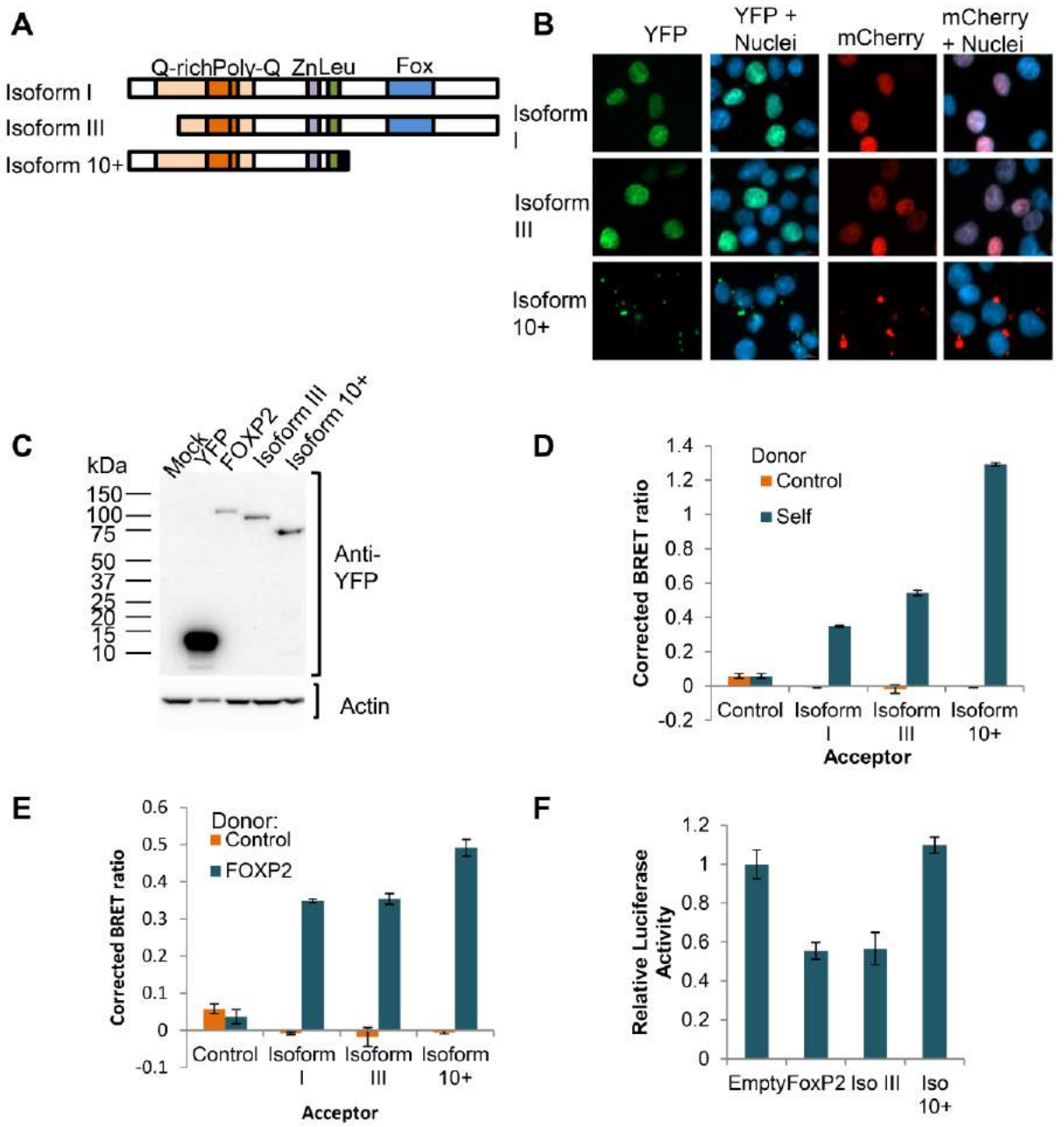

Fig. 3. Characterization of FOXP2 isoforms. **A.** Schematic representation of FOXP2 isoforms I, III and 10+ showing the glutamine-rich region (Q-rich, pale orange), polyglutamine tract (Poly-Q, dark orange), the zinc finger (Zn, purple), leucine zipper (Leu, green) and the DNA binding domain (FOX, blue). **B.** Fluorescence microscopy images of HEK293 cells transfected with FOXP2 isoforms fused to YFP (green, left panels) or mCherry (red, right panels). **C.** Western blot analysis of whole cell lysates of HEK293 cells transfected with YFP-fusion proteins. Mock transfection contained no plasmid. D BRET assay to assess homodimerization of the FOXP2 isoforms in HEK293 cells. **E.** BRET assay to assess the interaction of FOXP2 isoforms with full-length FOXP2. **F.** Luciferase assay to assess regulation of the SV40 promoter by FOXP2 isoforms. In D, E and F, the plotted values are means of biological triplicates from one representative experiment and the error bars represent standard deviation.

interaction, cotransfection of CtBP1 and CtBP2 caused increased nuclear localization of CtBP1 and decreased nuclear localization of CtBP2 (Fig. 2D).

We used the BRET assay to assess the interaction of CtBP1 and CtBP2 with FOXP1, FOXP2 and FOXP4 (Fig. 2E, 2F). Cells were transfected with FOXP proteins fused to Renilla luciferase and CtBP proteins fused to YFP. Consistent with previous report (Li et al., 2004), full length FOXP2 and FOXP1 were found to interact with CtBP1. FOXP4 shows a BRET ratio much lower than that of FOXP1 and FOXP2, indicating little or no interaction with CtBP1, despite the fact that both FOXP4 and CtBP1 are cytoplasmic and therefore have a greater overlap in the cell than FOXP1/2 and CtBP1. We also demonstrated that FOXP1 and FOXP2 interact with CtBP2, validating the yeast two-hybrid assay finding (Fig. 2F). BRET assays were also done

with CtBP1 fused to Renilla luciferase and FOXP2 proteins fused to YFP, but the assay did not work in this configuration, which is not unusual for this type of assay. The interaction between FOXP proteins and CtBP1 and CtBP2 may play an important role in the transcriptional activity of FOXP proteins. This interaction also acts as a possible starting point to investigate other FOXP interactors that together form a transcription regulatory complex. We also see that CtBP1 and CtBP2 both form homo- and heterodimers as assessed in a BRET assay. This is consistent with previous results that have reported CtBP1 to form a dimer of dimers (Madison et al., 2013).

2.2 Characterization of FOXP2 isoforms

There are three isoforms of FOXP2, produced by alternative splicing, namely isoform I (full length), isoform III and isoform 10+ (Fig. 3A). Isoform 10+ is truncated after the leucine zipper. The isoform, therefore, lacks the DNA binding forkhead box domain. Isoform III is truncated by 92 amino acids at the N-terminus but still contains the functional domains found in full length FOXP2, namely the poly-glutamine region, zinc finger, leucine zipper and the FOX domain.

A previous study assessed the localization of these isoforms by transfecting cells with constructs for expression of the isoforms with an N-terminal epitope tag (Xpress tag) and staining the cells using anti-Xpress antibody (Vernes et al., 2006). In these experiments, Isoforms I and III showed nuclear localization, while isoform 10+ formed aggregates in the cytoplasm. Here, constructs for expression of FOXP2 isoforms fused to YFP and mCherry, generated previously by this research group, were transfected into HEK293 cells for fluorescence imaging (Fig. 3B). Our results, utilizing the YFP and mCherry fusion constructs, are consistent with the results from Vernes et al. Isoform III shows nuclear localization identical to full-length isoform I, whereas isoform 10+ forms cytoplasmic aggregates. This validates the use of YFP and mCherry fusion constructs for studying localization of FOXP2 variants. In addition, the localization of all three proteins was found to be the same with both YFP and mCherry constructs, indicating that the fusion itself does not impact localization.

Western blot analysis verified that the correct YFP fusion proteins are expressed in HEK293 cells (Fig. 3C). The theoretical size of YFP fusions of FOXP2 isoforms are: full length, 104 kDa, isoform III, 95 kDa, and isoform 10+, 74 kDa. Consistent with these values, the full length protein is seen to run just above the 100 kDa mark on the blot; isoform III is seen at close to a 100 kDa and isoform 10+ is seen at about 70 kDa.

Since full-length FOXP2 is known to form homodimers, (Li et al., 2004) we assessed the homo- and heterodimerization of FOXP2 isoforms using the BRET assay. We show here, that isoform III and isoform 10+ also form homodimers, which is the expected result, as they both still retain the leucine zipper domain (Fig. 3D). The higher BRET signal with isoform 10+ is most likely due to increased protein concentration in the aggregates. In addition, full length FOXP2 was found to interact with isoform III and isoform 10+ (Fig. 3E). Dimerization of FOXP2 isoforms could play a role in the regulatory role of the proteins. Although isoform 10+ cannot bind to DNA, it still contains the leucine zipper and is therefore capable of dimerizing with both itself and with the full length protein. Therefore the isoform may exert its effect by retaining full length FOXP2 in the aggregates or being transported into the nucleus due to this interaction. This could be tested by co-transfecting the isoform 10+ and the full length FOXP2 constructs used here.

The activity of the FOXP2 isoforms in regulating transcription has been assessed previously using the SV40 assay (Vernes et al., 2006). Previous results have shown that isoform III represses the SV40 promoter to a similar fold as the full length protein. While isoform 10+ also shows some degree of repression, it is not as much as the full length protein despite the fact that this isoform is unable to bind DNA. Our results also show repression of transcription by isoform I and isoform III. However, we do not see any repression with isoform 10+, which is expected as it lacks the DNA binding domain. Future experiments could involve co-transfecting the full length and isoform 10+ FOXP2 proteins to see if dimerization with 10+ reduces ability of the full length protein to repress transcription.

In addition, we assessed interaction of the FOXP2 isoforms with CtBP1 and CtBP2 (Fig. 4). Co-transfections of the FOXP2 isoforms fused to YFP with CtBP1 fused to mCherry show that there is some degree of co-localization in the nucleus with the full length and isoform III (Fig. 4A). With isoform 10+, co-localization can be seen in aggregates in the cytoplasm. When CtBP1 is transfected alone, no aggregates are observed. This indicates that the aggregates seen when co-transfected with isoform 10+ is a result of interaction between the two proteins. Therefore, it presumably interacts with full length FOXP2 and isoform III in the nucleus

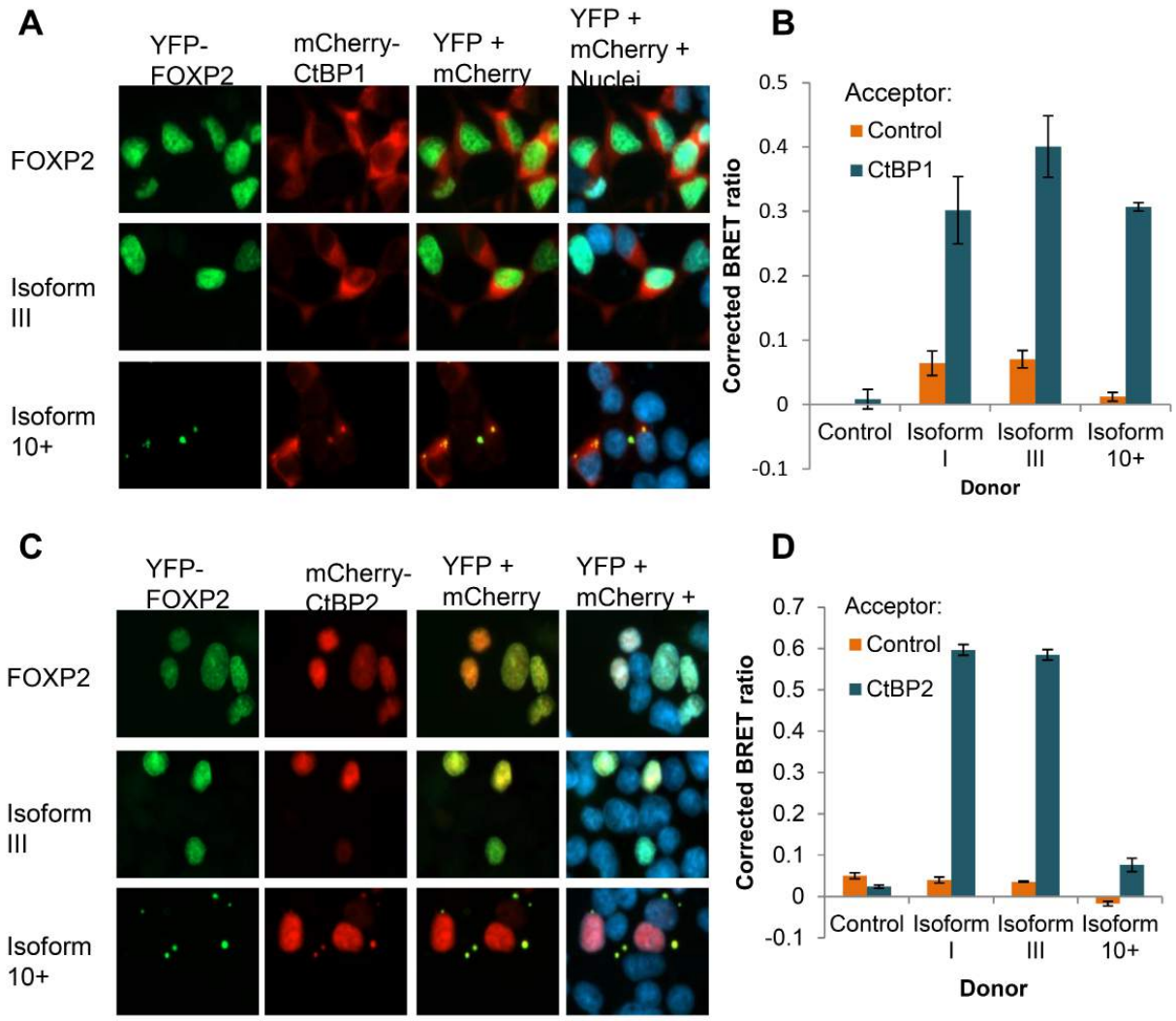

Fig. 4. Interaction of FOXP2 isoforms with CtBP proteins. **A.** Fluorescence microscopy images of FOXP2 isoforms fused to YFP (green) co-transfected with CtBP1 fused to mCherry (red) in HEK293 cells. **B.** BRET assay to assess the interaction between FOXP2 isoforms and CtBP1. **C.** Fluorescence microscopy images of FOXP2 isoforms fused to YFP (green) co-transfected with CtBP2 fused to mCherry (red) in HEK293 cells. **D.** BRET assay to assess the interaction between FOXP2 isoforms and CtBP2. In B and D, the plotted values are means of biological triplicates from one representative experiment and the error bars represent standard deviation.

and with isoform 10+ in the cytoplasmic aggregates. Consistent with the co-localization of FOXP2 isoforms and CtBP1, BRET assays using FOXP2 isoforms fused to Renilla luciferase and CtBP1 fused to YFP showed that all three isoforms can interact with CtBP1 (Fig. 4B). This shows that the CtBP1 binding site is within the N-terminal region of FOXP2 that is retained in isoform 10+.

Co-transfections of the FOXP2 isoforms fused to YFP with CtBP2 fused to mCherry also showed co-localization, including co-localization of CtBP2 with isoform 10+ in cytoplasmic aggregates that is suggestive of an interaction between these proteins (Fig. 4C). In a BRET assay with FOXP2 isoforms fused to Renilla luciferase and CtBP2 fused to YFP, there is clear interaction between CtBP2 and full length FOXP2 and isoform III, but not with isoform 10+, despite the co-localization seen in fluorescence images of co-transfection. This may be because only a very small proportion of isoform 10+ protein is associated with CtBP2 because most CtBP2 protein is located in the nucleus.

2.3 Characterization of human-specific amino acid changes in FOXP2

FOXP2 is a highly conserved protein with only a few amino acid changes between the mouse, chimp and human variants (Fig. 5A). The FOXP2 protein found in chimps differs in only two amino acids – N303T and S325N and an additional glutamine in the polyglutamine region. The mouse variant also differs from the human variants in a third amino acid substitution in addition to those found in the

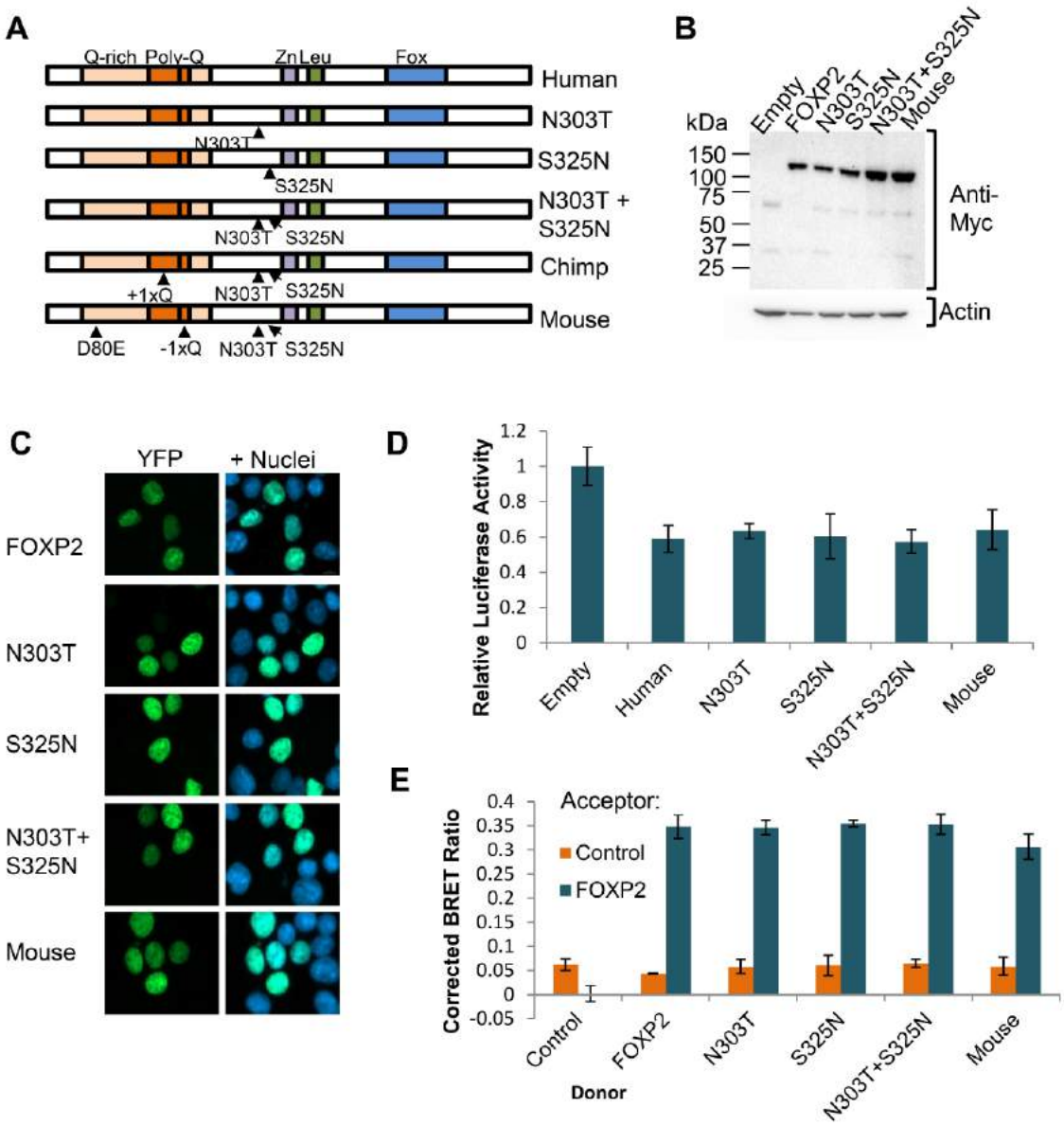

Fig. 5. Characterization of FOXP2 species variants. **A.** Schematic representation of FOXP2 species variants showing the glutamine-rich region (Q-rich, pale orange), polyglutamine tract (Poly-Q, dark orange), the zinc finger (Zn, purple), leucine zipper (Leu, green) and the DNA binding domain (FOX, blue). The variants labelled N303T, S325N and N303T+S325N are synthetic variants created by mutagenesis of human *FOXP2* to revert the amino acids at these positions to the ancestral ones found in the chimpanzee protein. **B.** Western blot analysis of whole cell lysates of HEK293 cells transfected with Myc-tagged human FOXP2, or the N303T, S325N, N303T+S325N or mouse Foxp2 variants. Proteins were detected using an anti-Myc antibody. **C.** Fluorescence microscopyimages of HEK293 cells transfected with YFP-tagged FOXP2 variants. **D.** Luciferase assay to assess regulation of SV40 promoter by YFP-tagged species variants of FOXP2. **E.** BRET assay to assess dimerization of the species variants of FOXP2 with the human FOXP2 protein. In D and E, the plotted values are means of biological triplicates from one representative experiment and the error bars represent standard deviation.

chimp variant. This variant also lacks a glutamine residue in the polyglutamine region. It is interesting that two recent amino acid changes have occurred since the split between humans and chimpanzees because these changes could be hypothesized to relate to the evolution of language in our species. Experiments with transgenic mice have shown that the human specific changes have effects on neurons, but the mechanism for these effects is unknown. It is therefore useful to compare the different amino acid changes found in the protein as it allows us to assess if these mutations themselves greatly impact protein function or if other factors may be at play.

Here, we investigate constructs with the N303T and the S325N amino acid changes separately and together, as well as the mouse variant. Constructs for expression of these FOXP2 variants with an N-terminal Myc epitope tag have been previously

Table 1. Mutations in FOXP2 found in patients with neurodevelopmental disorders.

Mutation	Phenotype	Inheritance	References
R553H	CAS; receptive and expressive language deficits; bilateral loss of gray matter and reduced volume in caudate nucleus.	Autosomal dominant, co-segregates with phenotype	Vargha-Khadem et al., (1998); Fisher et al., (1998); Lai et al. (2001), Liegeois et al., (2003)
Q17L	Speech articulation problem	Not determined. Not present in affected sibling.	MacDermot et al. (2005)
R328X	Developmental delays in speech and language; impaired expressive; receptive language	Autosomal dominant, co-segregates with phenotype	MacDermot et al. (2005)
M406T	Focal epilepsy with CSWS, clinical phenotype not fully assessed	Inherited, does not co-segregate with phenotype	Roll et al. (2010)
N597H	CAS	Not determined	Laffin et al. (2012)
Q390VfsX5	CAS; dysarthria; severely impaired receptive; expressive language skills	*De novo*	Turner et al. (2013)
P416T	Neonatal feeding difficulties; delayed milestones; moderate to severe stuttering.	Inherited, does not co-segregate with phenotype	Turner et al. (2013)

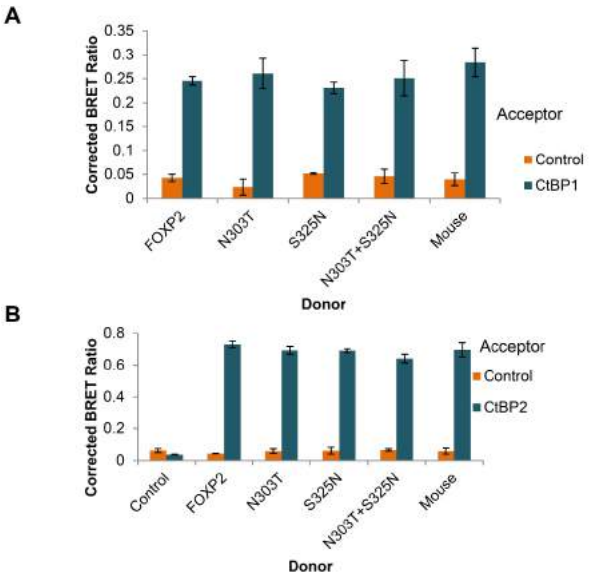

Fig. 6. Interaction of FOXP2 species variants with CtBP proteins. **A.** BRET assay to assess interaction of the species variants with CtBP1. **B.** BRET assay to assess interaction of the species variants with CtBP2. The plotted values are means of biological triplicates from one representative experiment and the error bars represent standard deviation.

generated in this research group. Western blot analysis was done with whole cell lysates of HEK293 cells transfected with these Myc-tagged FOXP2 variants (Fig. 5B). All the variants were expressed and there was no difference seen between the species variants with all of them running at around 100 kDa on the gel.

In addition to the Myc-tagged variants, YFP-tagged variants were also generated in this lab. Fluorescence imaging was done using HEK293 cells transfected with YFP-tagged species variants (Fig. 5C). Results show that all variants are nuclear and do not show any difference in localization when compared to the human FOXP2 variant, which is expected since the variants do not affect the nuclear localization signals of FOXP2.

We assessed regulation of the SV40 promoter by the species variants using a luciferase assay (Fig. 5D). All the variants repressed the SV40 promoter to a similar extent as the human FOXP2 protein, which is consistent with the fact that the variants do not affect the DNA-binding domain.

The ability of the different species variants to dimerize was assessed in a BRET assay using variants fused to Renilla luciferase and human FOXP2 fused to YFP (Fig. 5E). All the variants showed a similar level of BRET signal, indicating that these variants do not affect dimerization, which is also not surprising given that the amino acid differences are outside the leucine zipper domain.

Finally, the interaction of the species variants with CtBPs was assessed using the BRET assay (Fig. 6). All the variants were found to interact with CtBP1 and CtBP2 to a similar extent as human FOXP2.

Therefore in all the assays performed here, there is no difference in behaviour between human FOXP2 and ancestral forms of the protein. This is not unexpected because the basic molecular function of FOXP2 must have been conserved in evolution. Identifying differences between the species variants will require additional experiments, for example, looking at additional protein-protein interactions, post-translational modifications, and effects on cultured neurons. The constructs described here will be useful for dissecting the effects of different amino acid substitutions on protein activity.

2.4 Characterization of *FOXP2* mutations identified in patients with neurodevelopmental disorders

There have been a handful of mutations reported in *FOXP2* as well as chromosomal rearrangements. We reviewed the literature for mutations reported in *FOXP2* in patients with neurodevelopmental disorders. These mutations are summarized in Table 1 and Figure 7A.

The first identified mutation (R553H) in the KE family was a change in the nucleotide in exon 14 from a guanine to adenine (Lai et al., 2001). This resulted in a change in the amino acid sequence in the protein at position 553 (in forkhead domain) from an arginine to histidine (R→H). A mutation screening study on the entire coding region of *FOXP2* in children with a primary diagnosis of verbal dyspraxia detected three probands with a mutation affecting the protein (MacDermot et al., 2005). The mutation (R328X) was found to cause a cytosine to thymine transition in exon 7 and yielded a stop codon at position 328. The resulting protein was truncated and lacked the forkhead, leucine zipper and zinc finger domains. The mutation is unlikely to represent a polymorphism. The proband, a 4 year old, had a similar phenotype to that of the affected KE family individuals. The child was reported to have development delays in speech and language, and social skills as well as having impairment in receptive and expressive language. The mutation was also detected in the affected mother and the sister and was not found in the unaffected father, indicating that the mutation is probably causative. Another mutation detected in the same study was a point mutation (Q17L) causing an adenine to thymine transition leading to a glutamine to leucine change at residue 17. The mutation lies in a region of unknown function near the N-terminus of the protein.

A mutation causing cytosine to thymine substitution in exon 15 was reported in a study of children with childhood apraxia of speech (Laffin et al., 2012). This missense mutation is found near the C-terminal of the protein just outside the forkhead domain. Prediction tools (PolyPhen-2) suggest that the mutation is likely to be pathogenic.

The first *de novo* patient mutation was reported in an eight year old boy (Turner et al., 2013). This two base pair deletion results in a frameshift and a stop codon truncating the protein after the zinc finger domain. The child has a complex phenotype including, but not limited to, chewing difficulty, delayed speech, oral and motor milestones, impaired articulatory production and delayed phonological processes. The boy exhibited typical features of childhood apraxia of speech as well as dysarthria. He showed severe impairment in receptive and expressive language skills, and word reading and spelling skills.

Another mutation reported in the same study was point mutation (cytosine to adenine change) that is found in the region after the leucine zipper. It was found in two of three family members with stuttering and no features of CAS or dysarthria. This mutation was not predicted to be pathogenic by prediction tools.

SRPX2 is one of FOXP2's target genes. Based on this information patients who reported disorders linked to *SRPX2* mutations or other disorders with similar clinical spectrum (continuous spike-and-waves during sleep (CSWS) and Landau-Kleffner syndromes) were screened for *FOXP2* mutations (Roll et al., 2010). They found a heterozygous missense *FOXP2* mutation (M406T) in a patient reporting focal epilepsy with CSWS and cognitive and language deficits. The mutation resulted in a methionine to threonine substitution in the leucine zipper domain of the protein.

The R553H, R328X and Q17L mutations have been characterized previously (Vernes et al., 2006) and serve as controls in our evaluation of the more recently reported mutations: M406T, N597H, Q390VfsX5 and P416T. The M406T mutation is found in the leucine zipper which is the dimerization domain of the protein and may impact the ability of the protein to form homo- and heterodimers. The N597H mutation is found close to the DNA binding domain which may play a role in the ability of the protein to bind DNA and thereby regulate genes.

Constructs that contain the R553H, Q17L, R328X, M406T and N597H FOXP2 variants fused to YFP, Renilla luciferase (RLuc) and Myc tags were previously generated in this lab. In addition to these

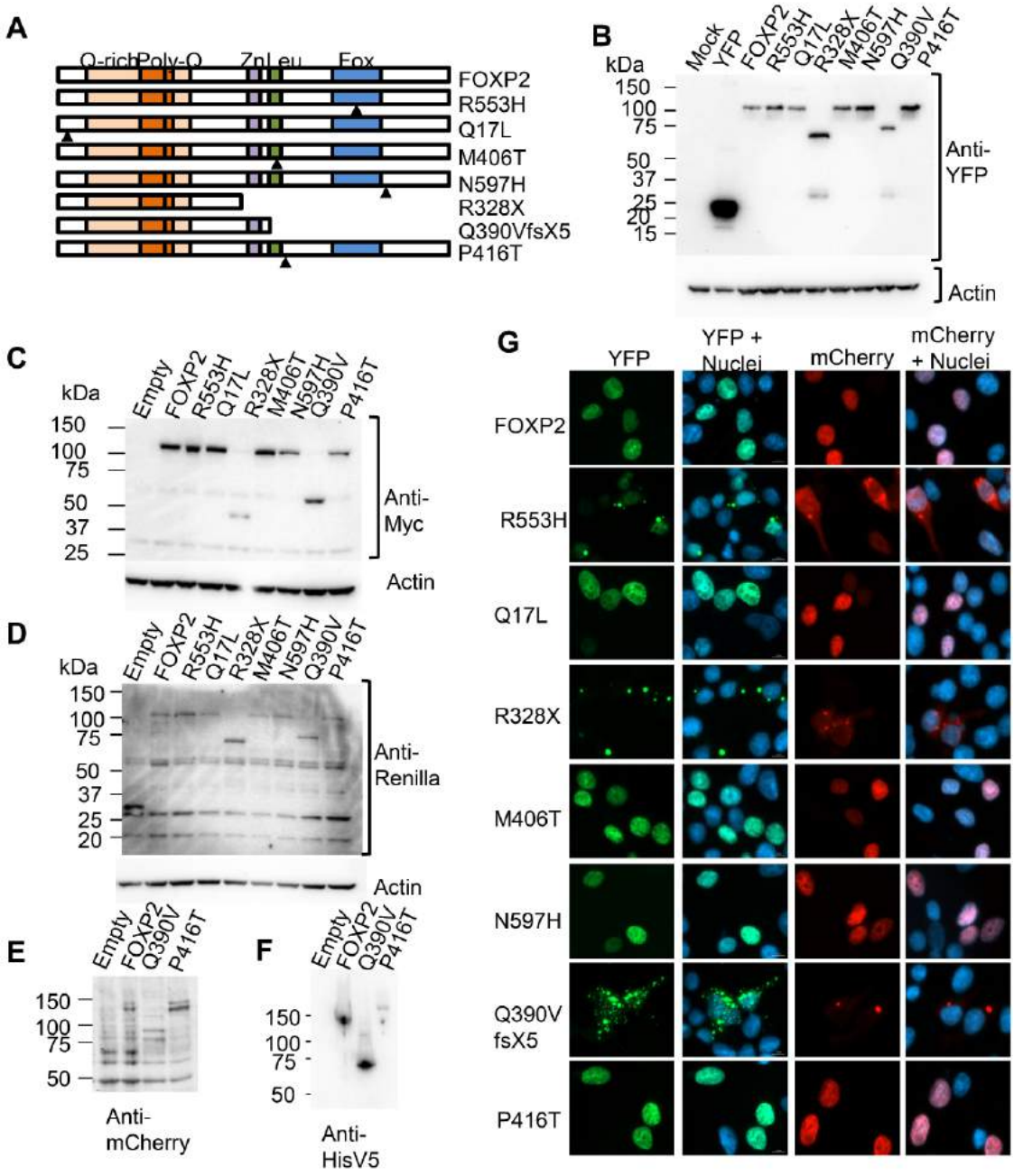

Fig. 7. Characterization of FOXP2 variants found in patients with neurodevelopmental disorders. **A.** Schematic representation of the FOXP2 variants reported in patients with neurodevelopmental disorders. Triangles indicate positions of mutations. **B.** Western blot analysis of whole cell lysates of HEK293 cells transfected with the YFP-tagged FOXP2 variants. **C.** Western blot analysis of whole cell lysates of HEK293 cells transfected with the Myc-tagged FOXP2 variants. **D.** Western blot analysis of whole cell lysates of HEK293 cells transfected with the Renilla-tagged FOXP2 variants. **E.** Western blot analysis of whole cell lysates of HEK293 cells transfected with the mCherry-tagged wild-type, Q390VfsX5 and P416T FOXP2 variants. **F.** Western blot analysis of whole cell lysates of HEK293 cells transfected with the HisV5-tagged wild-type, Q390VfsX5 and P416T FOXP2 variants. **G.** Fluorescence microscopy images of HEK293 cells transfected with YFP- and mCherry-tagged FOXP2 variants.

constructs, we generated constructs containing the Q390VfsX5 and the P416T mutations tagged with YFP, RLuc, Myc, HisV5 and mCherry. The sequences were generated by site directed mutagenesis using the wild-type *FOXP2* sequence in the vector pCR2.1-TOPO as a template and then subcloned into vectors containing the YFP, RLuc, Myc, HisV5 and mCherry N-terminal tags.

Western blot analysis of whole cell lysates of HEK293 cells transfected with these constructs (Fig. 7B, 7C, 7D, 7E, 7F) show that Q17L, M406T, N597H and P416T all have the same molecular weight as the wild type FOXP2 protein, running at just above a 100kDa. The truncated Q390VfsX5 runs at 75kDa while the R328X runs just below 75kDa. This is in line with the predicted protein structure,

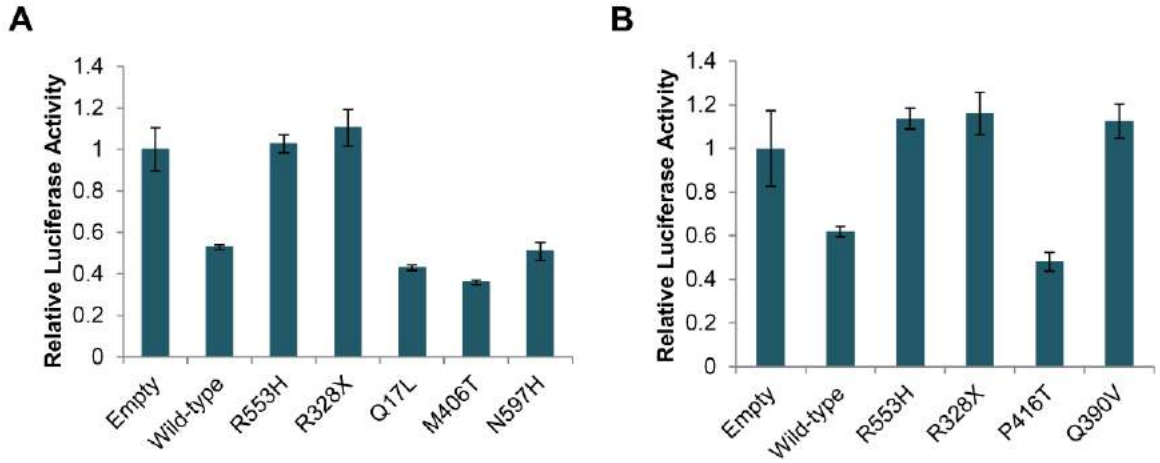

Fig. 8. Regulation of transcription by FOXP2 variants reported in patients with neurodevelopmental disorders. **A.** Luciferase assay to asses regulation of the SV40 promoter by the R553H, R328X, Q17L, M406T and N597H variants in HEK293 cells. **B.** Luciferase assay to assess regulation of the SV40 promoter by the Q390VfsX5 and P416T patient mutation constructs in comparison to wild type FOXP2, R553H and R328X in HEK293 cells. The plotted values are means of biological triplicates from one representative experiment and the error bars represent standard deviation.

given that Q390VfsX5 and R328X both lack a major part of the protein including the leucine zipper and the FOX domain. R328X also lacks the zinc finger domain. HisV5- and mCherry-tagged Q390VfsX5 and P416T also show the same result as with the YFP tags. These results, using antibodies to the protein tag, are consistent with the previous results on Q17L, R328X and M406T that use antibodies to an N-terminal Xpress tag (Roll et al., 2010; Vernes et al., 2006). The R328X runs lower on the gel while the Q17L and M406T do not differ from the wild type FOXP2. The Renilla luciferase and the mCherry antibodies were found to show poor specificity with several bands observed at unexpected molecular weights. The R328X shows a very low expression with Xpress tag (Vernes et al., 2006). Tags such as the YFP used here stabilize the protein causing higher expression levels, whereas small tags like Myc show low levels of expression similar to Xpress tag. Q390VfsX5 shows good expression even with the small Myc tag, indicating that amino acids present in Q390VfsX5 but not in R328X contribute to protein stability. Perhaps the presence of the zinc finger in the Q390VfsX5 and not the R328X impacts protein stability.

In addition to utilizing these constructs for Western blotting, they can also be used for future experiments including pull-downs to detect protein-protein interaction and ChIP experiments to identify and characterize potential targets and their regulation.

Intracellular localization of R553H, Q17L, R328X, M406T have previously been investigated (Roll et al., 2010; Vernes et al., 2006) and immunofluorescence results show that Q17L and M406T are nuclear while R328X shows diffused cytoplasmic aggregates. R553H shows both cytoplasmic and nuclear localization with a few cytoplasmic aggregates. We performed fluorescence imaging with these mutations transfected with either YFP or mCherry tags (Fig. 7G). Our results for the R553H and Q17L constructs are consistent with previous results (Roll et al., 2010; Vernes et al., 2006). In contrast to these results, however, we find that M406T construct still maintains nuclear localization with both YFP and mCherry tags and the R328X forms aggregates in addition to cytoplasmic localization. Moreover, we assessed intracellular localization of N597H, Q390VfsX5 and P416T tagged with YFP and mCherry. Both N597H and P416T were found to be nuclear while Q390VfsX5 shows aggregate formation in the cytoplasm

We assessed the ability of the proteins to repress the SV40 assay using a luciferase assay. Previous results have shown that the R553H and R328X mutations abolish the regulatory effect of FOXP2 on the SV40 promoter while the Q17L mutation still leaves the protein capable of this repression (Vernes et al., 2006). Our results are consistent with this, showing a loss of regulatory function with the R553H and the R328X mutations and repression with the Q17L mutation. In addition, we also assessed the regulation of the SV40 promoter by the FOXP2 variants containing the M406T, N597H, Q390VfsX5 and the P416T mutations. The M406T variant has been previously assessed in its ability to regulate expression of the *SRPX2* promoter, with results showing that the protein is still capable of repressing the promoter. Here, we assessed the ability of this variant to repress the SV40 promoter

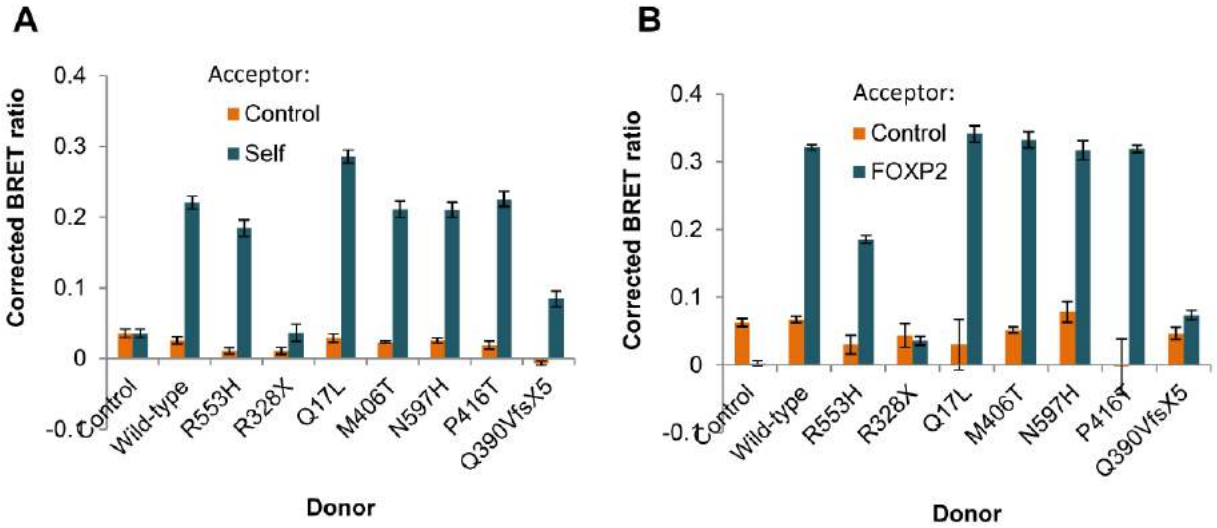

Fig. 9. Dimerization capability of FOXP2 variants reported in patients with neurodevelopmental disorders. **A.** BRET assay to asses homodimerization of the patient mutation constructs in HEK293 cells. **B.** BRET assay to assess interaction between the patient mutation and wild type FOXP2 in HEK293 cells. The plotted values are means of biological triplicates from one representative experiment and the error bars represent standard deviation.

and find that the protein also represses the SV40 promoter and the effect is similar to that of FOXP2. N597H also represses the SV40 promoter indicating that the mutation, despite its proximity to the DNA binding domain, does not impact the regulatory function of the protein. The same result was found for P416T which also retains the ability to repress the SV40 promoter. However, Q390VfsX5 does not repress the SV40 promoter. This is to be expected, as the protein lacks the DNA binding domain.

We then assessed the homodimerization of the FOXP2 constructs with the patient mutations using a BRET assay (Fig. 9A). All the full length patient mutation variants were found to form homodimers, having BRET ratios around the range of that for FOXP2. R328X did not form a homodimer, probably due to the lack of the leucine zipper that mediates dimerization. Q390VfsX5, that lacks the leucine zipper but retains the zinc finger, has a BRET ration that is lower than the mutation variants that dimerize but higher than that for R328X. The signal could be a result of non-specific protein interactions that arise due to proximity of two protein molecules and not necessarily due to a specific interaction.

Similar results were found when we assessed the interaction between these patient mutation constructs and FOXP2 (Fig. 9B). Q17L, M406T, N597H and P416T all show an interaction with wild-type FOXP2 comparable to that of the wild-type protein. R328X and Q390VfsX5 did not form heterodimers with FOXP2. R553H showed a lower BRET ratio when assessing its interaction with FOXP2. This could be due to the cytoplasmic expression of R553H. This heterodimerization could impact the functioning of the mutated proteins

We also assessed the interaction between these FOXP2 variants with CtBPs using fluorescence imaging and BRET assays. We co-transfected HEK293 cells with YFP-tagged FOXP2 patient mutation variants and mCherry-tagged CtBP1, (Fig. 10A) and CtBP2 (Fig. 10B). We see that mutants that retain nuclear localization, namely Q17L. M406T, N597H and P416T all show some degree of co-localization with CtBP1 in the nucleus. Mutants that cause cytoplasmic localization of the FOXP2 protein, however, show a high degree of co-localization with CtBP1. With the R328X and the Q390VfsX5 mutated constructs, we observe co-localization with CtBP1 in aggregates. This colocalization is also reflected in the BRET results where the cytoplasmic mutants have a higher BRET ratio when compared to the other mutations (Fig. 10C). This could imply that mutated FOXP2 proteins drag in CtBP1 protein molecules into the aggregates thereby interrupting other protein-protein interactions of CtBP1.

Fluorescence images of YFP-tagged FOXP2 patient mutations co-transfected with mCherry-tagged CtBP2 show that there is a high degree of co-localization with mutants that retain nuclear localization (Fig. 10B). Therefore, Q17L, M406T, N597H and P416T all show nuclear co-localizations. Mutants with cytoplasmic localization, on the other hand, show little to no co-localization except for the R328X which shows co-localization in the aggregates. R553H and Q390VfsX5 both show cytoplasmic aggregates that do not co-localize with the CtBP2 which is exclusively found in the nucleus. Results from the BRET assay show a high signal

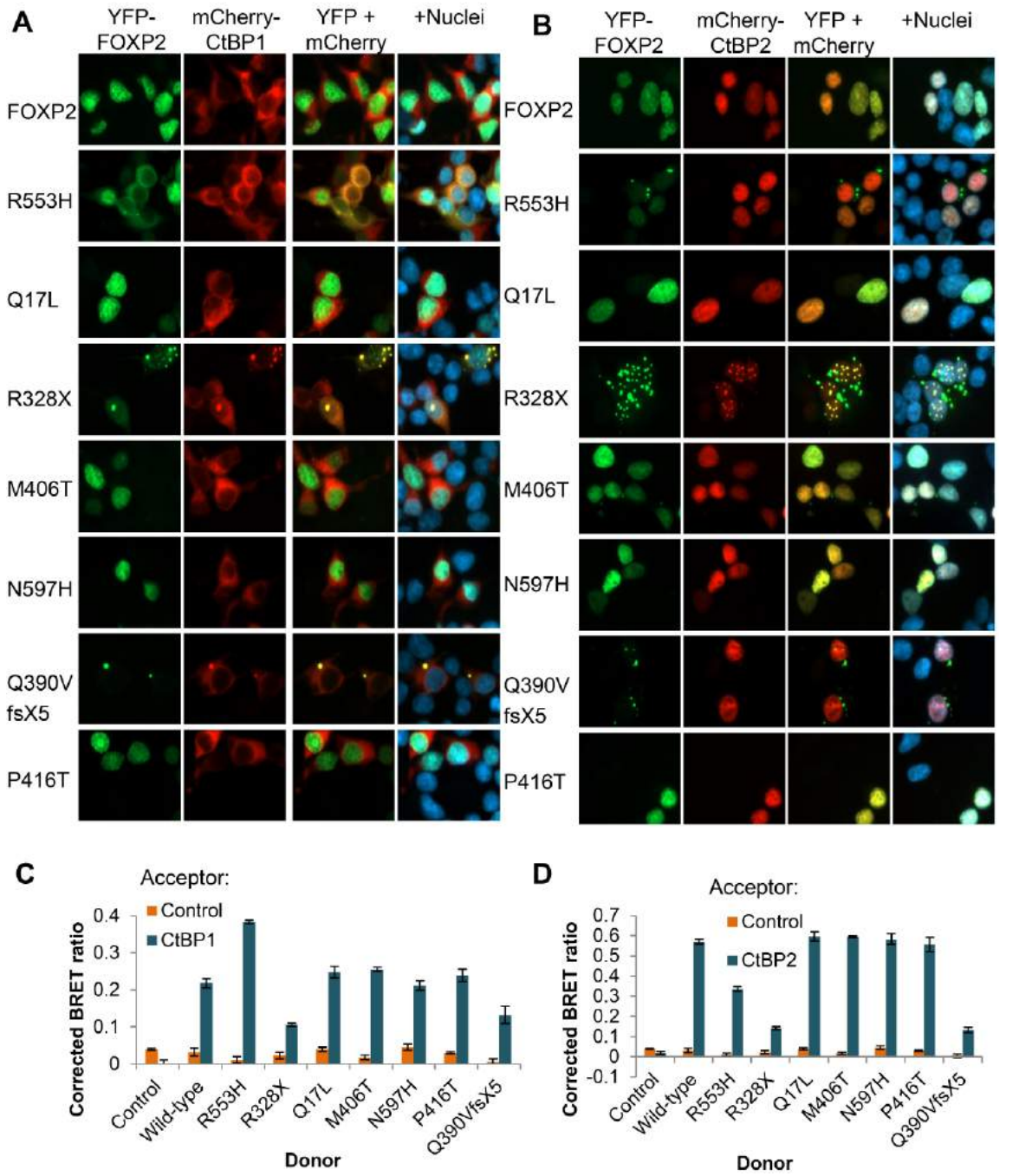

Fig. 10. Interaction of FOXP2 variants reported in patients with neurodevelopmental disorders with CtBP proteins. **A.** Fluorescence microscopy images of HEK293 cells co-transfected with YFP-tagged FOXP2 variants (green) and mCherry-tagged CtBP1 (red). **B.** Fluorescence microscopy images of HEK293 cells co-transfected with YFP-tagged FOXP2 variants (green) and mCherry-tagged CtBP2 (red). **C.** BRET assay to assess interaction between FOXP2 variants and CtBP1 in HEK293 cells. **D.** BRET assay to assess interaction between FOXP2 variants and CtBP2 in HEK293 cells. In C and D, the plotted values are means of biological triplicates from one representative experiment and the error bars represent standard deviation.

for the nuclear localized proteins indicating an interaction (Fig. 10D). The cytoplasmic variants also show a BRET signal although it is lower than that of the nuclear FOXP2 variants (Fig. 10D). A BRET signal is observed even for R328X, indicating that the binding site is still retained in this- the shortest FOXP2 variant.

In summary, a major difference in function can be seen in the truncated FOXP2 proteins and the R553H. N597H was reported as likely to be pathogenic (Laffin et al., 2012). However, we find here that the mutation does not impact either the intracellular localization or the function of the protein. This indicates that the protein still retains its ability to function normally and therefore may not be causal. In addition, we find that the Q390VfsX5

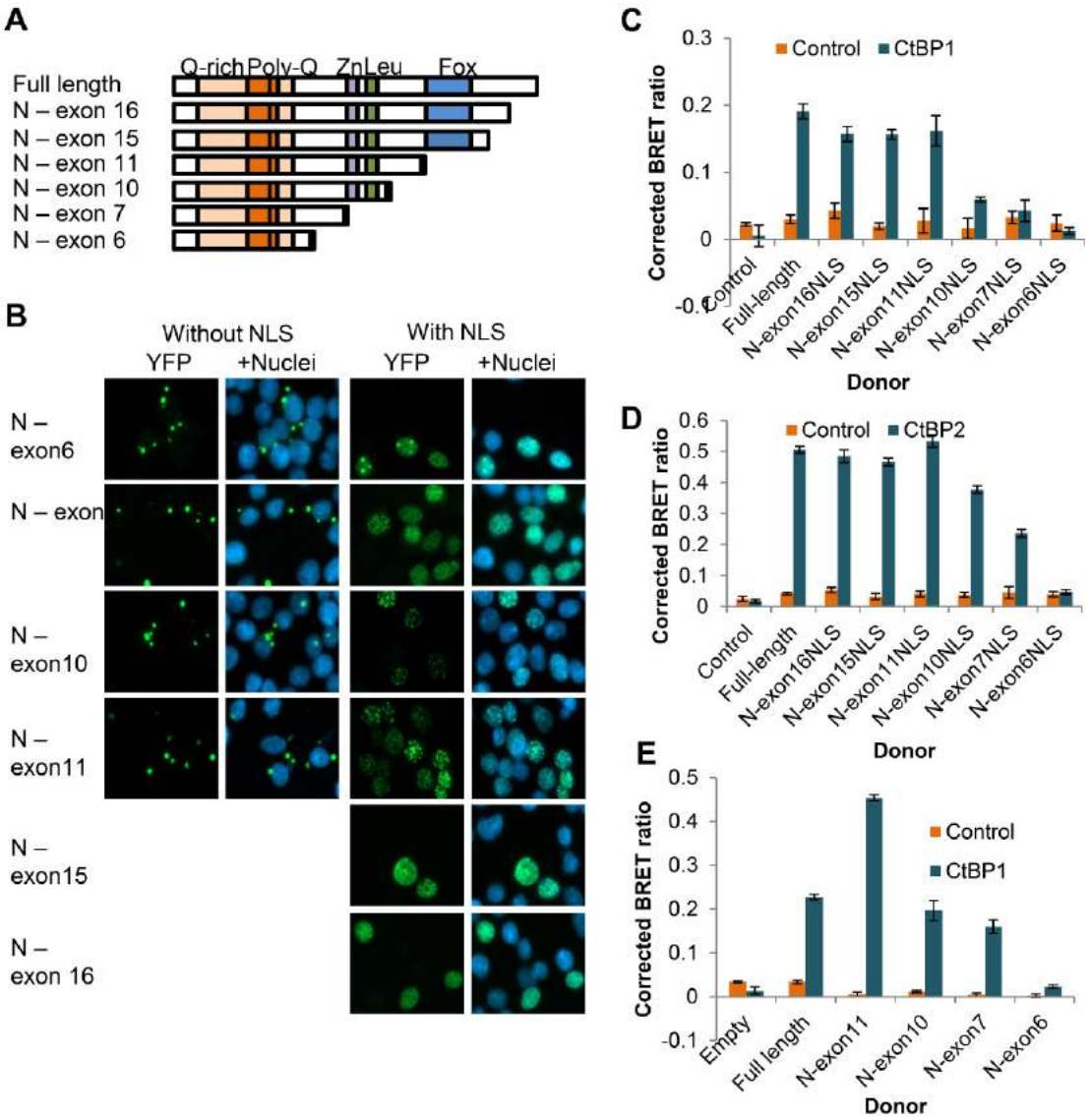

Fig. 11. Mapping the CtBP binding site using synthetic C-terminal truncations of FOXP2. **A.** Schematic representation of the synthetic C-terminal truncations extending from N-terminal to different exons. **B.** Fluorescence miscroscopy images of HEK293 cells transfected with YFP-tagged C-terminal truncations of FOXP2. The left panel shows images with constructs that do not contain a nuclear localization signal (NLS) while the right panel shows the same constructs but with an NLS attached. The exon 15 and exon 16 truncation contain endogenous NLS. **C.** BRET assay to assess interaction of NLS-containing C-terminal truncations with CtBP1. **D.** BRET assay to assess interaction of NLS-containing C-terminal truncations with CtBP2. **E.** BRET assay to assess interaction of C-terminal truncations not containing an NLS with CtBP1. In C, D and E, the plotted values are means of biological triplicates from one representative experiment and the error bars represent standard deviation.

shows a drastic difference in both intracellular localization and function when compared to wild type FOXP2. This indicates that the mutation could be pathogenic impacting how the protein functions in the cell and altering its effect. The P416T, on the other hand, still retains the localization and function when compared to the wild type FOXP2. These results also echo the phenotype of the patients. The patient with the *de novo* Q390VfsX5 mutation was shown to have a marked impairment in oral motor skills that was not found in the parents, while the patient with the P416T mutation showed phenotypic resemblance to another member of the family without the mutation. These results, in general, also highlight the relevance of functional characterization of the protein in a clinical setting.

2.5 Mapping the CtBP binding site in FOXP2

R328X, the shortest reported patient mutation, did not result in a total loss of interaction between FOXP2 and CtBP1. This indicates that this variant still retained at least part of the CtBP1 binding site.

In order to map the location of the CtBP1 binding site within the FOXP2 protein, we used truncations of the protein of different lengths, which have been generated previously in this research group (Fig. 11A). Truncations that do not contain the DNA binding domain and the immediate region around it lack the nuclear localization signals (NLS), therefore truncations shorter than the exon 11 were also made as versions containing an artificial NLS. Fluorescence images of YFP-tagged truncation mutations show that constructs that do not contain an NLS, either artificial or inherent, show cytoplasmic localization and also form aggregates (Fig. 11B). These same truncations, when attached with an artificial NLS, are efficiently re-targeted to the nucleus, where they form small aggregates. FOXP2 truncations that contain exon 16 and exon 15 still retain the two endogenous NLS and therefore appear nuclear.

In order to map the CtBP1 binding site, BRET assays were performed to assess the interaction between the different truncated variants of FOXP2 with CtBP1 and CtBP2. The interaction was assessed first with variants that contained the artificial NLS (Fig. 11C, 11D). In the case of both CtBP1 and CtBP2, truncations which included the protein encoded up until at least exon 11 showed a similar degree of interaction as the full-length FOXP2. For CtBP2 it was also clear that the variants truncated at the end of exon 10 or exon 7 also retained some binding ability, while the variant truncated at the end of exon 6 could no longer interact with CtBP2 (Fig. 11D). For CtBP1, the variants truncated at the end of exon 10 or exon 7 showed little or no binding. Since we expected that FOXP2 interacts with CtBP1 and CtBP2 through the same site, we thought that the discrepancy in the BRET results between CtBP1 and CtBP2 may be due to the differing subcellular localization of these protein – specifically, that the interaction between the shorter nuclear-targeted FOXP2 truncations and CtBP1 could not be detected because CtBP1 is in the cytoplasm. We therefore repeated the assay with CtBP1 using FOXP2 truncations without the NLS (Fig. 11E). In this experiment we observed that the variants truncated at the end of exon 7 or exon 10 retained some binding ability, whereas the variant truncated at the end of exon 6 did not show interaction. These results therefore mirror what was observed with CtBP2 and localize the CtBP binding site to within exon 7 of *FOXP2*. This is an interesting region of the protein because it shows the most variability between species, however as shown in Figure 5E, the human-specific changes in *FOXP2* do not affect CtBP binding. Our results also indicate that the CtBP binding site is not in the position suggested by Li and colleagues (Li et al., 2004).

2.6 Development of assays for FOXP2 transcriptional regulatory activity

While luciferase assays with the SV40 promoter tell us about the regulation of the viral promoter, they do not provide us with any biologically relevant information with regard to FOXP2 function in regulating genes that are relevant to neurodevelopment.

Putative FOXP2 target genes have been identified in earlier studies using ChIP and microarray techniques in different tissues and cell lines. These studies provide us with a large number of possible FOXP2 targets. We created list of putative targets from different studies (Konopka et al., 2009; Spiteri et al., 2007; Vernes et al., 2007, 2011) and filtered them based on several criteria including their relevance to neural development and functioning, and definition of the promoter region. Based on these filtering criteria, we selected two promoters, namely the promoters for the Cerberus 1 (CER1) and the Cholecystokinin (CCK) target genes. In addition to this, we also assessed targets that have been studied before, namely the Sushi-repeat containing protein, SRPX2 (Roll et al., 2010) and the mouse Clara cell 10 (mCC10) promoter (Weiguo Shu et al., 2007). The latter plays a role in mouse lung development. However, studies have shown that Foxp2 highly represses this promoter (W Shu, Yang, Zhang, Lu, & Morrisey, 2001) and so we assessed this promoter in our study as well.

In order to subclone the promoter regions into a plasmid with the luciferase gene as the reporter, a promoterless plasmid was generated with the pGL4 backbone (Fig. 11A).The promoter regions were selected, PCR amplified, cloned into the PCR cloning vector pCR2.1-TOPO plasmid and then subcloned into the promoterless plasmid. This plasmid was then used to assess regulation in luciferase assays. For all luciferase assays with the promoters, we assessed regulation by YFP-tagged wild-type FOXP2 and the R553H construct. The R553H mutation abolishes the DNA binding ability of FOXP2 and therefore acts as a good negative control. They were then compared to a control of an empty expression plasmid (pHis). In addition, we also assessed the effect of a YFP construct with no insert. In all the assays, we found no difference between the "Empty" and "YFP" conditions. The use of YFP-tagged constructs allowed us to

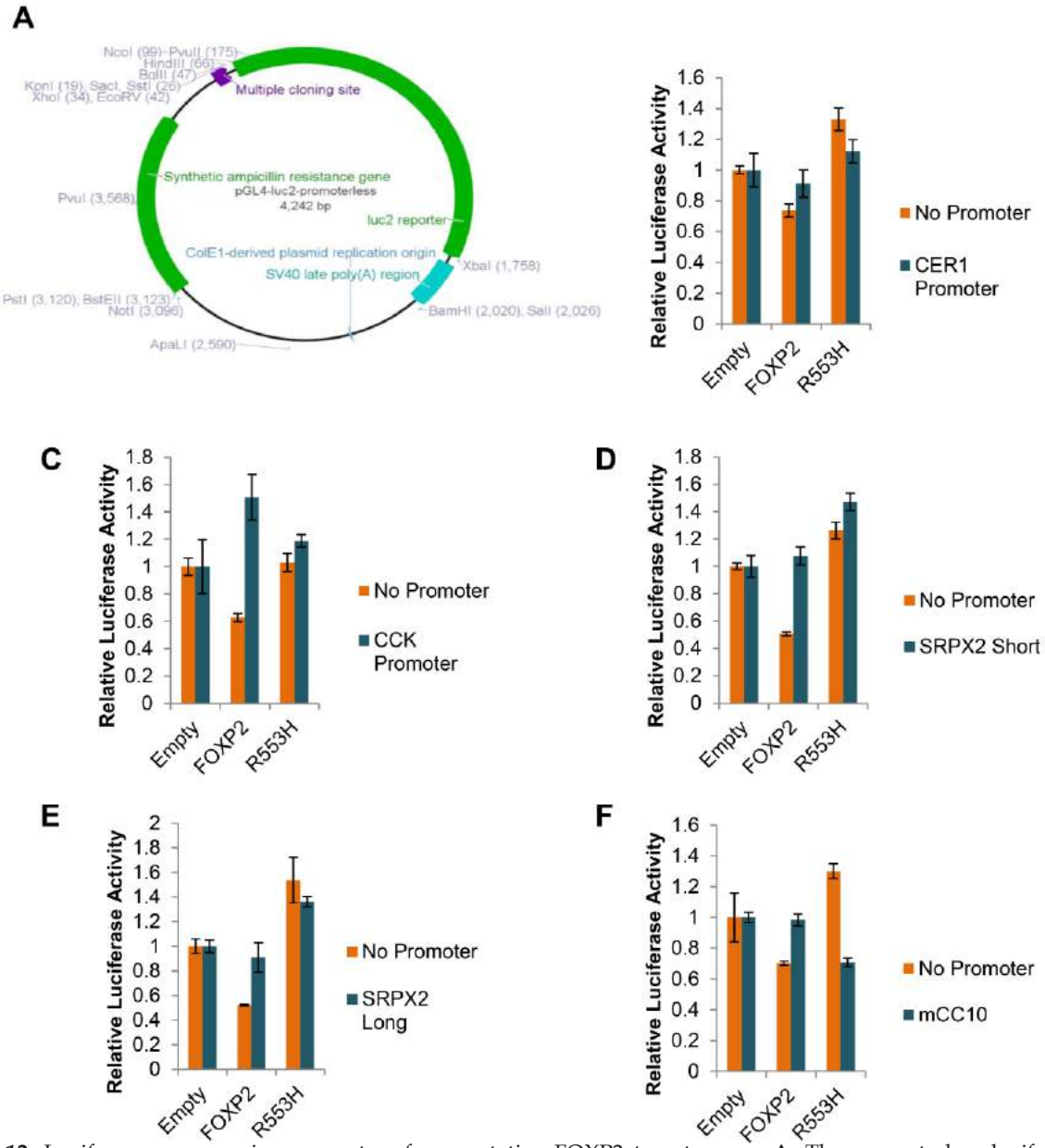

Fig. 12. Luciferase assays using promoters from putative FOXP2 target genes. **A.** The promoterless luciferase plasmid into which the promoters for FOXP2 target genes were subcloned. **B.** Luciferase assay to assess regulation of the CER1 promoter by FOXP2. **C.** Luciferase assay to assess regulation of the CCK promoter by FOXP2. **D.** Luciferase assay to assess regulation of the SRPX2 Short promoter by FOXP2. **E.** Luciferase assay to assess regulation of the SRPX2 Long promoter by FOXP2. In B-F, the plotted values are means of biological triplicates from one representative experiment and the error bars represent standard deviation.

monitor expression levels of FOXP2 to check that the proteins were expressed correctly in the assays. In short, we assessed the regulatory effects of a promoterless ("Empty") plasmid, wild type FOXP2 and the FOXP2 protein with the R553H mutation on the promoters for the *CER1*, *CCK*, *SRPX2* and *mCC10* target genes.

The first promoter we assessed was the CER1 promoter. CER1 is a FOXP2 ChIP target in SH-SY5Y cells, lung and inferior frontal cortex and CER1 mRNA levels were regulated by FOXP2 in quantitative PCR (qPCR) assays (Vernes et. al., 2007; Spiteri et. al., 2007). CER1 is a secreted protein and participates in the Wnt pathway that plays an important role in embryogenesis. The CER1 protein plays a role in neural induction by directly binding to and inhibiting the bone-morphogenic protein 4 (BMP-4). This inhibition, in turn, is crucial to neural induction (Biben et al., 1998). FOXP1/2/4 appear to repress the promoter as assessed through qPCR (Sin et al., 2014). We assessed the regulation of the CER1 promoter using the luciferase assay. We do not see a difference in regulation between the promoterless and the CER1 promoter conditions. We observe a slight repression of the promoterless plasmid. This could be due to FOXP2 consensus

binding sites on the promoterless plasmid. However, even in comparison to the repression seen with the promoterless plasmid, we did not observe a difference in activity with the CER1 promoter.

Another promoter we assessed was the promoter for the cholecystokinin CCK gene. FOXP2 ChIP target in lung and SH-SY5Y cells and was differentially expressed in mice lacking Foxp2 based on microarray and in situ hybridization experiments (Vernes et. al., 2007, Spiteri et. al., 2007, Vernes et. al., 2011). CCK is a neuropeptide and CCK receptors are found to be widely expressed throughout the central nervous system. Specifically, there is a high expression of the protein in the basolateral amygdala, striatum, hippocampus and cortical areas (Zwanzger, Domschke, & Bradwejn, 2012). In our study, although we do not observe a big difference in regulation of the promoter, there is an increase in luciferase activity which could mean that the promoter is active in HEK293 cells.

We also assessed the regulation of the *SRPX2* promoter. The sushi-repeat protein SRPX2 was reported to play a role in rolandic epilepsy and polymicrogyria (Roll et al., 2010), although this role is now less certain (Lesca et al., 2013). Also, mutations on this gene are found in patients with speech impairments. With this in mind, Roll and colleagues (Roll et al. 2010) assessed the regulation of the *SRXP2* gene by FOXP2. They found significant repression in SRPX2 levels using a luciferase assay. In addition, they report that FOXP2 represses the promoter by directly binding to FOXP consensus binding sites. We cloned two promoter fragments of SRPX2 ("SRPX2 short" and "SRPX2 long"). We did not use the same region as was used in the earlier study because this region contains start codons upstream of the luciferase start codon which may cause incorrect translation of transcripts produced from the plasmid. In contrast to previous results we do not see a difference in repression, either with the "long" or the "short" promoter region, between the empty condition and the FOXP2 condition.

Finally, we assessed the mouse Clara cell specific protein 10 (mCC10) promoter that plays a role in lung development. mCC10 was found to show considerable repression by Foxp2 in a lung cell line (Weiguo Shu et al., 2007). However, using the same region as the previous study, we did not see a difference between the empty and the FOXP2 condition.

There are several reasons why we may have failed to observe an effect of FOXP2 expression on luciferase expression in our assays. Endogenous FOXP2 found in HEK293 cells may already have a saturated effect on the promoter and overexpressing the protein does not produce any measurable difference in regulation. Perhaps, these promoters are not highly active in HEK293 cells, given that they play a role in either neural, or in the case of the mCC10, lung development. Potential interacting partners of FOXP2 for regulation of these promoters may be absent in HEK293 cells, due to which we do not observe an effect.

We did observe that FOXP2 expression represses luciferase expression from the promoterless vector. The promoterless plasmid contains several consensus binding sites for FOXP2 and FOXP2 could possibly repress the expression of the luciferase gene by binding to these sites. However, a highly active promoter would, most likely, result in a big difference in the luciferase activity which would drown out the repression seen with the promoterless construct.

3. Discussion

FOXP1, FOXP2 and FOXP4 have a high degree of similarity. In particular, FOXP2 is shown to have a high degree of similarity with FOXP1. This is reflected in the fluorescence images, interaction with CtBP1 and CtBP2, and regulation of the SV40 promoter. This indicates that they have a similar function at the molecular level. Surprisingly, FOXP4, despite containing the NLS regions, was found to be cytoplasmic. This can also be seen in its ability to repress the SV40 promoter where it does not repress as much as FOXP2. In addition, FOXP4 does not show an interaction with CtBP1 and CtBP2, despite extensive co-localization with CtBP1.

Among the isoforms of FOXP2, isoform 10+ shows drastic difference in both intracellular localization and function. Although it does not repress the SV40 promoter, it still forms homodimers and also interacts with isoform I. By interacting with isoform I, it could impact FOXP2 function. Perhaps it retains the full-length FOXP2 in the cytoplasmic aggregates reducing the amount of the full length protein that can bind to DNA and regulate gene expression. Isoform III, on the other hand, only differs from isoform I by a stretch of amino acids at the N-terminus and does not show a difference in intracellular localization and function. This region might, therefore, have a more subtle impact on how the protein functions.

FOXP2 is a highly conserved protein with very few amino acid changes between the mouse, chimp and human variants. The species variants of FOXP2

do not show a difference in activity as assessed in our study. The changes that have occurred in the human lineage could have two possible implications. One implication is that these changes provide the protein with altered function that is specific to the human species. The second implication is that these changes occur in regions that do not play a crucial role in the protein function, due to which the region is less conserved and more prone to amino acid changes. Given that we do not see a difference in the localization or the function of the protein found in the different species, it is likely that these mutations are not in regions that greatly impact protein functions examined here. Further experiments would be needed to unravel potential differences, if any, in the function of FOXP2 in different species.

Assessing protein function of FOXP2 variants with mutations found in patients is an important aspect of elucidating the role of FOXP2 in the brain under normal conditions as well as in disorders. As we see here, phenotypic characteristics can be traced back, to a certain extent, to the function of FOXP2. Mutations that show severe and sometimes specific impairments can be seen to have a major impact on the function of the protein. The R553H and R328X mutations have already been shown to have an impact on protein localization and function consistent with co-segregation of the mutations with language disorder in these families. In contrast, the M406T and Q17L mutations do not co-segregate with the impairments and this is reflected in the functional characterization of FOXP2 shown both in previous studies and our study.

The N597H mutation was found while screening for mutations in children with childhood apraxia of speech. Since the mutation is found close to the DNA binding domain, it would appear that this mutation could impact the functioning of the protein and it has also been reported to likely be pathogenic. However, we see here that this mutation does not cause a change in the localization or the function of FOXP2, suggesting that this mutation may not be responsible for the phenotype in this patient. This also puts into perspective the role of functional characterization in a clinical setting. Analyzing protein function sheds light on the possible process of how the protein changes affect cells, tissues and ultimately the patient.

The Q390VfsX5 mutation was found in a patient who was born under fetal distress and had a complex phenotype including the phenotype observed in the KE family. The mutation also causes a drastic change in the protein leading to truncation of a major part of the protein including the DNA binding domain. The inability of the protein to bind to DNA could play a crucial role in the regulation of FOXP2 targets with the effect possibly stretching to specific brain regions. Our data therefore support a causal role of this mutation in the phenotype observed in this patient.

The P416T mutation did not affect the protein drastically. This mutation also did not co-segregate with the phenotype. Therefore, the characterization of the mutation on a protein level is in line with the phenotypic characterization indicating that the mutation is probably not causal.

Luciferase reporter assays using promoters from putative FOXP2 target genes is crucial to further our understanding of FOXP2's function in the human body. However our assay here did not show a big difference in regulation between the wild type FOXP2 protein and the mutated R553H protein. This apparent lack of effect could be due to several reasons as mentioned before. The promoters we assessed here are known to be active in neurons. Therefore, it is possible that these promoters are not particularly active in HEK293 cells. In addition, since the environment is different between cell types, there may be FOXP2 interactors that are not present in these cell lines due to which FOXP2 does not show a massive regulatory effect. It would be worthwhile to repeat these experiments in different cell lines, especially in a cell line that does not contain endogenous FOXP2. This would help us understand if endogenous FOXP2 is enough to show a repression or activation in the genes assessed here. In addition, assessing regulation in neuronal cell lines would help us understand if FOXP2 lacks interacting partners to show a difference in regulation.

The battery of tests that we have performed in this study could act as a good starting point for characterization of future mutations reported in the *FOXP2* gene. They provide a good understanding of the effect of the mutation on the protein function. This could act as a possible link between understanding the protein function and the effect it would have on a behavioural level. It would also help to differentiate between a mutation that could play a major role in the impairment and a mutation that is benign. A mutation that does not impact the protein drastically perhaps does not contribute to the phenotype or contributes very little to the overall characteristics of the impairment. These assays could therefore be used as an additional tool in diagnosing the aetiology of language impairment in patients. Functional characterization of FOXP2 also provides us with invaluable information about the

role FOXP2 plays in protein networks and in turn the brain networks that it affects. This information can then help in understanding the brain networks of language and provide possible entry points to treatment opportunities.

4. Methods

4.1 Agarose gel electrophoresis

Agarose gels (usually 1% w/v) were prepared in 1X Tris-Borate-EDTA (BioRad) with 0.01% v/v SyberSafe (Life Technologies) to allow for visualization of the DNA under ultraviolet light. Gels were visualized using ChemiDoc XRS (BioRad).

4.2 Gel purification

The Promega Kit was used. The bands were extracted and dissolved in 100µl of membrane binding solution. The samples were then incubated at 50˚C with intermittent mixing until the gel slice is dissolved. The solution was then added to a spin column and centrifuged for 1 minute. The column was first washed with 700 µl and then with 500 µl of membrane wash solution. The DNA was then eluted in 30 µl of 10mM Tris pH 8.0 into a 1.5ml microcentrifuge tube.

4.3 PCR

PCR reaction mix was made to a final volume of 10 µl containing 1 µl of 10X Advantage 2 buffer, 0.2 µl of the forward and the reverse primers, 0.2 µl dNTPs, 0.2 µl genomic DNA (260 ng/µl) and 0.2 µl Advantage 2 polymerase enzyme. Cycling parameters were as follows:

Initial denaturation	3min at 94°C
Thermal cycling	30s at 94°C; 2min at 65°C
Final Extension	5min at 65°C

Typically 40 cycles of annealing and extension were performed.

4.4 Cloning PCR products

TOPO-TA cloning kit was used to clone PCR products. The final reaction mix of 6 µl contained 1 µl of salt solution 1 µl of the PCR product and 0.5 µl of the pCR2.1-TOPO vector (kept cold). The mixture was then diluted to to 6 µl. the reaction was incubated at room temperature for 20 minutes. The quantity of the PCR product can be adjusted depending on the intensity of the band.

4.5 Preparation of DNA

PureYield Miniprep and Midiprep Kits (Promega) were used to prepare DNA samples. The manufacturer's protocols were used. For the miniprep, a single colony from the transformation plate was inoculated into 2.5 ml of LB medium and cultured overnight at 225 rpm at 37˚C. 1.5 ml of this culture was used for the miniprep. For the midiprep, 100 µl of the culture was used to inoculate 150 ml of LB medium containing the appropriate antibiotic and cultured overnight at 37˚C and 225 rpm.

4.6 Restriction digestion

The FastDigest enzyme system (Fermentas) was used. The reaction mix contained 2 µl of the FastDigest green buffer, no more than 2 µl of the restriction enzymes and 0.5 µg of DNA was used for analytical digests and 2 µg of DNA for peparative digests. The final volume was made up to 20 µl using nuclease free water.

4.7 Ligation

The T4 ligase (NEB) was used. Reaction mix contained 1 µl of the T4 ligase, 1 µl of the NEB T4 ligase buffer and 50 ng of DNA in the ratio of 3 moles of insert: 1 mole of vector. The final volume was made up to 6 µl with nuclease free water. The reaction was then incubated at room temperature for 1 hour. For difficult ligations, incubation was done at 16˚C overnight.

4.8 Bacterial transformation

Competent cells were obtained from Life Technologies. DH5α Subcloning Efficiency Competent Cells were used for cloning of PCR products, routine subcloning and re-transformation. 40 µl of competent cells were transformed using 1 µl of the ligation reaction and incubated on ice for 30 minutes. The cells were then heat shocked at 42˚C for 20 seconds. The cells were then recovered in 200 µl of S.O.C. medium and cultured for 1 hour at 37˚C. The cells were then plated onto agar plates containing the appropriate antibody. For transformations with the TOPO plasmid, the plates with appropriate antibody were first spread with 100 µl of 2% X-Gal prior to spreading the culture.

Table 2. Primers for cloning promoter regions.

Promoter for	Forward Primer	Reverse Primer
CER1	AGCCATGGGAAATTTAGGCAAAG	CCATGGTGTCAGGGGCCCAAGCTTCTTTTG
CCK (Part 1)	AGATCTGCCCCCTCCCTTTCAGAATC	CTCTACCCACCCAGACCTCA
CCK (Part 2)	CCTCCCTGAACTTGGCTCAG	CCATGGCTGGCTGGTCTTTGGGAACTC
SRPX2 Long (Part 1)	GGTACCCTCTGCCTCCTGGGTTCAAG	TCCCACACTAAGAATGGAGGG
SRPX2 Short (same as SRPX2 Long part 2)	GGTACCCAGAGACCACTGGGAAGCAG	AAGCTTGATGGGGGAGAAGGAACACA
mCC10	GGTACCGGTAAGGCCTGGGAATGGCTAAC	CTCGAGGGGTATGTGTGGGTGTGTGGC

4.9 Sequencing

All constructs were verified by Sanger sequencing. Sequencing was performed by the Radboud University Medical Center Sequencing Facility.

4.10 FOXP2 constructs

The following plasmids have been previously generated in this research group:

The pYFP, phRLuc, pMyc, pmCherry and pHisV5 plasmids with no insert and with the coding sequences for FOXP1, FOXP4, FOXP2, Isoform III, Isoform 10+, N303T, S325N, N303T+S325N, Mouse, R553H, Q17L, R328X, M406T and N597H.

4.11 Creation of the Q390VfsX5 and P416T FOXP2 variants

The coding sequences for Q390VfsX5 and the P416T mutations were generated using the Quick Change Site Directed Mutagenesis Kit (Stratagene) using wild-type FOXP2 in pCR2.1-TOPO as a template. The following primers were used:

Q390VfsX5:

Forward:TGCGACCCTCAGAGACCAAACCA TCTCCC

Reverse:TAGAAAGCTGTATTTCTAACTTG CACCACCTGCATTTGC

P416T:

Forward:TGCGACCCTCAGAGACCAAACCA TCTCCC

Reverse:GGGAGATGGTTTGGTCTCTGAG GGTCGCA

The coding sequences for the FOXP2 protein with Q390VfsX5 and the P416T mutations were then subcloned into the mammalian expression vectors using BamH I and Xba I sites.

4.12 Creation of the promoterless luciferase plasmid

A 1200 bp NotI/HindIII fragment containing a multiple cloning site from pGL4.23 (Promega) was ligated into the backbone of pGL4.13 (Promega), from which the SV40 promoter and enhancer elements had been removed.

4.13 Creation of promoter plasmids

Promoter regions of *CER1*, *CCK*, *SRPX2* Short, both parts of *SRPX2* "Long" and *mCC10* were PCR amplified using human fetal brain cDNA as template. The amplicons were then cloned into the TOPO vector.

4.14 Primers for cloning promoter regions

The coding region for each promoter was then subcloned from the pCR2.1-TOPO vector into the promoterless luciferase plasmid as follows:

The promoter sequence for *CER1* was ligated into the promoterless vector using Nco I sites. The genomic DNA sequence already contains an Nco I site and this was used in the subcloning.

The promoter sequence for *CCK* (Part 1) and *CCK* (Part 2) was cut from the pCR2.1-TOPO backbone using Bgl II/ Sac I and Sac I/Hind III respectively. The part of the sequence that overlapped with both parts of the *CCK* promoter contained a Sac I site. *CCK* (part 1) and *CCK* (Part 2) were ligated together into the promoterless plasmid using the Bgl II and Hind III sites.

The promoter sequence for *SRPX2* Long (Part 1) and *SRPX2* Long (Part 2) was cut from the pCR2.1-TOPO backbone using Kpn I/ Sph I and Sph I/ Hind III respectively. The part of the sequence that

Table 3. Primary antibodies used for Western Blotting.

Antigen	Supplier	Raised in	Clonality	Isotype	Working Dilution
GFP	Clontech	Mouse	Monoclonal	IgG2a	1:8000
Renilla luciferase	Thermo Scientific	Rabbit	Polyclonal	IgG	1:2000
c-Myc	Santa Cruz Biotechnology	Mouse	Monoclonal	IgG	1:2000
mCherry	Novus Biologicals	Mouse	Monoclonal	IgG2a	1:1000
V5	Abcam	Mouse	Monoclonal	IgG2a	1:2000

overlapped with both parts of the *SRPX2* Long promoter contained a Sph I site. *SRPX2* Long (part 1) and *SRPX2* Long (Part 2) were ligated together into the promoterless plasmid using the Kpn I and Hind III sites.

The promoter sequence for *SRXP2* Short promoter was ligated into the promoterless vector using Kpn I and Hind III sites.

The promoter sequence for *mCC10* promoter was ligated into the promoterless vector using Kpn I and Xho I sites.

4.15 Mammalian cell culture

Cell culture reagents used are from Life Technologies unless otherwise specified. HEK293 cells were obtained from the European Cell And Culture Collection (ECACC). They were cultured in DMEM containing 10% fetal bovine serun, 2 mM L-glutamine and Penicillin/ Streptomycin.

4.16 Transient transfections

GeneJuice from Novagen was used. Cells were transfected at 40-80% confluency, cultured for 48 hours and then processed depending on the experiment. For 6-well plates, cells were seeded in 3 ml of complete medium. For each well, transfection of the DNA (1 μg) was done using 100 ul of the Opti-MEM and 3 μl of GeneJuice. For 24-well plates, cells were seeded in 2 ml of complete medium. For each well, transfection of the DNA (0.25 μg) was done using 20μl of Opti-MEM and 0.75 μl of GeneJuice. For 96-well plates, cells were seeded in 130 μl of complete medium. For each well, transfection of the DNA (180 ng total in 2 μl) was done using 6 μl of Opti-MEM and 0.19 μl of GeneJuice.

4.17 Microscopy

Cells were seeded on cover slips coated with 0.01% Poly-L Lysine (Sigma). After 48 hours of culture, the cover slips were washed with PBS and stained with 200 μl of Hoechst stain (1:10000 in PBS) for each cover slip. The cover slips were then mounted onto slides using a mounting medium (Dako).

4.18 Preparation of whole cell lysates

48 hours after transfection, cells grown in 6-well plates were washed with PBS. They were then lysed using 250 μl of lysis buffer containing 25 mM Tris pH7.5, 150 mM NaCl, 5 mM EDTA, 1% Triton X-100 and a protease inhibitor cocktail with 1% v/v PMSF. The cell suspension was then transferred to a microcentrifuge tube and incubated on ice for 30 minutes, mixing by pipetting up and down every ten minutes. The tubes were then centrifuged for 10 minutes at 4˚C. The supernatant was then used for further analysis.

4.19 Western blotting

Reagents for SDS-Polyacrylamide gel electrophoresis (SDS-PAGE) and western blotting were obtained from BioRad. Samples were resolved on 10% denaturing SDS-PAGE gels. Proteins were transferred to PVDF membranes using Ready-To-Use Membrane Stacks and TransBlot Turbo Blotting apparatus. The membranes were blocked in PBS containing 0.5% milk and 0.1% Tween. The antibodies were diluted in 0.5% milk. The membranes were incubated with primary antibody for 2 hours and with the secondary antibody for 1

Table 4. Secondary antibodies used for Western Blotting.

Antigen	Supplier	Raised in	Conjugate	Working Dilution
Mouse IgG	BioRad	Goat	HRP	1:5000
Rabbit IgG	Jackson ImmunoResearch	Goat	HRP	1:5000

hour. Membranes were washed with PBS containing 0.1% Tween and visualized using Novex ECL Chemiluminescent Substrate Reagent Kit (Life Technologies) and the ChemiDoc XRS system to detect antibody binding.

The primary antibodies used can be found in Table 3. The secondary antibodies used can be found in Table 4.

4.20 Luciferase assays

Cells were seeded in clear bottom 96-well plates in 130 µl of complete media. The following day, cells were transfected in triplicate with a total of 180 ng of DNA containing the firefly luciferase plasmid the promoter being assessed, the Renilla luciferase plasmid, an empty expression plasmid and a filler (pCR2.1-TOPO) plasmid.

The Promega Dual Luciferase kit was used for assessing luciferase activity. After 48 hours of transfection, cells seeded in 96-well plates were first washed with 100 µl of PBS and then lysed using 20 µl 1X Passive Lysis Buffer per well. After 15 minutes of incubation the plate was placed in the TECAN Infinite F200Pro plate reader. After injection of 50 µl of the firefly luciferase substrate (LAR II), luminescence was measured over 10 seconds. Once firefly activity was measured, of 50 µl of the Renilla luciferase substrate (Stop and Glo) was added and luminescence was measured for 10 seconds. The background (containing only the filler plasmid) was subtracted from the raw counts from each well. The firefly luciferase values were then normalized to the Renilla luciferase values to account for sample to sample variability other than that being tested. The mean was taken of the biological triplicates and the empty condition (containing only the firefly luciferase plasmid, Renilla luciferase plasmid, the filler and the empty expression) was then set to 1.0. The mean values for each condition were then plotted relative to the empty condition.

4.21 Bioluminescence Resonance Energy Transfer (BRET)

HEK293 cells (10% of a 75 cm2 flask) were plated in a clear-bottomed white 96-well plate in 130 µL of normal growth medium. The following day cells were transfected in triplicate with 6 fmol of Renilla fusion and 6 fmol of YFP fusion plasmids. The total mass of plasmid per well was adjusted to 60 ng using a re-circularized pCR2.1-TOPO vector. For each triplicate transfection 20µL of serum-free OptiMEM was combined with 1.8 µL of GeneJuice and incubated for 5 min at room temperature. DNA solution (180 ng total DNA in 2 µL) was added to the medium and incubated for 10 min at room temperature. The transfection mix was added to the cells (6.5 µL/well) and cells were grown for a further 24 hours before addition of luciferase substrate. The life cell Renilla luciferase substrate EnduRen (Promega) was dissolved in DMSO at 34 mg/mL and diluted 1:1000 in phenol red-free, HEPES-buffered DMEM containing 10% fetal bovine serum, 2 mM L-glutamine and Penicillin/Streptomycin. Medium was aspirated from the cells and replaced with 50 µL of diluted substrate. Cells were returned to the incubator for 5-20 hours. Luminescence was measured using a TECAN Infinite F200Pro plate reader. For each well the luminescence signal was integrated over 10 s using first a filter blocking wavelengths longer than 470 nm and then a band-pass filter permissive to wavelengths between 500 and 600 nm. The luminescence signal observed in the absence of Renilla luciferase was measured from wells transfected only with the filler pCR2.1-TOPO plasmid and was subtracted from all of the readings. The ratio of the luminescence signal from the Renilla luciferase that is observed with each filter set in the absence of a BRET acceptor was determined by transfecting a nuclear-targeted Renilla luciferase in the absence of a YFP fusion construct. This ratio was subtracted from the ratios obtained using pairs of Renilla and YFP fusion constructs to obtain the corrected BRET ratio. Following luminescence measurements the medium was aspirated from the plate and YFP fluorescence was measured from each well as a measure of protein expression levels.

References

Bacon, C., & Rappold, G. a. (2012). The distinct and overlapping phenotypic spectra of FOXP1 and FOXP2 in cognitive disorders. *Human Genetics*, 131(11), 1687–98.

Biben, C., Stanley, E., Fabri, L., Kotecha, S., Rhinn, M., Drinkwater, C., … Harvey, R. P. (1998). Murine cerberus homologue mCer-1: a candidate anterior patterning molecule. *Developmental Biology*, 194(2), 135–51.

Bruce, H. A., & Margolis, R. L. (2002). FOXP2 : novel exons , splice variants , and CAG repeat length stability. *Human Genetics*, *111*(2) 136–144.

Campbell, P., Reep, R. L., Stoll, M. L., Ophir, A. G., & Steven, M. (2010). rodents : Functional implications. *Journal of Comparative Neurology*, *512*(1), 84–100.

Carrion-Castillo, A., Franke, B., & Fisher, S. E. (2013). Molecular genetics of dyslexia: An overview. *Dyslexia*, *19*(4), 214–240.

Deriziotis, P., Graham, S. a, Estruch, S. B., & Fisher, S. E. (2014). Investigating protein-protein interactions in live cells using bioluminescence resonance energy transfer. *Journal of Visualized Experiments: JoVE*, (87), 1–15.

Enard, W., Gehre, S., Hammerschmidt, K., Hölter, S. M., Blass, T., Somel, M., … Pääbo, S. (2009). A humanized version of Foxp2 affects cortico-basal ganglia circuits in mice. *Cell*, *137*(5), 961–71.

Ferland, R. J., Cherry, T. J., Preware, P. O., Morrisey, E. E., & Walsh, C. a. (2003). Characterization of Foxp2 and Foxp1 mRNA and protein in the developing and mature brain. *The Journal of Comparative Neurology*, *460*(2), 266–79.

Groszer, M., Keays, D. A., Deacon, R. M. J., Bono, J. P. De, Gaub, S., Baum, M. G., … Fisher, S. E. (2008). Impaired Synaptic Plasticity and Motor Learning in Mice with a Point Mutation Implicated in Human Speech Deficits. *Current Biology*, *18*(5), 354–362.

Hisaoka, T., Nakamura, Y., Senba, E., & Morikawa, Y. (2010). The forkhead transcription factors, Foxp1 and Foxp2, identify different subpopulations of projection neurons in the mouse cerebral cortex. *Neuroscience*, *166*(2), 551–63.

Konopka, G., Bomar, J. M., Winden, K., Coppola, G., Jonsson, Z. O., Gao, F., … Geschwind, D. H. (2009). Human-specific transcriptional regulation of CNS development genes by FOXP2. *Nature*, *462*(7270), 213–7.

Laffin, J. J. S., Raca, G., Jackson, C. a, Strand, E. a, Jakielski, K. J., & Shriberg, L. D. (2012). Novel candidate genes and regions for childhood apraxia of speech identified by array comparative genomic hybridization. *Genetics in Medicine: Official Journal of the American College of Medical Genetics*, *14*(11), 928–36.

Lai, C. S., Fisher, S. E., Hurst, J. a, Vargha-Khadem, F., & Monaco, a P. (2001). A forkhead-domain gene is mutated in a severe speech and language disorder. *Nature*, *413*(6855), 519–23.

Lesca, G., Rudolf, G., Bruneau, N., Lozovaya, N., Labalme, A., Boutry-kryza, N., … Szepetowski, P. (2013). GRIN2A mutations in acquired epileptic aphasia and related childhood focal epilepsies and encephalopathies with speech and language dysfunction. *Nature Publishing Group*, *45*(9), 1061–1066.

Li, S., Weidenfeld, J., & Morrisey, E. E. (2004). Transcriptional and DNA Binding Activity of the Foxp1 / 2 / 4 Family Is Modulated by Heterotypic and Homotypic Protein Interactions. *Molecular and Cellular Biology*, *24*(2), 809–822.

MacDermot, K. D., Bonora, E., Sykes, N., Coupe, A.-M., Lai, C. S. L., Vernes, S. C., … Fisher, S. E. (2005). Identification of FOXP2 truncation as a novel cause of developmental speech and language deficits. *American Journal of Human Genetics*, *76*(6), 1074–80.

Madison, D. L., Wirz, J. a, Siess, D., & Lundblad, J. R. (2013). Nicotinamide adenine dinucleotide-induced multimerization of the co-repressor CtBP1 relies on a switching tryptophan. *The Journal of Biological Chemistry*, *288*(39), 27836–48.

Newbury, D. F., Winchester, L., Addis, L., Paracchini, S., Buckingham, L. L., Clark, A., … Monaco, A. P. (2009). CMIP and ATP2C2 Modulate Phonological Short-Term Memory in Language Impairment. *American Journal of Human Genetics*, *85*(2), 264–272.

Reimers-Kipping, S., Hevers, W., Pääbo, S., & Enard, W. (2011). Humanized Foxp2 specifically affects cortico-basal ganglia circuits. *Neuroscience*, *175*, 75–84.

Roll, P., Vernes, S. C., Bruneau, N., Cillario, J., Ponsole-Lenfant, M., Massacrier, A., … Szepetowski, P. (2010). Molecular networks implicated in speech-related disorders: FOXP2 regulates the SRPX2/uPAR complex. *Human Molecular Genetics*, *19*(24), 4848–60.

Sakai, Y., Shaw, C. a, Dawson, B. C., Dugas, D. V, Al-Mohtaseb, Z., Hill, D. E., & Zoghbi, H. Y. (2011). Protein interactome reveals converging molecular pathways among autism disorders. *Science Translational Medicine*, *3*(86), 86ra49.

Shu, W., Lu, M. M., Zhang, Y., Tucker, P. W., Zhou, D., & Morrisey, E. E. (2007). Foxp2 and Foxp1 cooperatively regulate lung and esophagus development. *Development*, *134*(10), 1991–2000.

Shu, W., Yang, H., Zhang, L., Lu, M. M., & Morrisey, E. E. (2001). Characterization of a new subfamily of winged-helix/forkhead (Fox) genes that are expressed in the lung and act as transcriptional repressors. *The Journal of Biological Chemistry*, *276*(29), 27488–97.

Sia, G. M., Clem, R. L., & Huganir, R. L. (2013). The human language-associated gene SRPX2 regulates synapse formation and vocalization in mice. *Science*, *342*(6161), 987–91.

Sin, C., Li, H., & Crawford, D. a. (2015). Transcriptional Regulation by FOXP1, FOXP2, and FOXP4 Dimerization. *Journal of Molecular Neuroscience: MN*, *55*(2):437–448.

Spiteri, E., Konopka, G., Coppola, G., Bomar, J., Oldham, M., Ou, J., … Geschwind, D. H. (2007). Identification of the transcriptional targets of FOXP2, a gene linked to speech and language, in developing human brain. *American Journal of Human Genetics, 81*(6), 1144–57.

Turner, S. J., Hildebrand, M. S., Block, S., Damiano, J., Fahey, M., Reilly, S., … Morgan, A. T. (2013). Small intragenic deletion in FOXP2 associated with childhood apraxia of speech and dysarthria. *American Journal of Medical Genetics. Part A*, *161*(9), 2321–6.

Vernes, S. C., Nicod, J., Elahi, F. M., Coventry, J. a, Kenny, N., Coupe, A.-M., … Fisher, S. E. (2006). Functional genetic analysis of mutations implicated in a human speech and language disorder. *Human Molecular Genetics*, *15*(21), 3154–67.

Vernes, S. C., Oliver, P. L., Spiteri, E., Lockstone, H. E., Puliyadi, R., Taylor, J. M., … Fisher, S. E. (2011). Foxp2 regulates gene networks implicated in neurite outgrowth in the developing brain. *PLOS Genetics*, *7*(7), e1002145.

Vernes, S. C., Phil, D., Newbury, D. F., Abrahams, B. S., Ph, D., & Fisher, S. E. (2009). *NIH Public Access*, *359*(22), 2337–2345.

Vernes, S. C., Spiteri, E., Nicod, J., Groszer, M., Taylor, J. M., Davies, K. E., … Fisher, S. E. (2007). High-throughput analysis of promoter occupancy reveals direct neural targets of FOXP2, a gene mutated in speech and language disorders. *American Journal of Human Genetics*, *81*(6), 1232–50.

Zwanzger, P., Domschke, K., & Bradwejn, J. (2012). Neuronal network of panic disorder: the role of the neuropeptide cholecystokinin. *Depression and Anxiety*, *29*(9), 762–74.

Abstracts

Proceedings of the Master's Programme Cognitive Neuroscience is a platform for CNS students to publish their Master thesis. Given the number of submissions, we select the articles that received the best reviews, under recommendation of our editors, for the printed edition of the journal. The abstracts of the other articles are provided below, and for interested readers a full version is available on our website: www.ru.nl/master/cns/journal.

Appetitive-aversive counter conditioning in serotonin transporter knockout rats

Amanda Almacellas B., Peter Karel, Judith Homberg

Cocaine is the second most used illicit drug and an effective treatment against addiction and relapse is still to be found. The conditioned positive reinforcement that environmental stimuli constitute when paired to cocaine use is a challenging pitfall for the extinction of drug-seeking behaviour. Serotonin has an important role in the development of substance addiction: it's involved in both the arousing effects of cocaine and in an individual's propensity to develop drug addiction. The s allele carriers of the 5-HTTLPR polymorphism have been reported to have a higher probability of developing substance abuse. In this study a new paradigm is set up in order to explore a putative new research line towards an addiction treatment which specially benefits this portion of the human population. SERT-/- rats were used to model the s allele carriers and long access cocaine-self administration was used for modelling cocaine addiction. Appetitive-aversive counter conditioning is a cognitive conditioning process which has the potential to be developed as a new addiction treatment effective against relapse. The animals developed addiction for the drug and were relatively influenced by counter conditioning of the conditioning stimuli. In conclusion, our data shows the flaws and strengths of this paradigm, its possible limitations and advantages. In addition it provides a new insight on the nature of drug addiction and Pavlovian conditioning.

Compensation of Parietal Cortex for Perturbations to Frontal Cortex

Andreea Loredana Cretu, Ian Cameron, Ivan Toni

Frontal eye field (FEF) and parietal eye field (PEF) have both been shown to be involved in the control of saccades, but the role of these regions for vector inversion is still not clear. Recent evidence suggests that after FEF disruption, PEF compensates by showing increased BOLD activity. Equally important, dorsolateral prefrontal cortex and FEF have been found to be important for executive control of saccades. In the antisaccade task, participants have to suppress an automatic saccade towards a visual target and generate instead a voluntary saccade towards the opposite direction. This task allows us to dissociate between the brain regions that are critically involved in executive control but also in vector inversion process. To that end, we first used continuous theta burst stimulation (cTBS) to right frontal eye fields (rFEF), right dorsolateral prefrontal cortex, or a control site and we subsequently applied single-pulse transcranial magnetic stimulation (TMS) to right parietal eye fields (rPEF) at different times. Hereafter, participants performed the pro-/anti-saccade task and amplitude, reaction time, and error rates were assessed. rFEF cTBS relative to right primary somatosensory cTBS induced hypometric contralateral antisaccades (i.e., when the visual target was on the right side). By applying single-pulses over rPEF between 120 and 210 ms, the deficits became more pronounced.

Learning Visual Context and Linguistic Regularities in Language Production - an Artificial Language Learning Study

Elise Hopman, Elisabeth Norcliffe, Falk Huettig, Caitlin Fausey

Learning a language involves the detection of statistical regularities in language, the world, and between language and the world. Previous research has shown that people can learn and use many different types of regularities, though, at present, most language production research has only presented participants with a single regularity manipulation in a given experiment. Much less attention has been paid to more realistic situations in which a learner is presented with multiple regularities at the same time. This thesis aims to investigate exactly that: how does the presence of multiple cross-modal statistical regularities influence learning of these regularities? Participants learn an artificial language situated in an artificial world and are then asked to produce sentences in the artificial language to describe novel scenes. During the exposure phase the verb of the sentence, the background colour of the visual scene, or both were independently predictive of sentence structure. In their own productions, people always show the verb biases present in the input to determine the structure of their sentences, regardless of the presence or absence of the colour regularity in the input. More importantly, we observed marginal evidence that the colour regularity is learned better in presence than in absence of the verb regularity. This suggests that the mere presence of an easy to learn regularity may facilitate learning of a harder regularity, even when there is no redundancy between the different regularities. If proven robust by ongoing follow-up experiments, this result has important implications for theories of statistical learning.

How we build persistent memories: an investigation of memory durability during encoding and a manipulation of early consolidation

Leonore Bovy, Isabella Wagner, Mariët van Buuren, Guillén Fernández

Only a subset of our experiences are remembered while most are forgotten. What determines whether we remember or forget? In two studies, we aimed at predicting memory retention by looking at the initial encoding phase of an association memory task and investigated the influence of catecholamines on memory retention. Both studies employed an item-location paradigm.

In the first experiment, we used a subsequent memory paradigm where we additionally differentiated between durable and weak memory persistence. The results revealed that several frontal and temporal areas exhibited increased activation during the encoding of durable in comparison to weak memories, including the fusiform gyrus, inferior frontal gyrus, superior frontal gyrus, and left lateral orbitofrontal cortex. Furthermore, increased connectivity during encoding between the inferior frontal gyrus and the posterior cingulate cortex was predictive of durable memory retention. All in all, these areas have shown to be crucially involved in successful encoding, revealing stronger activation in a specific set of regions that lead to durable memories.

In our second experiment, we explored the influence of methylphenidate on memory retention during the consolidation phase in a double blind, placebo-controlled study. The results revealed no significant difference between groups on memory retention or reaction times. A significant main effect between treatment groups of systolic and diastolic blood pressure and a significant interaction between treatment group and time of heart rate measures was found. To our knowledge, this was the first study to look into the effects of methylphenidate on memory retention during the consolidation phase.

Overall, we investigated the neural correlates of durable memory formation during encoding and the facilitation of memory retention during early consolidation. Future studies should focus on integrating findings on a systems and molecular level to adequately assess predictors for durable memories.

The Role of Prior Uncertainty on the Neural Response to Semantically Predicted and Unpredicted Events

Lukas Spieß, Sasha Ondobaka, Karl Friston, Peter Kok, Floris de Lange, Harold Bekkering

Human perception of the world and one's own body is intrinsically uncertain. Two types of uncertainty are commonly distinguished: uncertainty in the sensory processing stream (likelihood uncertainty) and uncertainty regarding the causes of sensations (prior uncertainty). Although studies are beginning to investigate the role of prior knowledge on perception, action, and cognition, it is currently unclear to what extent neural responses to predicted and unpredicted events are weighted by the amount of uncertainty in the prior that is used to form these predictions. In the current study we devised a numerical inference task that allowed us to independently manipulate predictions and prior uncertainty on a semantic level without establishing artificial probabilistic stimulus-stimulus relationships. Contrary to our expectations, we found no brain areas where neural responses to predicted and unpredicted events are differentially weighted by prior uncertainty. However, we did find increased activity in the right visual cortex in response to semantically unpredicted events and a marginally significant increase in activation in the right supramarginal gyrus when uncertainty was low compared to when it was high. The implications of these findings are discussed with regard to the co-localization of brain regions encoding uncertainty and those responsible for computing prediction errors. Moreover, the results suggest that early sensory cortices respond to unpredicted events even when statistical relationships were kept constant and predictions had to be derived semantically.

Cerebral Compensation in Parkinson's Disease: BOLD Activation in the Oculomotor Network after Perturbation of the Parietal Eye Fields: Implications for Parkinson's Disease.

Femke Struik, Ian Cameron, Ivan Toni, Bas Bloem

Parkinson's disease is characterized by bradykinsesia and akinesia due to degeneration of the dopaminergic neurons in the substantia nigra, causing problems in voluntary movement. To overcome these problems, patients with Parkinson's disease can develop compensational strategies in which they are helped by visual information to initiate movements. However, these compensatory mechanisms are not always beneficial, as strong visual cues can trigger freezing. In previous eye movement experiments, patients with Parkinson's disease are shown to be more reflexive at pro-saccades, but they have problems in inhibiting these reflexes at anti-saccades. Neuroimaging evidence has revealed reduced activity in movement programming regions (frontal eye fields), but increased activity in parietal/occipital visual regions. The aim of the current project was to establish whether this parietal hyperactivity is compensational or pathological. To this end, we disrupted activity in the right intraparietal sulcus (IPS; parietal eye fields). Two Parkinson's patients and seven healthy controls were tested in a pro- and anti-saccade task in three sessions: baseline, after continuous theta-burst stimulation (cTBS) to IPS, and after cTBS to a control region, S1. The BOLD activity in left and right parietal eye fields, frontal eye fields, and dorsolateral prefrontal cortex after cTBS to IPS was compared to cTBS to S1. In healthy controls we found increased activity in right frontal eye field (FEF) after cTBS to right IPS, suggesting compensation of right FEF. These results are discussed in relation to previous transcranial magnetic stimulation (TMS) studies, compensation, and Parkinson's disease.

Certainty About Movement Prediction Influences Beta and Gamma Oscillations

René Terporten, Linda Drijvers, Asli Özyürek, Ole Jensen

Different contexts change the degree of certainty people have in order to predict upcoming observable movements. The aim of the present study was to reveal how certainty affects oscillatory brain activities in the beta (13-35Hz) and gamma (40-100Hz) frequency range. In a magnetoencephalography (MEG) experiment, participants were asked to indicate whether presented action verbs (e.g., 'to wave') matched the subsequent display of a movement occurring in a video. The predictability of upcoming observable movements was manipulated by changing the chance of a match between action verb and displayed movement. Posterior beta and visual gamma power were shown to be relatively stronger for highly predictable conditions, as compared to conditions with lower predictability, during and shortly before display of the movement. These findings provide a window upon top-down inference processes, as indexed by beta power modulations, and onto visual areas in order to minimize prediction error, as reflected by gamma band activity. Overall, we concluded that a context which influences the certainty about upcoming, observable movements of other people triggers an active interplay of oscillatory activity in the beta and gamma frequency band.

Institutes associated with the Master's Programme Cognitive Neuroscience

Donders Institute for Brain, Cognition and Behaviour:
Centre for Cognitive Neuroimaging
Kapittelweg 29
6525 EN Nijmegen

P.O. Box 9101
6500 HB Nijmegen
www.ru.nl/donders/

Donders Institute for Brain, Cognition and Behaviour:
Centre for Neuroscience
Geert Grooteplein Noord 21, hp 126
6525 EZ Nijmegen

P.O. Box 9101
6500 HE Nijmegen
www.ru.nl/donders/

Donders Institute for Brain, Cognition and Behaviour:
Centre for Cognition
Montessorilaan 3
6525 HR Nijmegen

P.O. Box 9104
6500 HB Nijmegen
www.ru.nl/donders/

MAX-PLANCK-GESELLSCHAFT

Max Planck Institute for Psycholinguistics
Wundtlaan 1
6525 XD Nijmegen

P.O. Box 310
6500 AH Nijmegen
http://www.mpi.nl

IN·DEI·NOMINE·FELICITER

Radboud Institute for Molecular Life Sciences
Geert Grooteplein 28
6525 GA Nijmegen

P.O. Box 9101
6500 HB Nijmegen
http://www.ncmls.nl

Radboudumc
Geert Grooteplein-Zuid 10
6525 GA Nijmegen

P.O. Box 9101
6500 HB Nijmegen
http://www.umcn.nl/

Baby Research Center
Montessorilaan 3
6525 HR Nijmegen

P.O. Box 9101
6500 HB Nijmegen
http://babyresearchcenter.nl